Stockholm
University

Geometry, Topology and Emergence in Moiré Systems

Ahmed Abouelkomsan

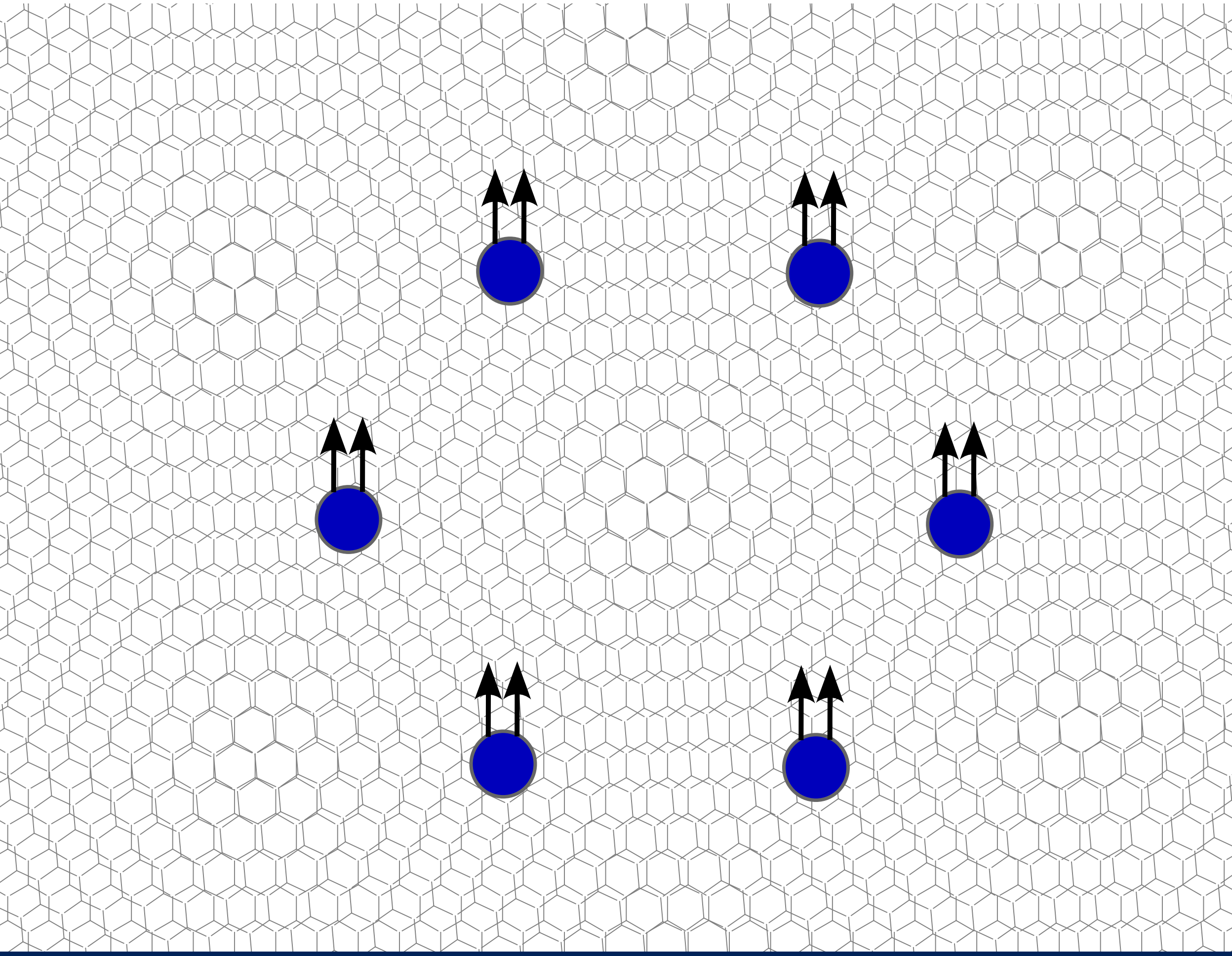

Doctoral Thesis in Theoretical Physics at Stockholm University, Sweden 2022

Geometry, Topology and Emergence in Moiré Systems

Ahmed Abouelkomsan

Academic dissertation for the Degree of Doctor of Philosophy in Theoretical Physics at Stockholm University to be publicly defended on Friday 13 January 2023 at 13.00 in Oskar Kleins Auditorium, FR4, AlbaNova universitetscentrum, Roslagstullsbacken 21 and online via Zoom, public link is available at the department website.

Abstract

The experimental discovery of correlated insulators and superconductivity in highly tunable Van der Waals heterostructures, such as twisted bilayer graphene, has highlighted the role of moiré patterns, resulting from tiny relative twists or lattice constant mismatches, in realizing strongly correlated physics. A key ingredient is the existence of very narrow flat bands where interaction effects are dominant.

In this thesis and the accompanying papers, we theoretically study a number of experimentally relevant moiré systems. We generally show that strong interactions combined with the geometry and the topology of the underlying flat bands can result in a plethora of distinct quantum many-body phases ranging from topological order to multiferroicity. Of particular importance are lattice analogues of the fractional quantum Hall effect known as fractional Chern insulators. They harbour peculiar phenomena such as fractional charge and statistics and provide a route towards realizing topologically ordered states at high temperature. A ubiquitous feature of the many-body physics is the emergence of unique particle-hole dualities driven by the geometry of band-projected interactions.

Keywords: *Moiré materials, Topological phases, Fractional Chern insulators, Quantum geometry, Quantum Hall effects.*

Stockholm 2022
http://urn.kb.se/resolve?urn=urn:nbn:se:su:diva-211973

ISBN 978-91-8014-116-1
ISBN 978-91-8014-117-8

Stockholm University

Department of Physics

Stockholm University, 106 91 Stockholm

GEOMETRY, TOPOLOGY AND EMERGENCE IN MOIRÉ SYSTEMS

Ahmed Abouelkomsan

Stockholm
University

Geometry, Topology and Emergence in Moiré Systems

Ahmed Abouelkomsan

©Ahmed Abouelkomsan, Stockholm University 2022

ISBN print 978-91-8014-116-1
ISBN PDF 978-91-8014-117-8

Cover by the author : Composite fermions on a moiré superlattice.

Printed in Sweden by Universitetsservice US-AB, Stockholm 2022

In memory of my friend
Mohamed who
peacefully left our cruel
world but nevertheless
always on my mind.

Abstract

The experimental discovery of correlated insulators and superconductivity in highly tunable Van der Waals heterostructures, such as twisted bilayer graphene, has highlighted the role of moiré patterns, resulting from tiny relative twists or lattice constant mismatches, in realizing strongly correlated physics. A key ingredient is the existence of very narrow flat bands where interaction effects are dominant.

In this thesis and the accompanying papers, we theoretically study a number of experimentally relevant moiré systems. We generally show that strong interactions combined with the *geometry* and the *topology* of the underlying flat bands can result in a plethora of distinct quantum many-body phases ranging from topological order to multiferroicity. Of particular importance are lattice analogues of the fractional quantum Hall effect known as fractional Chern insulators. They harbour peculiar phenomena such as fractional charge and statistics and provide a route towards realizing topologically ordered states at high temperature. A ubiquitous feature of the many-body physics is the *emergence* of unique particle-hole dualities driven by the geometry of band-projected interactions.

Contents

Abstract **i**

List of Accompanying Papers **v**

Preface **vii**
My Contributions vii
Material From Licentitate Thesis viii
Acknowledgements viii

Sammanfattning på svenska **xi**

1 Introduction **1**
1.1 Van der Waals Heterostructures 1
1.2 The Rise of the Twist 3
1.3 What Is This Thesis About? 5

2 The Quantum Hall Effect and Beyond **7**
2.1 The Quantum Hall Effect 7
2.1.1 Landau Levels 8
2.2 The Integer Quantum Hall Effect 11
2.2.1 Laughlin Pumping Argument 11
2.3 Geometry of Quantum States 12
2.3.1 Applications to Bloch Hamiltonians 13
2.4 Chern Insulators 15
2.4.1 Example: The Haldane Model 16

3 Life in a Flat Chern Band **19**
3.1 The Fractional Quantum Hall Effect 19
3.1.1 Laughlin Wavefunction 20
3.1.2 Haldane Pseudopontetials 20
3.1.3 Laughlin State Excitations 22
3.1.4 Ground State Degeneracy 23

3.1.5 Beyond Fillings $\nu = 1/m$ 24
3.1.6 Halperin States 25
3.2 Fractional Chern Insulators 26
3.2.1 Motivation 26
3.2.2 FCI Phenomenology 27
3.2.3 FCI Identification: Ground State Degeneracy and Spectral Flow 29
3.2.4 FCI Identification: Particle Entanglement Spectrum 31
3.2.5 Higher Chern Number FCIs 33
3.3 Ideal Chern Bands 34
3.3.1 The GMP Algebra 34
3.3.2 Remarks Regarding the Trace Condition 36

4 A Survey of Moiré Systems 39
4.1 Graphene 39
4.1.1 Tight Binding Model 40
4.1.2 Low Energy Model 40
4.2 Multilayer Graphene 42
4.2.1 Bilayer Graphene 42
4.2.2 Trilayer Graphene 44
4.3 Twisted Bilayer Graphene 45
4.3.1 The Continuum Model (CM) 46
4.3.2 Band Structure 49
4.3.3 Symmetries of the Continuum Model 52
4.4 Graphene-Based Models Without C_2 Symmetry 55
4.4.1 Graphene Aligned With Boron Nitride 55
4.4.2 Twisted Bilayer Graphene Aligned With Boron Nitride . . . 56
4.4.3 Trilayer Graphene Aligned With Boron Nitride 57
4.4.4 Twisted Double Bilayer Graphene 59
4.5 Transition Metal Dichalcogenides 60
4.6 TMD Moiré Systems 62
4.6.1 Heterobilayers 62
4.6.2 Homobilayers 63

5 Discussion and Outlook 65
5.1 Summary of Accompanying Papers 65
5.2 Outlook 70

List of Accompanying Papers

Paper I

A. Abouelkomsan, Z. Liu and E.J. Bergholtz, *Particle-Hole Duality, Emergent Fermi Liquids, and Fractional Chern Insulators in Moiré Flatbands*, Phys. Rev. Lett. **124**, 106803 (2020), Editor's Suggestion.

Paper II

Z. Liu, **A. Abouelkomsan** and E.J. Bergholtz, *Gate-Tunable Fractional Chern Insulators in Twisted Double Bilayer Graphene*, Phys. Rev. Lett. **126**, 026801 (2021).

Paper III

D. Varjas, **A. Abouelkomsan**, K. Yang and E.J. Bergholtz, *Topological Lattice Models with Constant Berry Curvature*, SciPost Physics **12** (4), 118 (2022).

Paper IV

A. Abouelkomsan, K. Yang and E.J. Bergholtz, *Quantum Metric Induced Phases in Moiré Materials*, arXiv:2202.10467 (2022).

Paper V

A. Abouelkomsan, E.J. Bergholtz and S. Chatterjee, *Multiferroicity and Topology in Twisted Transition Metal Dichalcogenides*, arXiv.2210.14918 (2022).

Preface

My Contributions

Paper I

I was the driving force of the project from the beginning. I searched for different moiré materials to study. I performed almost all the initial numerical calculations on the models that established the main results of the paper and contributed to the writing of the paper.

Paper II

I initiated the project by finding signatures of FCI states in the model investigated through numerical exact diagonlization studies. I then compared and benchmarked my results for smaller systems with calculations done by Zhao which he later expanded upon and extended to larger system sizes to form the body of the paper. I performed additional band structure and mean field calculations on the model and contributed to the writing of the paper.

Paper III

I did all the numerical calculations on the FCI states, took part in interpreting the results and writing the manuscript.

Paper IV

I did all the numerical calculations that confirmed the theory proposed by the main co-author Kang with which I also did most of the derviations in the text. I contributed to writing the manuscript and interpreting the results.

Paper V

I did all the numerical and theoretical calculations, contributed to the writing and the analysis of the results.

Material From Licentiate Thesis

This thesis contains material from my unpublished Licentiate thesis "Strongly Correlated Moiré Materials" defended in March 2021. The overlapping material are parts in chapters 2, 3 and 4.

Acknowledgements

First and foremost, I am immensely grateful to my advisor Emil Bergholtz for everything in the past 4 years. Working with Emil has been a lot of fun and I consider myself very lucky to have had this opportunity. The list of stuff I am thankful for is quite long. Before I started my PhD, I was still doubtful if I made the right decision. I had some concerns and long thoughts about the usual student-advisor relationship. However, they disappeared quite fast. When I arrived, I felt deeply welcomed and being taken care of. Emil used to check on me almost daily with no expectation or pressure to do stuff. It was just easy to feel comfortable talking to him, even saying the stupidest ideas without being judged. Emil suggested some interesting ideas to research which worked out unexpectedly in a very nice way. I think the concreteness of the ideas he suggested helped me to focus my learning process and avoid being lost. Emil did his best to ensure that I get a good level of supervision while also enjoying a bit of independence. Needless to say, I am very thankful for the unlimited travel resources which was one of the highlights of my PhD. I had the opportunity to discuss my work, enjoy insightful physics discussions and regain my faith in what I am doing.

I would like to thank the members of predefense committee, Ingemar Bengtsson, Sten Hellman and David Marsh for comments on large parts of this thesis.

My time in the KOF corridor has been enjoyable. I particularly want to thank Kang Yang for the nice collaborations during my PhD projects. I am grateful to Johan Carlström for a lot of discussions and help. I am quite thankful to my mentor, Jonas Larson, for friendly and easy-going chats. I also thank Elisabet for being a very nice and fun person to talk and share an office with. I quite enjoyed our daily lunch gathering and the frequent chats with the current and previous people in the corridor. Thanks to Hans, Sören, Supriya, Maria, Eddy, Iman, Yoran, Yaron, Pil, Irina, Daniel, Sreekanth, Marcus, Fan, Ilaria, Carlos I, Carlos II, Lukas I, Lukas

II, Oscar, Anna, Pranay, Paolo and many others for all the interactions during the past years.

I am very lucky to have had the chance to spend a lot of time with a nice group of people from AlbaNova and surroundings such as Kunal, Alex, Gui, Michael, Nikki, Gustavo, Pierluca, Darya, Laura, Vipin and others. Thanks for showing me the other side of the building.

My life in Stockholm was a roller coaster in many aspects. I am grateful to Carlos and Lila for bringing a flavor of my very nice Canada times to Sweden. I am also thankful to all the members of SSideline city run club (and the newly found Run Collective Stockholm) for giving me motivation to combat the darkness and getting acquainted to the concept of social running.

Finally, I consider myself very fortunate to have loving and caring friends with whom I had a lot of fun gatherings and trips. They have truly made my life here way more tolerable. Thanks to Aliki, Jorge, Aurore, Sunniva, my bros Vasilis and Christian and my lovely flatmates Ana and Nadia for being amazing friends and human beings.

أبي العزيز

أعلم أنك ستقرأ هذه الكلمات بكل شغف مثلما دائما عاهدت منك, أهدي لك هذه الرسالة وشكرا لك على كل شئ.

Sammanfattning på svenska

I denna avhandling och de fem bifogade artiklarna studerar vi en ny klass av kvantmaterial som kallas moiré material. De utgörs av två eller flera atomlager som tillsammans visar moiré interferensmönster på grund av en lite relativ rotation. Ibland händer det att bandstrukturen hos dessa material har energiband som är nästan platta. Vi är särskilt intresserade av att förstå vilka kvantmekaniska faser dessa material har när elektroner fyller en del av de platta banden vid låg temperatur. Med användning av numeriska och analytiska verktyg förutser vi många faser som är möjligt i dessa material. Dessa faser inkluderar Fermi flytande faser och exotiska topologiska fraktionella Chern isolatorer.

Efter en kort introduktion i det första kapitlet diskuterar vi teorin av kvanthalleffekten och fraktionerad Chern isolatorer i det andra och tredje kapitlet. Vi beskriver även några tekniker som användas till upptäckt av topologiska faser. Det fjärde kapitlet handlar om teorin av moiré material och deras bandstrukturer. Vi avslutar avhandlingen med en kort sammanfattning av de bifogade artiklarna.

Chapter 1

Introduction

1.1 Van der Waals Heterostructures

The experimental discovery of graphene with all its unique properties has ignited a huge interest into two dimensional materials research [1]. Research on graphene and other atomically-thin materials has developed rapidly in the latest years. This is manifested in numerous experiments being done and many theoretical works on the subject. Advances in fabrication techniques have made it possible not only to fabricate monolayers but also to stack many of them in a single heterostructure in a manner that is quite similar to assembling Lego pieces (Figure 1.1). The resulting heterostructures are commonly referred to as *Van der Waals* heterostructures [2]. Relatively weak Van der Waals forces between the layers are sufficient to keep them in place.

Immediately, this has expanded the possible prospects that can be investigated. On one hand, the heterostructures show unusual properties that need to be explained while on the other hand, gaining control over designing artificial van der Waals materials can be used to target interesting phases of matter.

The tunability of Van der Waals heterostructures shows up in different ways. When the heterostructures are placed between top and bottom metallic gates, the carrier density can be completely controlled. The top and bottom gates can be thought of as parallel plate capacitors implying that the carrier density n is simply given by the relation $n = (C_{\mathrm{TG}}V_{\mathrm{TG}} + C_{\mathrm{BG}}V_{\mathrm{BG}})/e$ where $C_{\mathrm{TG}}\,(C_{\mathrm{BG}})$ and $V_{\mathrm{TG}}\,(V_{\mathrm{BG}})$ are the capacitance and the voltage of the top (bottom) gates respectively and e is the elementary charge.

Many of these heterostructures admit very peculiar band structures as we shall encounter later in this thesis. Theoretically, controlling the carrier density amounts to controlling the filling of the bands which allows accessing different regimes of interest. The potential difference between the top and bottom gates, $V = V_{\mathrm{TG}} -$

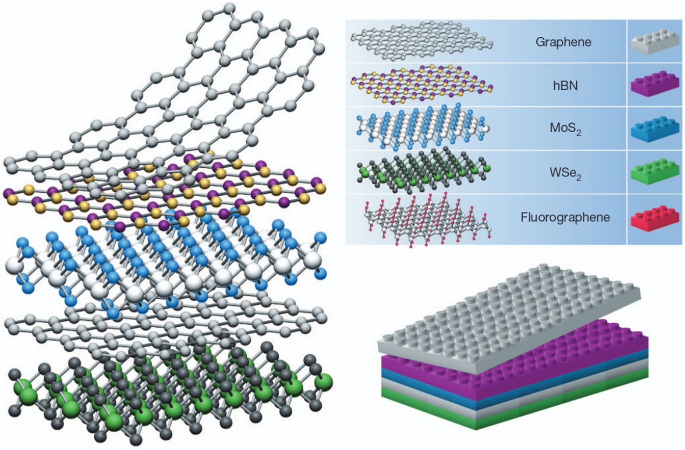

Figure 1.1: A schematic illustration of the Lego-like property of Van der Waals heterostructures. Atomic layers can be stacked on top of each other in stable configurations. The figure is adapted from Ref. [2] with permission from Springer Nature.

V_{BG}, is an additional control knob in the form an applied electric field that can be tuned independently of the carrier density. The response of the heterostructure to an external electric field and its effect on the underlying phases is of interest on its own.

Much earlier, before graphene was manufactured, the quantum Hall effect was discovered in two dimensional electron gases subject to a magnetic field [3,4]. The discovery of the quantum Hall effect, both integer and fractional, has revolutionized the entire field of condensed matter physics and has reshaped our understanding of classifying different quantum phases of matter.

For instance, fractional quantum Hall states represent a new kind of order, *topological* order, with peculiar properties that include topological degeneracies, excitations with fractional charge and statistics and patterns of long-range entanglement [5,6]. A key ingredient to the formation of these phases is strong interactions. The electronic structure consists of Landau levels that are completely flat and as a consequence, interactions dominate the relevant physics.

The fractional quantum Hall effect is one example of a *strongly correlated* phase of matter that is central to this thesis but it is not the only one. Strongly correlated physics encompasses a significant portion of research on quantum many-body systems. It's concerned with phases of matter that can only be understood when strong electron-electron interactions are taken into account. Going away from ideal limits where electron-electron interactions are neglected greatly complexify the problem on one hand but on another hand opens the door towards exotic and

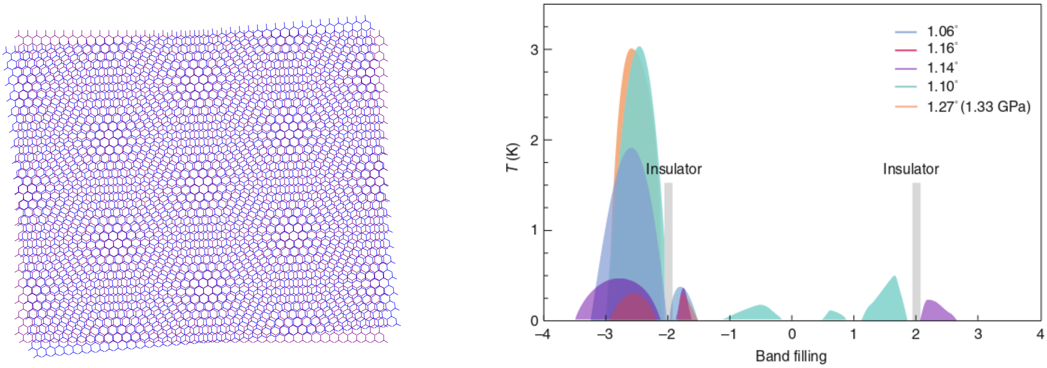

(a) **(b)**

Figure 1.2: (a) An example of a moiré pattern obtained by twisting two hexagonal layers (purple and blue). (b) A compilation plot of phase diagrams of a number of experiments done on twisted bilayer graphene at different twist angles. The main feature is the emergence of superconducting domes (the coloured domes) around insulating states at integer band fillings. The figure is adapted from Ref. [7] with permission from Springer Nature.

unconventional phases of matter. Flat bands are one way to make interactions pronounced and hence more likelihood to stabilize an interaction-induced phase.

1.2 The Rise of the Twist

One way of flattening the bands of Van der Waals heterostructures would be by applying an external magnetic field to create Landau levels. It turns out there is another intricate way of achieving this. That is through the application of a superlattice potential, a periodic potential with a periodicity that is much larger than the underlying lattice structure. A Van der Waals heterostructure is a natural platform for superlattice potentials due to the possible formation of *moiré* patterns.

Moiré patterns are long distance modulations that result from a slight lattice mismatch or a tiny relative twist between adjacent layers. In Figure 1.2(a), we show an example of a moiré pattern from twisting two hexagonal layers. Quite remarkably, a superlattice potential from moiré patterns is sometimes enough to create flat bands. A famous example of this is twisted bilayer graphene [8,9], made out of two layers of graphene with a relative twist (same moiré pattern as Figure 1.2(a)). For tiny twist angles, the system acquires a periodicity on a much larger scale. At a set of *magic* twist angles, the system has extremely flat bands around the charge neutrality point [1].

We will recap here some early experimental results to give the reader a flavor of the current status of the field. However, it should be noted that this is rapidly developing and new experiments with intriguing outcomes have been (and still being) performed and we are far from a complete understanding of all the experimental results.

A series of seminal experiments [10–14] done on twisted bilayer graphene have shown that, upon doping the bands around charge neutrality so that there are integer number of electrons or holes per moiré unit cell, a series of correlated insulators appear. The insulating states are correlated in the sense that they are formed solely by interactions and cannot be understood from the single particle picture which predicts semimetallic states instead.

In addition, moving a bit away from the fillings which corresponds to the correlated insulators, superconducting states appear. Superconductivity is an interesting subject on its own and is arguably what brought so much interest to this field. That being said, superconductivity is outside the general scope of this thesis. The phase diagram as function of band filling for a number of devices shows a common structure of superconducting domes around insulating states as indicated in Figure 1.2(b). However, we stress that superconductivity has been also observed in the absence of nearby insulating states [15, 16].

The experimental findings were found to depend, to an certain extent, on the device details. In devices where boron nitride (a substrate layer) is aligned to one of the graphene layers, a quantized Hall response was detected [17] at filling $\nu_T = +3$ corresponding to completely filling 3 out of the 4 conduction bands above charge neutrality. These Chern insulator states are also ferromagnetic. Similar experimental findings were obtained in [18] but later experiments [19] demonstrated an unconventional series of Chern insulator states that are believed to break time reversal symmetry spontaneously as a consequence of strong interactions without the need to align one of the layers with boron nitride. All of this demonstrates the versatility of twisted bilayer graphene as a platform for strongly correlated physics that is still yet to be fully explored. It is one of the systems that we study in this thesis and the accompanying papers.

Moreover, we investigate two other graphene-based moiré systems. The first is ABC stacked trilayer graphene aligned with boron nitride [20–22]. It enjoys an extra degree of tunability in the form of an external electric field that controls the bandwidth and the topology of its valence band. Gate-tunable Mott insulators, superconducting states and correlated ferromagnetic Chern insulators have been reported in this system at integer fillings [23–25]. In addition, a recent experiment has shown signs of ferromagnetism at non-integer fillings [26]. The second is twisted double bilayer graphene [21,27–31]. Similar to trilayer graphene aligned with boron nitride, an applied external electric field changes the bandwidth and the topology of the bands which provides extra control in addition to tuning the twist angle. Ferromagnetic correlated insulator states have been reported in such a system [32–35].

---

[1] The charge neutrality point is where the Fermi level should be so that the material is charge neutral. For instance, this corresponds to the Dirac points in monolayer graphene.

Moiré patterns are not exclusive to graphene-based structures but they also can form in other Van der Waals heterostructures. In addition to graphene with its remarkable properties, a large and distinct class of two dimensional materials includes semiconductors made from transition metal dichalcogenides (TMDs) [36,37]. Experiments on both heterobilayers made of two different TMDs and homobilayers made of the same TMD material have shown evidence of remarkably wide range of phenomena such as Hubbard-like physics [38–40], generalized Wigner crystals [41–43], continuous quantum phase transitions [44, 45] and the quantum anomalous Hall effect [46, 47].

1.3 What Is This Thesis About?

The goal of this thesis and the accompanying papers is to study interactions in the flat bands of the aforementioned moiré systems with the aim of mapping out the interacting phase diagram.

The thesis chapters provide a brief introduction to most of the background material relevant the accompanying papers, namely quantum Hall physics and moiré physics.

In Papers I [48], II [49], III [50] and IV [51], we are concerned with *fractional* band fillings corresponding to non-integer fillings per moiré unit cell. While almost all experiments done on moiré systems focused on integer fillings, little in comparison has been done at fractional fillings.

Of particular importance when the band filling is fractional are lattice analogues of the fractional quantum Hall states, known as fractional Chern insulators [52,53]. They have been observed [54] for the first time experimentally in a Van der Waals heterostructure, albeit with a very strong magnetic field that creates the underlying Landau levels.

Fractional Chern insulator states are of great experimental interest because they offer the possibility of realizing fractional quantum Hall physics at high temperature and without the need of strong magnetic field overcoming two of the main drawbacks of the conventional quantum Hall setup.

We seek to figure out if fractional Chern insulator states are possible in moiré systems. We find an affirmative answer as shown in the Paper I [48] and Paper II [49]. Later experimental evidence for fractional Chern insulator states have been found in twisted bilayer graphene [55] confirming one of our theoretical predictions.

In Paper V [56], we focus on *integer* band fillings of twisted TMD homobilayers and construct the phase diagram of the interacting problem when the band filling is odd. Our main finding is robust multiferroicity [57] manifested in coexisting magnetic and electric order. Multiferroics are of great practical interest because of the prospects of controlling magnetism with electric fields and vice-versa which could be used to create energy efficient electronic devices.

Chapter 2

The Quantum Hall Effect and Beyond

In this chapter, we introduce basic notions of the quantum Hall effect focusing on the integer quantum Hall effect and its lattice analogue, the Chern insulator. This is not an attempt at a comprehensive discussion of the vast field of the quantum Hall effect. Instead, we focus only on the necessary concepts. Quantum Hall physics is deeply linked to ideas from geometry and topology which we also discuss alongside their applications to Bloch Hamiltonians.

2.1 The Quantum Hall Effect

The discovery of the quantum Hall effect was a major breakthrough in the field of condensed matter physics that paved the way for new and exotic phases of matter. Classically, in two dimensions, electrons in a magnetic field experience cyclotron motion. When an electric field is introduced, it induces a current $\mathbf{J}$ that is related to the electric field through Ohm's law,

$$\mathbf{J} = \sigma \mathbf{E}, \tag{2.1}$$

where σ is the conductivity matrix with the elements

$$\sigma = \begin{pmatrix} \sigma_{xx} & \sigma_{xy} \\ -\sigma_{xy} & \sigma_{yy} \end{pmatrix}. \tag{2.2}$$

The inverse of this matrix is referred to as the resistivity matrix $\rho = \sigma^{-1}$. The off-diagonal elements of the conductivity matrix measure the Hall effect [58], that is the current induced in one direction due to an applied electric field in the transverse direction. When electrons are confined into a two dimensional plane with a strong

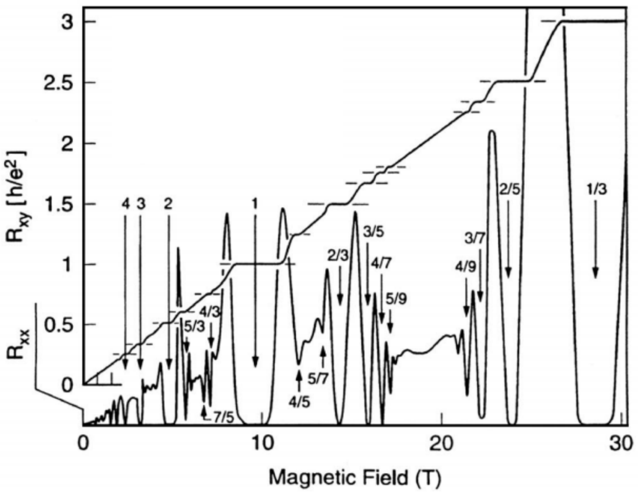

Figure 2.1: Experimental data of the quantum Hall effect: The transverse resistance R_{xy} and the longitudinal resistance R_{xx} are plotted against the applied magnetic field. The figure is adapted from Ref. [59] with permission from Elsevier.

applied magnetic field, the Hall resistivity ρ_{xy} was found [3, 4] to take quantized values given by

$$\rho_{xy} = \frac{2\pi\hbar}{e^2}\frac{1}{\nu} \tag{2.3}$$

where ν is either an integer (the integer quantum Hall effect) or a rational number (the fractional quantum Hall effect) measured with extreme accuracy. As a function of the applied magnetic field, the Hall resistivity exhibits a number of plateaus. Within each plateau, the Hall resistivity is fixed to its quantized value while the longitudinal resistivity ρ_{xx} drops to zero as evident from Figure 2.1. Since the conductivity is the inverse of the resistivity, this implies that the Hall conductivity on the plateaus is also quantized $\sigma_{xy} = -\rho_{xy}^{-1}$ and the longitudinal conductivity also vanishes $\sigma_{xx} = 0$.

2.1.1 Landau Levels

The starting point of any microscopic analysis is to consider the Schrödinger equation for non-interacting electrons with mass m_e in a magnetic field B, a problem solved by Landau [60]. The Hamiltonian is given by

$$H = \frac{\mathbf{\Pi}^2}{2m_e} = \frac{(\mathbf{p} + e\mathbf{A})^2}{2m_e}. \tag{2.4}$$

For the purpose of introducing Laughlin wavefunctions later in section 3.1.1, it is helpful to work in the symmetric gauge where the vector potential $\mathbf{A}$ is given by $\mathbf{A} = -\frac{yB}{2}\hat{x} + \frac{xB}{2}\hat{y}$. Diagonalizing the Hamiltonian above is done by defining two sets of creation and annihilation operators that are functions of $\mathbf{\Pi} = \mathbf{p} + e\mathbf{A}$ and $\widetilde{\mathbf{\Pi}} = \mathbf{p} - e\mathbf{A}$,

$$a = \frac{\Pi_x - i\Pi_y}{\sqrt{2e\hbar B}} \quad , \quad a^\dagger = \frac{\Pi_x + i\Pi_y}{\sqrt{2e\hbar B}} \quad \text{with} \quad [a, a^\dagger] = 1 \tag{2.5}$$

$$b = \frac{\widetilde{\Pi}_x - i\widetilde{\Pi}_y}{\sqrt{2e\hbar B}} \quad , \quad b^\dagger = \frac{\widetilde{\Pi}_x + i\widetilde{\Pi}_y}{\sqrt{2e\hbar B}} \quad \text{with} \quad [b, b^\dagger] = 1. \tag{2.6}$$

In the symmetric gauge, $[\Pi_i, \widetilde{\Pi}_j] = 0$ but the Hamiltonian (2.4) is a function of $\mathbf{\Pi}$ only so it commutes with $\widetilde{\mathbf{\Pi}}$. The Hamiltonian written in terms of the creation and annihilation operators a and $a^\dagger$ reads

$$H = \hbar\omega_B(a^\dagger a + \frac{1}{2}). \tag{2.7}$$

with energies of the form

$$E_n = \hbar\omega_B(n + \frac{1}{2}) \qquad n \in \mathbf{N} \tag{2.8}$$

where ω_B is the cyclotron frequency defined as $\omega_B = eB/m_e$. The energy levels are called *Landau* levels. It is easy to see that Landau levels are degenerate because any state obtained by acting m times with the $b^\dagger$ creation operator, $b^{\dagger m}\left|n\right\rangle \sim b^{\dagger m} a^{\dagger n}\left|0\right\rangle$ has the same energy E_n as $\left|n\right\rangle$ because $[H, b^\dagger] = 0$. The generic form of the wavefunctions corresponding to the Landau levels is then given by

$$\left|n, m\right\rangle = \frac{a^{\dagger n} b^{\dagger m}}{\sqrt{n!m!}}\left|0, 0\right\rangle \tag{2.9}$$

where $\left|0, 0\right\rangle$ is the vacuum state. The exact form of the wavefunctions can be obtained by first restricting ourselves to the lowest Landau level $\left|0, m\right\rangle$ and then solving the differential equation $a\left|0, m\right\rangle = 0$. Before doing this, let's write the creation and annihilation operators in complex coordinates $z = x - iy$ and $\bar{z} = x + iy$ with the holomorphic and anti-holomorphic derivatives defined as $\partial = (\partial_x + i\partial_y)/2$ and $\bar{\partial} = (\partial_x - i\partial_y)/2$. This leads to

$$a = -i\sqrt{2}(l_B\bar{\partial} + \frac{z}{4l_B}) \quad , \quad a^\dagger = -i\sqrt{2}(l_B\partial - \frac{\bar{z}}{4l_B}) \tag{2.10}$$

$$b = -i\sqrt{2}(l_B\partial + \frac{\bar{z}}{4l_B}) \quad , \quad b^\dagger = -i\sqrt{2}(l_B\bar{\partial} - \frac{z}{4l_B}) \tag{2.11}$$

where $l_B = \sqrt{\hbar/eB}$ is called the magnetic length scale. It is the effective length scale of the quantum Hall problem. We have then,

$$a\,|0,m\rangle = -i\sqrt{2}(l_B\bar{\partial} + \frac{z}{4l_B})\,|0,m\rangle = 0. \tag{2.12}$$

The solution to the above equation reads

$$|0,m\rangle \equiv \psi_{\mathrm{LLL},m}(z,\bar{z}) = f_m(z)e^{-|z|^2/4l_B} \tag{2.13}$$

with any holomorphic function $f_m(z)$. The lowest state in the lowest Landau level $\psi_{\mathrm{LLL},0}(z,\bar{z})$ is annihilated also by b, this fixes $f_0(z)$ to be a constant so we have $\psi_{\mathrm{LLL},0}(z,\bar{z}) \sim e^{-|z|^2/4l_B}$ and we can get the rest of the states in the lowest Landau level by acting successively with $b^\dagger$ so we end with, up to a normalization constant,

$$\psi_{\mathrm{LLL},m}(z,\bar{z}) \sim \left(\frac{z}{l_B}\right)^m e^{-|z|^2/4l_B^2}. \tag{2.14}$$

The higher Landau levels wavefunctions can be obtained by acting successively with $a^\dagger$ on (2.14). Since the Hamiltonian (2.4) is rotationally invariant in the symmetric gauge, angular momentum is a good quantum number. This can be readily seen by noticing that the wavefunctions (2.14) are eigenfunctions of the angular momentum operator $J = \hbar(z\partial - \bar{z}\bar{\partial})$,

$$J\psi_{\mathrm{LLL},m}(z,\bar{z}) = \hbar m\,\psi_{\mathrm{LLL},m}(z,\bar{z}). \tag{2.15}$$

The degeneracy of each Landau level can be calculated explicitly from the exact form of the wavefunctions. We will state the final result here. The degeneracy of each Landau level is given by $\mathcal{D} = \frac{AB}{\Phi_0}$ with A is the area of the sample and Φ_0 is the flux quantum $\Phi_0 = 2\pi\hbar/e$. One could furthermore define a filling factor ν that tells us about the total filling of the Landau levels. It is given by $\nu = \frac{N_e}{\mathcal{D}} = \frac{n\Phi_0}{B}$ with N_e is the number of electrons in the sample and $n = N_e/A$ is the density of electrons.

Finally, we note that in order to draw useful connections with the classical description of particles in a magnetic field experiencing cyclotron motions, it is possible to decompose the position operator $\hat{\mathbf{r}}$ into two parts,

$$\hat{\mathbf{r}} = (\frac{1}{2}\hat{\mathbf{r}} + \hat{\mathbf{z}} \times \mathbf{p}) + (\frac{1}{2}\hat{\mathbf{r}} - \hat{\mathbf{z}} \times \mathbf{p}) \equiv \boldsymbol{\eta} + \mathbf{R}. \tag{2.16}$$

The operator $\boldsymbol{\eta}$ describes the *cyclotron motion* of an orbit while the operator $\boldsymbol{R}$ describes the *guiding center* of the orbit. In fact, the operators $\boldsymbol{\eta}$ and $\mathbf{R}$ are nothing but the operators $\mathbf{\Pi}$ and $\widetilde{\mathbf{\Pi}}$ defined above multiplied by the square of the magnetic length l_B^2. In addition, they obey the following commutation relations

$$[\eta_x, \eta_y] = il_B^2 \ , \ [R_x, R_y] = -il_B^2 \ , \ [\eta_i, R_j] = 0 \tag{2.17}$$

The Hamiltonian (2.4) depends solely on $\boldsymbol{\eta}$ therefore the degeneracy of a single Landau level can be understood by realizing that the Hamiltonian (2.4) commutes with the guiding center operator $\mathbf{R}$.

2.2 The Integer Quantum Hall Effect

The integer quantum Hall effect can be well-understood without needing to consider interactions between electrons. With an integer ν Landau levels completely filled, a simple calculation shows that the Hall resistivity is given by (2.3) and there is a gap of the order $\hbar\omega_B$ to the next Landau level. At very low temperatures $k_B T \lll \hbar\omega_B$, electrons have no where to go when a small electric field is applied, hence the vanishing longitudinal conductivity σ_{xx}. However, this is not the full story. This argument needs to be modified a bit in order to explain the plateau structure by taking into account disorder effects. It also does not explain why the Hall conductivity should be quantized to an integer.

2.2.1 Laughlin Pumping Argument

Laughlin came up with an argument [61] that explains the quantization of the Hall conductivity which relies on the idea of gauge invariance. The argument makes use of the fact that the eigenspectrum of an annulus is insensitive to the enclosing of an integer number of flux quanta Φ_0. A statement first proven by Byers and Yang in the context of superconducting rings [62]. Let's consider a quantum Hall system defined on an annulus that encloses an extra flux $\Phi(t)$ as shown in Figure 2.2. We then adiabatically switch on the enclosed flux from zero to one flux quantum Φ_0 in time ΔT. As a result, an electromotive force (EMF) is generated in the annulus,

$$\varepsilon(t) = -\frac{d\Phi(t)}{dt} = \oint \mathbf{E} \cdot \mathbf{dl}. \tag{2.18}$$

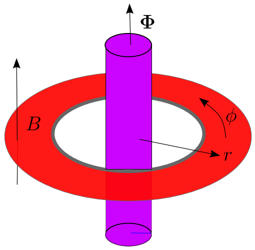

Figure 2.2: The annulus geometry used in Laughlin's argument for the quantization of the Hall conductivity.

The radial current in the annulus I_r is related to the EMF induced around the annulus through the Hall conductance G_H,

$$I_r(t) = G_H \varepsilon(t). \tag{2.19}$$

The total charge pumped in ΔT time is related to the flux change $\Delta\Phi = \Phi(T) - \Phi(0) = \Phi_0$. After inserting one flux quantum Φ_0, the system is physically the same. If we start in the ground state, we have to stay in the exact same ground state after one flux is adiabatically inserted assuming no ground state degeneracy [1] but during this process, an integer number of charges $\Delta Q = pe$ is pumped from one end to the other end in the annulus. The Hall conductance has to be quantized by the virtue of (2.18). This provides a way of thinking of quantum Hall systems as charge pumps.

2.3 Geometry of Quantum States

In this technical section, we introduce in a non-rigorous way (the physicist's way) the notion of quantum state geometry. We shall see how this gives rise to the familiar physical quantities such as the Berry curvature and the Fubini-Study metric which are a corner stone in the modern understanding of condensed matter systems at the level of the wavefunctions i.e, beyond energetics.

We consider a quantum-mechanical system described by a Hamiltonian $H(x)$ that is a function of generic parameters $x = (x_1, x_2, \dots)$ living in a manifold $x \in \mathcal{M}$. The Hamiltonian acts on a N dimensional Hilbert space $\mathcal{H}$ and has energies and eigenstates $E_n(x)$, $|u_n(x)\rangle$ respectively with $n = 1, 2, \dots, N$

The Hilbert space $\mathcal{H}$ contains all possible quantum states $|\psi(x)\rangle = \sum_n c_n |u_n(x)\rangle$, however, we know from standard quantum mechanics that quantum states related by gauge transformations $|\psi(x)\rangle$ and $|\tilde{\psi}(x)\rangle = e^{i\phi(x)} |\psi(x)\rangle$ are physically equivalent so the *physical* Hilbert space is in fact not $\mathcal{H}$ but it is $\mathcal{H}/U(1) \equiv CP^{N-1}$ or what is known as the complex projective space [2]. Given the parameter dependence x, the gauge invariant projector $P = |\psi(x)\rangle \langle\psi(x)|$ implements the following map,

$$f : \mathcal{M} \to CP^{N-1}. \tag{2.20}$$

Therefore, quantum states can be generally understood as maps from a parameter space to a complex projective space. Let us denote the coordinates of the complex projective space as y such that $y^a = f^a(x^\alpha)$. The complex projective space is an example of a Riemannian manifold [63] equipped with a *metric* $g_{ab}(y)$ and a locally defined *connection* $A_a(y)$. Intuitively, the metric gives a notion of distance and the connection implements parallel transport. From the connection it is possible to define a *curvature* $\Omega_{ab}(y) = \partial_a A_b(y) - \partial_b A_a(y)$. The map f induces a metric $g_{\alpha\beta}(x)$ and a connection $A_\alpha(x)$ back on the manifold $\mathcal{M}$ given by

---

[1] If the ground state in degenerate, we are guaranteed to stay in a ground state, not necessarily the ground state we started with. That is indeed the case for the fractional quantum Hall effect.

[2] A complex projective space CP^N is defined as the set of equivalence classes on the complex space C^{N+1} with complex coordinates z_i such that $(z_1, z_2, \dots z_{N+1}) \sim \lambda(z_1, z_2, \dots z_{N+1})$ where λ is any non-zero complex number.

$$g_{\alpha\beta} = \frac{\partial f^a}{\partial x^\alpha}\frac{\partial f^b}{\partial x^\beta} g_{ab}, \quad A_\alpha = \frac{\partial f^a}{\partial x^\alpha} A_a. \tag{2.21}$$

This is usually termed as the "pullback" of a given map f. From the induced connection $A_\alpha(x)$, a curvature $\Omega_{\alpha\beta}(x)$ can be constructed. $g_{\alpha\beta}(x)$ and $\Omega_{\alpha\beta}(x)$ are the Fubini-Study metric (also referred to as the quantum metric) and the Berry curvature respectively. They are given explicitly by

$$g_{\alpha\beta}(x) = \mathrm{Re}[\langle \partial_\alpha \psi(x) | \partial_\beta \psi(x)\rangle - \langle \partial_\alpha \psi(x) | \psi(x)\rangle \langle \psi(x) | \partial_\beta \psi(x)\rangle]. \tag{2.22}$$

$$\Omega_{\alpha\beta}(x) = -2\,\mathrm{Im}[\langle \partial_\alpha \psi(x) | \partial_\beta \psi(x)\rangle] \tag{2.23}$$

From the definition, the Berry curvature $\Omega_{\alpha\beta}(x)$ is an antisymmetric tensor, $\Omega_{\alpha\beta}(x) \equiv \epsilon_{\alpha\beta}\Omega(x)$. The metric $g_{\alpha\beta}(x)$ measures infinitesimal distances between quantum states

$$|\,\langle \psi(x) | \psi(x+dx)\rangle\,| \approx 1 - \frac{1}{2} g_{\alpha\beta}(x) dx^\alpha dx^\beta \tag{2.24}$$

and the Berry curvature $\Omega_{\alpha\beta}(x)$ contains information about the geometrical Berry phases [64] obtained for closed loop γ in the parameter space $\mathcal{M}$

$$\phi(\gamma) = \int_\gamma A(x) = \int_S dS^{\alpha\beta}\, \Omega_{\alpha\beta}(x) \tag{2.25}$$

where S is the surface enclosed by the loop γ.

2.3.1 Applications to Bloch Hamiltonians

Having introduced briefly the Berry curvature and the quantum metric from a mathematical point of view, let's apply this to two dimensional non-interacting lattice systems. In this context, the parameters $x = (k_x, k_y)$ are the two dimensional crystal momentum. Assuming we have a non-interacting lattice system with N bands, a generic Hamiltonian that describes this is given by

$$H = \sum_{\mathbf{k},a,b} c^\dagger_{\mathbf{k},a} h_{a,b}(\mathbf{k}) c_{\mathbf{k},b} \tag{2.26}$$

where $c^\dagger_{\mathbf{k},a}(c_{\mathbf{k},a})$ are creation (annihilation) operators for particles with crystal momentum $\mathbf{k}$ and $a = 1, 2, \ldots, N$ combined orbital/spin indices. The periodic structure of the problem allows the usage of Bloch's theorem and defines a Brillouin zone for the crystal momentum $\mathbf{k} = (k_x, k_y)$ that is a torus $\mathbf{T}^2$.

Diagonalizing the Hamiltonian (2.26) by solving the $N \times N$ eigenvalue problem $\sum_b h_{ab}(\mathbf{k}) u_n^b(\mathbf{k}) = E_n(\mathbf{k}) u_n^a(\mathbf{k})$, we obtain

$$H = \sum_{\mathbf{k},n} E_n(\mathbf{k}) \gamma^\dagger_{\mathbf{k},n} \gamma_{\mathbf{k},n} \tag{2.27}$$

where $E_n(\mathbf{k})$ describes the dispersion of $n = 1, \ldots, N$ bands with eigenstates $|\mathbf{k}, n\rangle = \gamma^\dagger_{\mathbf{k},n} |0\rangle = \sum_a u_n^a(\mathbf{k}) c^\dagger_{\mathbf{k},a} |0\rangle$. Following the definitions introduced in the previous section, a Berry curvature and quantum metric in the Brillouin zone can be constructed for single band n with a wavefunction $|\mathbf{k}, n\rangle$ by using equations (2.22) and (2.23) with $|\psi(x)\rangle \equiv |\mathbf{k}, n\rangle$ and $\alpha, \beta \equiv k_x, k_y$ [3].

It is possible to combine the Fubini-Study metric and the Berry curvature into one single quantity known as the quantum geometric tensor $R^n_{\alpha\beta}(\mathbf{k})$ defined as

$$R^n_{\alpha\beta}(\mathbf{k}) = \langle \partial_\alpha \mathbf{k}, n| Q_n(\mathbf{k}) |\partial_\beta \mathbf{k}, n\rangle \equiv g^n_{\alpha\beta}(\mathbf{k}) + \frac{i}{2} \epsilon_{\alpha\beta} \Omega^n(\mathbf{k}) \tag{2.28}$$

with $Q_n(\mathbf{k}) = 1 - |\mathbf{k}, n\rangle \langle \mathbf{k}, n|$ is the orthogonal projector to the band n. The Fubini-Study metric $g^n_{\alpha\beta}(\mathbf{k})$ and the Berry curvature $\Omega^n(\mathbf{k})$ are the symmetric (real) and the antisymmetric (imaginary) parts of $R^n_{\alpha\beta}(\mathbf{k})$

$$g^n_{\alpha\beta}(\mathbf{k}) = \frac{1}{2}(R^n_{\alpha\beta}(\mathbf{k}) + R^n_{\beta\alpha}(\mathbf{k})) \tag{2.29}$$

$$\Omega^n(\mathbf{k}) = i \sum_{\alpha,\beta} \epsilon^{\alpha\beta} R^n_{\alpha\beta}(\mathbf{k}) \tag{2.30}$$

where $\epsilon^{\alpha\beta}$ is the Levi-Civita tensor.

The quantum geometric tensor $R^n_{\alpha\beta}(\mathbf{k})$ is a positive semi-definite matrix which means $\mathrm{tr} R^n(\mathbf{k}) \geq 0$. From this, one obtains the following important inequality

$$\mathrm{tr} g^n(\mathbf{k}) \geq |\Omega^n(\mathbf{k})| \tag{2.31}$$

that relates the Fubini-Study metric and the Berry curvature. The trace of the Fubini-Study metric at a certain momentum point $\mathbf{k}$ is always bounded by the absolute value of the Berry curvature at the same point. This places constraints on the form of the Fubini-Study metric in the Brillouin zone.

The role of the Berry curvature in understanding the properties of condensed matter systems is extensive. Semi-classically, the Berry curvature resembles a magnetic field in momentum space therefore the dynamics of electrons in bands with non-trivial Berry curvature can be quite unusual [65,66]. We will focus here on the connection to the quantum Hall effect and later to ideal Chern bands in section 3.3 but we refer the reader to Ref. [67] for a comprehensive review.

---

[3] The definition of both the Berry curavture and Fubini-Study metric can be generalized to more than a single band.

The Berry curvature is a local geometrical quantity, however using the Berry curvature, it is possible to build global topological quantities. For example, a core concept that is used in characterizing the topology of a band is the Chern number defined as,

$$C_n = \frac{1}{2\pi} \int_{\mathbf{T}^2} d^2k \ \Omega^n(\mathbf{k}) \tag{2.32}$$

where the integral is carried over the first Brillouin zone. The Chern number is always an integer [68]. For a Chern number to be well-defined for a band, it has to be gapped from the other bands. The Chern number does not change under continuous deformations that keep the band gap open therefore it is an example of one topological invariant (in two spatial dimensions) that can be used to classify different phases of matter.

The Fubini-Study metric is a much less explored quantity in the context of condensed matter systems. A whole lot of useful information can be gained from characterizing distances between Bloch states, for instance, in making a connection between Chern bands and Landau levels as we will encounter in section 3.3. The uniformity and relative degree of fluctuations of both the Berry curvature and the Fubini-Study metric have direct impact on the stability of a novel class of phases called fractional Chern insulators which we introduce in section 3.2. One interesting application of the Fubini-Study metric that is worth mentioning is in the context of superconductivity and Bose-Einstein condensation in flat bands [69,70].

2.4 Chern Insulators

Starting from a two dimensional lattice model, consider the case where the chemical potential is located in a gap somewhere in the band structure such that the system is at total integer filling. It was shown [71], using the Kubo formula, that the Hall conductivity can be written as a sum of the Chern numbers of occupied bands.

$$\sigma_{xy} = \frac{e^2}{2\pi\hbar} \sum_{\alpha} C_\alpha \tag{2.33}$$

where α runs over the occupied bands, i.e. below the chemical potential. The quantization and robustness of the Hall conductivity can then be seen as a result of it being a topological quantity.

The formula (2.33), generally referred to as the TKNN invariant, was first derived in the context of models with periodic potentials and external magnetic fields.

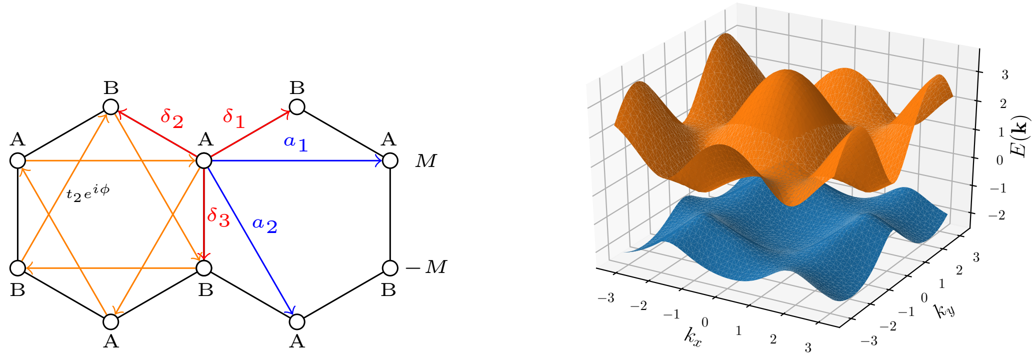

(a) **(b)**

Figure 2.3: (a) The honeycomb lattice with the two sublattices A and B. The bases of the lattice are given by the vectors $\mathbf{a}_1$ and $\mathbf{a}_2$. Nearest neighbor hoppings are implemented by the vectors $\{\boldsymbol{\delta}_i\}$. The orange arrows denote the directions for which the complex next nearest hopping phase is positive. (b) Band structure of the Haldane model with parameters $(t_1, t_2, \phi, M) = (1, 0.2, \pi/3, 0.5)$. The lowest band carries a Chern number $C = 1$

Later, Haldane [72] introduced a model on a honeycomb lattice that shows a non-zero quantized Hall conductance without an external magnetic field. A non-zero Chern number, or equivalently a non-zero Hall conductance, is linked to breaking of time reversal symmetry. An external magnetic field breaks time-reversal invariance by default but such a symmetry can be also broken through complex hopping processes on the lattice with a total of zero flux through each unit cell. Lattice models that possess Chern bands showing non-zero quantized Hall response are referred to as *Chern Insulators.* We reserve the name here for models with zero external magnetic field although the terminology is sometimes used for both.

2.4.1 Example: The Haldane Model

Let's introduce the Haldane model as an explicit example of a Chern insulator. We will also use the same model supplied with interactions as a prototype of a fractional Chern insulator in section 3.2. The Haldane model is defined on a honeycomb lattice. A famous material with such a lattice structure is graphene discussed later in section 4.1. The honeycomb lattice is not a Bravais lattice but this can be overcome by taking a unit cell of two atoms, referred to as A and B sublattices.

On the honeycomb lattice shown in Figure 2.3, there is a real nearest hopping

t_1, a complex next-nearest hopping $t_2 e^{i\phi}$ and a sublattice potential implemented by a mass term M with opposite signs on the A and B sublattices. A positive complex hopping is determined by the direction of the orange arrows in Figure 2.3(a). A tight binding Hamiltonian that takes into account nearest neighbor and next neighbor hopping is then given by

$$H = -\sum_{\langle i,j \rangle} t_1 c^\dagger_{i,A} c_{j,B} - \sum_{\langle\langle i,j \rangle\rangle} t_2 e^{\pm i\phi} (c^\dagger_{i,A} c_{j,A} + c^\dagger_{i,B} c_{j,B}) + \text{h.c} \tag{2.34}$$

where $c^\dagger_{i,\alpha}(c_{i,\alpha})$ creates(annhilates) an electron on site $\mathbf{R}_i$ and sublattice $\alpha = A, B$.

There are 3 nearest neighbors given by the vectors $\boldsymbol{\delta}_1 = a(\frac{\sqrt{3}}{2}, \frac{1}{2})$, $\boldsymbol{\delta}_2 = a(-\frac{\sqrt{3}}{2}, \frac{1}{2})$ and $\boldsymbol{\delta}_3 = a(0, -1)$ shown in Figure 2.3(a) with a the distance between sublattices. Moreover, there are 6 next nearest neighbors given by the primitive lattice vectors $\pm\mathbf{a}_1 = \pm\sqrt{3}a(1, 0)$, $\pm\mathbf{a}_2 = \sqrt{3}a(\pm\frac{1}{2}, \mp\frac{\sqrt{3}}{2})$ and $\pm\mathbf{a}_3 = \pm\mathbf{a}_1 \mp \mathbf{a}_2$. Solving this tight-biding problem yields a Bloch Hamiltonian in the bases of A and B sublattices $H = \sum_k (c^\dagger_A(\mathbf{k}),\, c^\dagger_B(\mathbf{k}))\mathcal{H}(\mathbf{k})(c_A(\mathbf{k}),\, c_B(\mathbf{k}))^T$ with

$$\begin{aligned}
\mathcal{H}(\mathbf{k}) &= d_0 \mathbf{I} + \sum_i d_i \sigma_i \\
d_0 &= 2t_2 \cos\phi \sum_{i=1,2,3} \cos(\mathbf{k} \cdot \mathbf{a_i}) \\
d_x &= t_1 \sum_{i=1,2,3} \cos(\mathbf{k} \cdot \boldsymbol{\delta}_i) \\
d_y &= t_1 \sum_{i=1,2,3} \sin(\mathbf{k} \cdot \boldsymbol{\delta}_i) \\
d_z &= M - 2t_2 \sin\phi \sum_{i=1,2,3} \sin(\mathbf{k} \cdot \mathbf{a_i})
\end{aligned} \tag{2.35}$$

where σ_i are the Pauli matrices and $\mathbf{I}$ is the identity matrix. The energies of the two bands of the Hamiltonian are given by $E(\mathbf{k}) = d_0 \pm \sqrt{d_x^2 + d_y^2 + d_z^2}$. For spinless particles, time-reversal symmetry acts on the Bloch Hamiltonian as $\mathcal{T}\mathcal{H}(\mathbf{k})\mathcal{T}^{-1} = \mathcal{H}^*(-\mathbf{k})$. We see that time-reversal symmetry is broken for $\phi \neq 0$. If, in addition to the broken time-reversal symmetry, the two bands are gapped, they acquire a non-zero Chern number $C = \pm 1$. When the Fermi level lies in the band gap, the system is a Chern insulator. An example of such a scenario is shown in Figure 2.3(b) where the lowest band has a Chern number $C = 1$.

Chapter 3

Life in a Flat Chern Band

We have seen in the previous chapter that the integer quantum Hall effect is linked to a non-zero Chern number. One implies the other and vice-versa. The purpose of this chapter is to focus on the physics of bands that have non-zero Chern numbers. We refer to those as *Chern* bands. The situation becomes more interesting when the Chern band is flat. The canonical example of this is, again, the Landau level. Apart from showing quantized integer Hall response when they are completely filled, partial filling of flat Chern bands can give rise to exotic states with fractional Hall response.

In this chapter, we discuss the physics of the fractional quantum Hall effect (FQHE) in the lowest Landau level and then move on to introduce its lattice realizations known as fractional Chern insulators (FCI). Characterization of a generic Chern band with respect to how close or far it is to a Landau level is discussed at the end of the chapter.

3.1 The Fractional Quantum Hall Effect

The story is different when the filling factor ν (equation (2.3)) takes fractional values. Interactions are essential in order to explain the fractional quantum Hall effect since fractionally filling Landau levels while ignoring interactions would result in a compressible gapless state because of the Landau level degeneracy, but we know that fractional quantum Hall states are gapped and incompressible. Looking back at the experimental data of the fractional quantum Hall effect (Figure 2.1), one notices that most of the prominent plateaus and peaks occur at values $\nu < 1$ which corresponds to fractional filling of the lowest Landau level. We shall focus on the fractional quantum Hall effect in the lowest Landau level. The fractional quantum Hall effect still occurs in higher Landau levels, for example at filling $\nu = 5/2$ with arguably more interesting and exotic properties (for example see Ref [73] and references therein).

The problem of electrons interacting in the lowest Landau level is extremely hard to tackle using standard perturbative techniques due to the massive degeneracy of the lowest Landau level in addition to its complete flatness. This leaves us with a purely interacting problem. A common and quite distinctive approach to the quantum Hall problem is to write trial many-body wavefunctions. The trial wavefunctions are not the exact many-body wavefunctions but they manage to capture the universal properties of the system, namely the topological properties such as the fractionally charged excitations and their fractional statistics. We discuss next one such seminal trial wavefunction.

3.1.1 Laughlin Wavefunction

The trial wavefunctions approach was first proposed by Laughlin [74] in an attempt to explain the quantized Hall conductivity at fillings $\nu = 1/m$. The Laughlin wavefunction reads,

$$\psi_{\text{Laughlin}}(z_i) = \prod_{i<j}(z_i - z_j)^m e^{-\sum_{i=1}^{n}|z_i|^2/4l_B^2} \tag{3.1}$$

where m is odd for fermions and even for bosons. When $m = 1$ corresponding to an integer filling $\nu = 1$, the Laughlin wavefunction is just a Slater determinant of the lowest Landau level wavefunctions in the symmetric gauge (2.14). It turns out that the Laughlin wavefunction gives a very accurate description for the fractional quantum Hall effect at fillings $\nu = 1/m$.

There exist many ways to justify this. Numerically, it has a very high overlap with the exact ground state obtained by solving the problem for few interacting particles in a Coulomb potential [75]. Another way to look at it is by taking a step backward and asking what interaction Hamiltonian the Laughlin state is a ground state for. In other words, finding a parent Hamiltonian for the Laughlin state and comparing it to the Coulomb interaction Hamiltonian projected to the lowest Landau level. This can be done through the language of Haldane pseudopotentials [76].

3.1.2 Haldane Pseudopontetials

Haldane pseudopontetials are a way to parameterize any two-body interaction given that it depends only on the distance between the two particles. The two-particle wavefunction obtained from the lowest Landau level wavefunctions (2.14) reads

$$\psi_{m_1,m_2}(z_1, z_2) \sim (z_1^{m_1} z_2^{m_2} \pm z_1^{m_2} z_2^{m_1})e^{-(|z_1|^2+|z_2|^2)/4l_B^2}. \tag{3.2}$$

m	0	1	2	3	4	5	6
V_m	0.88623	0.44311	0.33234	0.27695	0.24233	0.21809	0.19992

Table 3.1: Haldane Pseudopotentials of the Coulomb interaction in the lowest Landau level.

z_1 and z_2 are the complex coordinates for particle 1 and particle 2 respectively while m_1 and m_2 are the angular momentum values of particle 1 and particle 2 respectively. It is possible to decompose it in terms of relative and center of mass coordinates, $z = (z_1 - z_2)/\sqrt{2}$ and $Z = (z_1 + z_2)/\sqrt{2}$,

$$\psi_{M,m}(Z, z) = \langle z, Z|M, m\rangle \sim Z^M z^m e^{-(|Z|^2+|z|^2)/4l_B^2} \sim \psi_M(Z)\psi_m(z) \tag{3.3}$$

where M is the center of mass angular momentum and m is the relative angular momentum. It is easy to see that the relative coordinate part of the two-body wavefunction $\psi_m(z)$ is the same as the Laughlin wavefunction for two particles. In fact, the Laughlin wavefunction is the exact ground state for two particles interacting with any pairwise isotropic interaction $V(|\mathbf{r_i} - \mathbf{r_j}|)$ as long as we neglect mixing between Landau levels.

We can now expand any two-body pairwise interaction in the bases of the two-particle wavefunctions. The matrix elements of the interaction in these bases $\langle M', m'|V|M, m\rangle$ will depend only on the relative angular momentum values since the interaction is pairwise. Moreover if the interaction is isotropic — which is the case for the Coulomb potential, then it is diagonal in the relative angular momentum bases. $\langle M', m'|V|M, m\rangle = \delta_{M',M}\delta_{m',m}\langle m|V|m\rangle = \delta_{M',M}\delta_{m',m}V_m$ with V_m referred to as the Haldane pseudopotentials. We end up with,

$$V = \sum_{M,m} V_m \left|M, m\right\rangle \left\langle M, m\right| . \tag{3.4}$$

An interesting property of the Laughlin state (3.1) is that the lowest relative angular momentum carried by any two particles is m. This means that it is a zero energy state for any Hamiltonian that penalizes any two particles having relative angular momentum smaller than m. One such Hamiltonian in terms of the Haldane pseudopotentials would be

$$V'_m = 1 \;\; \text{if}\, m' < m \;\; \text{and} \;\; V'_m = 0 \;\; \text{if}\, m' \geq m. \tag{3.5}$$

This is a very short-ranged interaction in real space in contrast to the Coulomb interaction which is long-ranged. However looking at the Haldane pseudopotentials of the projected Coulomb interaction to the lowest Landau level as shown in Table

3.1 reveals that there is a big gap between successive Haldane pseudopotentials V_{m+2} and V_m[1]. This gap gets smaller as m increases. For sufficiently low m, a parent Hamiltonian of the form (3.5) with the Laughlin state as a zero energy state is a good description of Coulomb interactions in the lowest Landau level. For example, if $m = 3$, $V_1 \ggg V_3$ so keeping only V_1 is indeed a good approximation.

3.1.3 Laughlin State Excitations

Laughlin wavefunctions can be thought of as describing a uniform density fluid. Density perturbations to this fluid are therefore excitations of the Laughlin state. There are two types of charged excitations, quasi-hole excitations corresponding to a lower density and quasi-particle exciations corresponding to a higher density. Let's focus first on the quasi-hole excitations. The wavefunction describing one quasi-hole at position η at filling $\nu = 1/m$ is given by

$$\psi_{\mathrm{qh}}(z;\eta) = \prod_{i=1}^{N}(z_i - \eta)\prod_{k<l}(z_k - z_l)^m e^{-\sum_{i=1}^{n}|z_i|^2/4l_B^2}. \tag{3.6}$$

It can be seen as an extra zero introduced to the wavefunction. The quasi-hole carries a fractional charge $q_{\mathrm{qh}} = e/m$ since adding m quasi-holes at the same point describes a deficit of one electron charge at this point. In addition to the fractional charge, quasi-holes are an example of anyons, particles that exhibit fractional exchange statistics [77, 78]. The existence of anyons is exclusive to systems in two spatial dimensions. In the lowest Landau level, the quasi-holes are abelian anyons. Unlike fermions and bosons, exchanging two quasi-holes results in a complex phase,

$$\psi_{\mathrm{qh}}(z;\eta_1,\eta_2) = e^{i\pi\alpha}\psi_{\mathrm{qh}}(z;\eta_2,\eta_1) \tag{3.7}$$

where $\alpha < 1$ is the fractional statistics parameter. For a Laughlin state, $\alpha = 1/m$ [79]. The story is similar for quasi-particles, albeit with a more complicated wavefunction. They carry an opposite charge $q_{\mathrm{qe}} = -e/m$ and have the same fractional statistics as quasi-holes.

The existence of excitations with fractional charge and statistics is indeed a remarkable property of the fractional quantum Hall effect. Direct evidence of fractional charge has been found in shot-noise experiments [80] and recently, evidence for fractional statistics has been observed in interferometry experiments [81].

---

[1] m has to be odd for fermions and even for bosons.

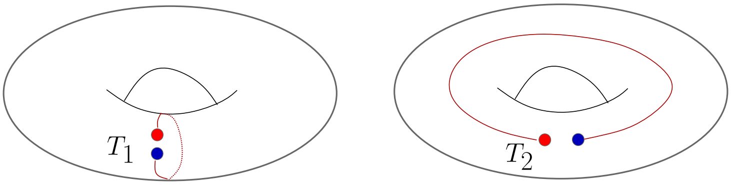

Figure 3.1: An illustration of the operations implemented by the two different operators T_1 and T_2 on the torus. The red and blue dots represent the quasi-hole and the quasi-particle.

3.1.4 Ground State Degeneracy

Another unique property of fractional quantum Hall states that only shows up when they are wrapped on a manifold with non-trivial topology is the many-body ground state degeneracy. It has been shown that such a degeneracy depends on the genus of the manifold [6]. The ground state degeneracy was first derived in quantum Hall systems with periodic boundary conditions (equivalent to a torus) by making use of the magnetic translation algebra [82]. Here, we provide a non-rigorous argument why the ground state has to be degenerate for fractional quantum Hall states at fillings $\nu = p/q$. The argument assumes the existence of a ground state with quasi-hole and quasi-particle excitations which have fractional statistics parameter $\alpha = 1/q$ at fillings $\nu = p/q$.

Let's consider a process on the torus where we create a pair of quasi-hole and quasi-particle, move the quasi-particle around the two different cycles of the torus then annihilate it with the quasi-hole again as illustrated in Figure 3.1. If T_1 is an operator that implements this process along the first cycle and T_2 is another operator that implements it along the second cycle, these two operators will not commute as a consequence of the fractional statistics of the quasi-hole and quasi-particle. They are related by

$$T_1 T_2 = e^{2\pi i/q} T_2 T_1. \tag{3.8}$$

This could be deduced by realizing that the product $T_1 T_2 T_1^{-1} T_2^{-1}$ is equivalent to taking the quasi-electron around the quasi-hole (see Figs. 4 and 5 in Ref. [6]) hence, the resulting phase. The operators T_1 and T_2 in the algebra (3.8) map a ground state to a different ground state therefore, the algebra (3.8) cannot be realized on a single ground state. The ground state has to be degenerate with at least q-fold degeneracy. The argument can be generalized to higher-genus surfaces. The degeneracy of the ground state has to be at least q^g where g is the genus of the surface.

Back to the Laughlin Argument.

The Laughlin argument discussed in section 2.2.1 can be modified to take into account the ground state degeneracy of fractional quantum Hall states. This is done by realizing that after inserting one unit of flux quantum, the spectrum of the system does not change but instead of returning to the same ground state we started with, the system is at a different ground state. One needs to insert q units of flux quantum to return to the same exact ground state given q-fold degeneracy. After q units of flux, a unit charge is pumped from one-side to the other therefore, a fractional charge e/q is pumped after inserting one unit of flux quantum.

3.1.5 Beyond Fillings $\nu = 1/m$

The Laughlin state is a good description of fractional quantum Hall states at fillings $\nu = 1/m$ due to the short-range nature of the effective interaction in the lowest Landau level. However, there are many fractional quantum Hall states that show at other fillings.

One way to explain the emergence of other quantum Hall states is through the hierarchy approach given in [76,83]. The idea is that the quasi-particles and quasi-hole themselves could form a quantum Hall liquid built over the initial quantum Hall state. This will change the density of the liquid, i.e. the effective filling fraction. For example, starting from $\nu = 1/m$ state, the quasi-particles and quasi-holes of this state could form a quantum Hall liquid that would contribute to the total filling fraction as

$$\nu = \frac{1}{m} \mp \frac{1}{2pm^2 \pm m} = \frac{1}{m \pm \frac{1}{2p}} \tag{3.9}$$

where p is a positive integer. The minus sign is for quasi-holes and the plus sign is for quasi-particles. The second term could be deduced by figuring out what the filling fraction of a Laughlin-like state made of quasi-holes or quasi-particles would look like. For example, for $m = 3$ and $p = 1$, the quasi-particle contribution results in $\nu = 2/5$ Jain state that has been observed experimentally (Figure 2.1). Furthermore, the quasi-holes and quasi-particles of the new state could themselves form a quantum Hall liquid thus modifying again the total filling fraction leading to a hierarchy given by

$$\nu = \cfrac{1}{m \pm \cfrac{1}{2p_1 \pm \cfrac{1}{2p_2 \pm \dots}}} \tag{3.10}$$

The hierarchy approach explains a wide range of the observed filling fractions with odd denominator in the lowest Landau level. In addition to the hierarchy picture, the sequence of the experimentally observed fractional quantum Hall states can be also explained through the language of composite fermions [84] which we briefly comment on.

A composite fermion is defined as an electron bound to $m-1$ flux quanta where m is odd. When placed in a magnetic field B, composite fermions therefore experience an effectively different magnetic field B^*. This implies that they also have a different filling factor ν^* than bare electrons with filling factor ν. It can be shown [85] if $B^* > 0$ that

$$\nu = \frac{\nu^*}{1+(m-1)\nu^*} \tag{3.11}$$

If composite fermions fill their lowest Landau level ($\nu^* = 1$) then this corresponds to electron filling $\nu = 1/m$. So the fractional quantum Hall effect at electron fillings $\nu = 1/m$ corresponds to an integer quantum hall effect of composite fermions. By integer filling more than one Landau level ($\nu^* > 1$), equation (3.11) gives the sequence $\nu = 2/5, 3/7, 4/9, \ldots$ for $m = 3$ which are the observed states to the left of $\nu = 1/3$ in Figure 2.1. Additional fractional quantum Hall states can also be built from composite fermions with $B^* < 0$. We refer the interested reader to the comprehensive book [86] for more details about the theory of composite fermions.

3.1.6 Halperin States

The Laughlin wavefunctions introduced in section 3.1.1 are spin-polarized. They do not take into account the spin degree of freedom of the underlying particles. This is usually motivated by the large Zeeman splitting between spin up and spin down particles in the presence of a strong magnetic field therefore at low energies, it suffices to consider only one type of spin. However, in a weak magnetic field or even in the absence of an external magnetic field, there is a need to generalize the Laughlin wavefunctions to take into account the spin of the particles. The Halperin states labeled (m_1, m_2, n) [87] read

$$\psi_{m_1,m_2,n}(z,w) = \prod_{i<j}^{N^\uparrow}(z_i - z_j)^{m_1} \prod_{k<l}^{N^\downarrow}(w_k - w_l)^{m_2} \prod_{i,k}(z_i - w_k)^n e^{-\sum_{i=1}^{N^\uparrow}|z_i|^2/4l_B^2 - \sum_{i=1}^{N^\downarrow}|w_i|^2/4l_B^2} \tag{3.12}$$

The set $\{z_i\}$ ($\{w_i\}$) are the positions of the spin up (down) particles. In fact, the construction above is not limited to spin only. It can be adopted for generic multi-component quantum Hall systems, i.e. quantum Hall systems with additional quantum numbers. The extra degree of freedom can be for example the valley degree of freedom in graphene-like systems or the layer degree of freedom in quantum Hall bilayers.

3.2 Fractional Chern Insulators

We have seen that it is possible to realize the integer quantum Hall effect in non-interacting lattice models in the absence of external magnetic fields. The key was that integer filling of topologically non-trivial bands with non-zero Chern numbers results in a quantized Hall response.

A natural follow-up is to wonder if this analogy can be extended to the fractional quantum Hall effect. Can we have interacting lattice models that realize a fractional quantum Hall effect in the absence of external magnetic fields? The answer to such question is not straightforward as there is a variety of different possible interacting many-body states in lattice models. However, there have been lots of theoretical and numerical studies suggesting that *Fractional Chern Insulators* (FCIs) can be realized in a number of lattice models. (For a detailed review, we refer the reader to Refs. [52, 53] and references therein).

3.2.1 Motivation

As rich as quantum Hall physics can be, the conventional setup for realizing this kind of physics is accompanied by challenges that severely hinder the possible prospects for real life applications. These challenges include the need to cool down the electron gases to very low temperatures and the need for very strong magnetic fields $B \sim 10\,\text{Tesla}$.

FCIs offer a route around this. Analogues of Landau levels (flat Chern bands) can exist without external magnetic fields as a consequence of the underlying topology of the band structure. In addition, the lattice provides a natural length scale set by the lattice constant that is typically smaller than the magnetic length scale. To give some numbers, a rough estimation of the magnetic length is $l_B \approx 26\,\text{nm}\,\sqrt{B}$ while a typical lattice constant of a material would be of the order $O(\mathring{A})$. This further implies that interactions on the lattice scale are greater than the magnetic length scale which means that FCI states could in principle have higher energy gaps thus surviving higher temperatures, a necessity towards any practical implementations.

In addition, as we shall discuss briefly later, the existence of flat bands with Chern numbers $C > 1$ opens the door towards new states that generally do not have a continuum analogue in terms of decoupled Landau levels.

3.2.2 FCI Phenomenology

We will first adopt a *phenomenological* approach in identifying suitable models for FCI phases. As a common guideline, we want to target lattice modes with bands that have properties close to Landau levels. Let's first demonstrate this using the lower band of the Haldane model (2.35). The Haldane model is far from being the ideal lattice model for realizing FCI states, but it is a good starting point. We need a number of ingredients.

A Nearly Flat Topological Band

Landau levels are perfectly flat so in targeting FCI states, it is indeed useful to minimize the dispersion of the lattice bands as much as possible so that interactions dominate. For the Haldane model, it is possible to minimize the bandwidth of the lower band by certain choices of the model parameters. Needless to say, the band has to carry a non-zero Chern number in analogy to Landau levels. When the Haldane model breaks time reversal symmetry and a gap opens, the lower band carries a Chern number $C = \pm 1$.

A Considerable Band Gap

In addition to a flat Chern band, it is useful to have a large band gap. A larger band gap means a larger window of interaction strength values V that keeps the relevant interacting physics restricted to the flat band. Schematically, we want a hierarchy of scales as follow,

$$W(\text{Bandwidth}) \lll V(\text{Interaction}) \lll \Delta(\text{Band gap}). \tag{3.13}$$

In diagnosing FCI states, we do not need to worry that much about satisfying this hierarchy as we are going to project all the physics to our band of interest anyway but such a hierarchy is indeed required in order to justify the projection procedure in the first place.

Minimal Berry Curvature Fluctuations

Landau levels are unique in the sense that they have perfectly uniform Berry curvature while generic lattice models show Berry curvature fluctuations. It is then desirable to have lattice models with minimized Berry curvature fluctuations. There is indeed a correlation between the stability of FCI states and Berry curvature fluctuations [88]. However, it is crucial to mention that the story is more complicated than this and the connection between minimizing Berry curvature fluctuations and stabilizing FCI states is not straightforward. This should only be seen from a phenomenological point of view when dealing with generic lattice models. Flattening the Berry curvature does not always improve the prospects of FCI states. Indeed, this was the subject of Paper III [50]. It turns out there is a vital role to quantum geometry of the Chern band in defining what is a *good* or *bad* Chern band for realizing FCI. We will elaborate more on this in section 3.3.

The ingredients above are not strict requirements but they serve as general guidelines for targeting lattice models with the potential to host FCI states.

The Choice of Interaction.

The type of interaction needed to stabilize FCI states is highly model dependent. It also depends on what kind of FCI states are targeted. Abelian FCI states tend to be stabilized when the interaction is short-ranged since model fractional quantum Hall states are ground states of short-ranged interactions as discussed in section 3.1.2. We shall target Laughlin states in the Haldane model so it makes sense to consider a very short-ranged interaction in real space. A fermionic interaction consisting only of the V_1 term (also known as the hollow-core interaction) (3.4) is not possible on the lattice since the lattice does not have the full rotational symmetry of the continuum needed for the pseudopotentials expansion. However a nearest neighbor density-density interaction is a good approximation.

$$H_{\text{int}} = U \sum_{\langle ij \rangle} :\rho_i \rho_j: \tag{3.14}$$

where $\rho_i = c_i^\dagger c_i$ is the density operator at site i. The full Hamiltonian then reads $H = H_0 + H_{\text{int}}$ with H_0 is the non-interacting Hamiltonian (2.34).

Once a *good* Chern band is identified, it is advantageous numerically to project all the physics onto this band. As discussed before, the projection is justified when the relevant energy scales are related like (3.13). Let's define a projector that projects onto the lowest band in the Haldane model, $\mathcal{P} = |u_0(\mathbf{k})\rangle \langle u_0(\mathbf{k})|$ with $u_0(\mathbf{k})$ is the Bloch eigenfunction of the lowest band. The projected Hamiltonian $H^{\text{proj}} = \mathcal{P} H \mathcal{P}$ is given by

$$H^{\text{proj}} = \sum_{\mathbf{k}} E_0(\mathbf{k}) d_{\mathbf{k}}^\dagger d_{\mathbf{k}} + \sum_{\mathbf{k}_1\mathbf{k}_2\mathbf{k}_3\mathbf{k}_4} V^{\text{proj}}_{\mathbf{k}_1\mathbf{k}_2\mathbf{k}_3\mathbf{k}_4} d_{\mathbf{k}_1}^\dagger d_{\mathbf{k}_2}^\dagger d_{\mathbf{k}_3} d_{\mathbf{k}_4} \tag{3.15}$$

$E_0(\mathbf{k})$ is the dispersion of the lowest band, $d_{\mathbf{k}}^\dagger$ and $d_{\mathbf{k}}$ are creation and annihilation operators of electron in the lowest band respectively. $V^{\text{proj}}_{\mathbf{k}_1\mathbf{k}_2\mathbf{k}_3\mathbf{k}_4}$ is the projected interaction matrix elements. For the interaction (3.14) projected onto the lowest band, they are given explicitly by

$$V^{\text{proj}}_{\mathbf{k}_1\mathbf{k}_2\mathbf{k}_3\mathbf{k}_4} = \\ U\delta_{\mathbf{k}_1\mathbf{k}_2=\mathbf{k}_3+\mathbf{k}_4}\left(u^*_{0A}(\mathbf{k}_1)u^*_{0B}(\mathbf{k}_2)u_{0B}(\mathbf{k}_3)u_{0A}(\mathbf{k}_4) + A \leftrightarrow B\right)\sum_{j=1,2,3} e^{i(\mathbf{k}_2-\mathbf{k}_3)\cdot\boldsymbol{\delta}_j} \tag{3.16}$$

where u_{0A} and u_{0B} are the components of the lowest band Bloch eigenfunction corresponding to the A and B sublattices respectively.

3.2.3 FCI Identification: Ground State Degeneracy and Spectral Flow

The projected Hamiltonian (3.15) is our starting point. We want to study it at fractional band fillings $\nu = p/q$. We do this through exact diagonalization, a standard technique that has proven very useful in diagnosing the quantum Hall problem. We know that fractional quantum Hall systems exhibit a ground state degeneracy once wrapped on a higher genus surface as argued in section 3.1.4. Therefore we expect FCI states to show similar behavior on higher genus surfaces. Numerically, wrapping our system on the torus $\mathbf{T}^2$ is done by imposing periodic boundary conditions. For a finite size system consisting of $N_x \times N_y$ unit cells, periodic boundary conditions restrict the momentum values to take

$$\mathbf{k} = \frac{n}{N_x}\mathbf{G}_1 + \frac{m}{N_y}\mathbf{G}_2\ , \quad n = [0, \ldots, N_x - 1]\ , \quad m = [0, \ldots, N_y - 1] \tag{3.17}$$

where $\mathbf{G}_1$ and $\mathbf{G}_2$ are two reciprocal lattice vectors.

In Figure 3.2(a), we show the many-body spectrum of the band-projected interacting Hamiltonian (3.15) of the Haldane model at filling $\nu = 1/3$. The interacting problem is also translationally invariant so the spectrum is labeled by total momentum $\mathbf{K}$ which we map it to take single values $\mathbf{K} \to K_x + N_xK_y$. We observe a 3-fold degeneracy with a gap much larger than the ground states splitting similar to what is expected from fractional quantum Hall states. In addition to the 3-fold degeneracy, the momentum label of each ground state can be predicted by applying an exclusion rule on the folded momentum $K_x + N_xK_y$ that gives the admissible FQH configurations in accordance to Haldane generalized statistics of FQH states derived by a number of different approaches [89–92]. For $\nu = 1/q$, the allowed momentum configurations of FQH ground states are those which have only one particle in q consecutive orbitals[2]. The momenta of the ground states in Figure

---

[2] For most cases, this simple counting based on folding the two dimensional momentum $\mathbf{K}$ works but a more involved counting was described in [93].

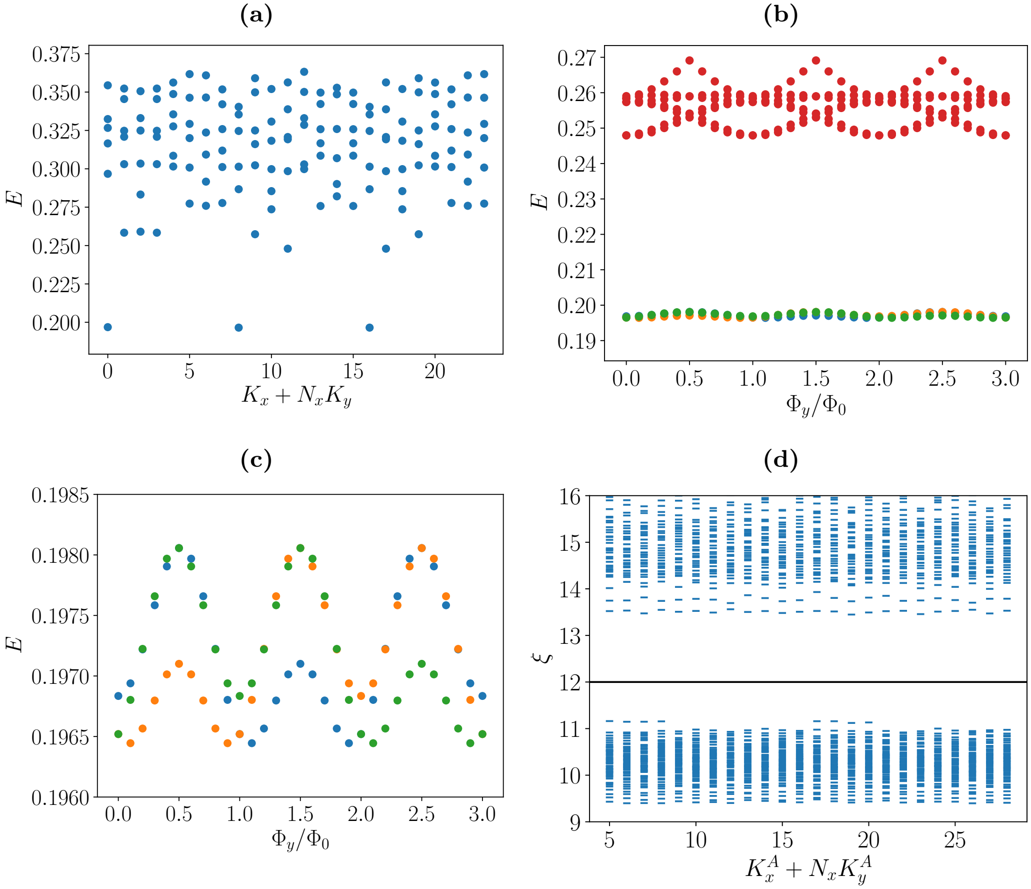

Figure 3.2: Identification of the FCI phase in the Haldane model: (a) The many-body spectrum at filling of $1/3$ for 8 particles on of lattice of 4×6 sites with periodic boundary conditions. (b) The spectral flow of the low-lying energy states as a function of the inserted flux Φ/Φ_0. The green, orange and blue colors correspond to the 3 degenerate ground states in different momentum sectors while the red states are higher energy states. (c) A close-up look of the spectral flow of the 3 degenerate ground states corresponding to different momentum sectors. (d) The particle entanglement spectrum for $N_A = 3$ particles after tracing out $N_B = 5$ particles. There are 1088 states below the black line.

3.2(a) indeed corresponds to the predicted momenta from the exclusion statistics.

In addition to the 3-fold degeneracy, it is possible to check the spectral flow of the ground states upon insertion of varying fluxes through the cycles of the torus. For instance, inserting a flux through the y-cycle of the torus $\Phi_y = l\Phi_0$ will modify the single particle momenta $k_y \to k_y + \frac{l}{N_y}\mathbf{G}_2$. In Figure 3.2(b) , we vary l from 0 to 3 and observe how the spectrum evolves. The 3 ground states remain gapped from the rest of the spectrum confirming the incompressibility of the system. The ground states flow among each other separated from the other states suggesting robust topological degeneracy. Since each ground state carries a different total momentum quantum number on the geometry used in this example, it is possible to track each one by assigning a different color to each. We show a close-up of this in Figure 2.3(c). After insertion of 3 units of flux quanta, the ground states are exactly the same. The energies are the same after 1 and 2 units of flux quantum as expected but the ground states are different. Based on the Laughlin argument discussed in section 2.2.1, this indicates that the system shows quantized Hall conductivity.

The ground state degeneracy in addition to the spectral flow hint that the underlying phase is a FCI state belonging to the Laughlin universality class. Moreover, to completely rule out competing states such as charge density waves (CDWs), one could look at the momentum space occupation. FQH are uniform density states thus we equivalently expect that FCI states have nearly uniform densities in momentum space. It is also possible to look at quasi-hole excitations of the ground state by slightly modifying the filling factor away from 1/3. The counting of quasi-hole exciations is also a signature of Laughlin states.

We describe next another technique used to identify FCI states based on the entanglement spectrum of the many-body ground states.

3.2.4 FCI Identification: Particle Entanglement Spectrum

Entanglement spectrum is another probe that can be used to identify different topological phases of matter. Assume we have a generic $d \times d$ dimensional many-body density matrix ρ written in some orthonormal bases $\{\mu\}$. Let's also assume that the system can be partitioned into two parts A and B so that the orthonormal basis can be decomposed into a tensor product of basis within each part $\{\mu\} = \{\mu^A \otimes \mu^B\}$ with $d = \dim_A \times \dim_B$ where $\dim_{A(B)}$ are the dimensions of the Hilbert spaces of subsystem A (B). We then have

$$\rho = \sum_{i,j=1}^{d} M_{ij} \left|\mu_i\right\rangle \left\langle\mu_j\right| = \sum_{ijkl} M_{ij;kl} \left|\mu_i^A \otimes \mu_j^B\right\rangle \left\langle\mu_k^A \otimes \mu_l^B\right| \tag{3.18}$$

By tracing out one of part of the system, say part B, we obtain the reduced density matrix ρ_A defined on subsystem A,

$$\rho_A = \mathrm{Tr}_B \rho \equiv e^{-H_A}. \tag{3.19}$$

The entanglement spectrum is defined as the spectrum $\{\xi_i\}$ of the Hamiltonian H_A. Furthermore, if we have a symmetry, implemented by a operator that commutes with the density matrix $[\rho, \mathcal{O}] = 0$, that can be decomposed into two parts $\mathcal{O} = \mathcal{O}_A + \mathcal{O}_B$, it follows that $[\rho_A, \mathcal{O}_A] = 0$ so it is possible to label the spectrum with the quantum numbers of $\mathcal{O}_A$.

The entanglement spectrum was initially studied by Li and Haldane [94] to characterize topological order in quantum Hall states. There are many ways to partition a system into two parts. In the initial study, the *orbital* entanglement spectrum was used which amounts to partitioning the system in angular momentum space. It was then hypothesized that low energy structure of the entanglement spectrum is universal to all states within the same universality class or with the same topological order. For example, the low energy part of the entanglement spectrum of model fractional quantum Hall states (e.g Laughlin states) is identical to the one obtained by exact diagonlization of Coulomb interactions in the lowest Landau levels at fillings where the model fractional quantum Hall state is expected to be a good description. This hypothesis was tested numerically on many fractional quantum Hall states and was extended to fractional Chern insulator states as a way to confirm that these states are in the same universality class as their analogous fractional quantum Hall states [95].

Moreover, different kinds of cuts contain different information about the system. When the system is cut in real space or equivalently orbital space, the low energy part of the entanglement spectrum contains information about the allowed edge excitations of the system. Here, we are going to discuss *particle* entanglement spectrum (PES) [96] which is obtained by doing a cut in particle space by tracing out a number of particles. If we have a generic many-body wavefunction $|\Psi\rangle$ for N particles that is written in the occupation bases of a number of orbitals

$$|\Psi\rangle = \sum_i c_i \, |\alpha_i; n_1 n_2 \ldots n_{N_o}\rangle \tag{3.20}$$

with α_i labeling Fock basis i that has a configuration $n_1 n_2 \ldots n_{N_o}$ with n_i the occupation of each orbital. For instance, the orbitals can be the different momentum points corresponding to a finite number of unit cells. The basis above have a fixed number of particles $\hat{N} |\alpha_i\rangle = N$ with $\hat{N} = \sum_{i=1}^{N_o} \hat{n}_i$. They can be decomposed into basis of N_A and N_B particles $N = N_A + N_B$, $|\alpha_i\rangle = |\alpha_i^A\rangle \otimes |\alpha_i^B\rangle$ with $\hat{N} |\alpha_i^A\rangle = N_A$ and $\hat{N} |\alpha_i^B\rangle = N_B$,

$$|\Psi\rangle = \sum_{ij} c_{ij} \, |\alpha_i^A\rangle \otimes |\alpha_j^B\rangle \, . \tag{3.21}$$

The reduced density matrix is obtained by tracing out N_B particles of the density matrix $\rho = |\Psi\rangle\langle\Psi|$,

$$\rho_{N_A} = \mathrm{Tr}_{N_A}\rho \equiv e^{-H_{N_A}}. \tag{3.22}$$

The eigenvalues of H_{N_A} form the particle entanglement spectrum. For d degenerate ground states $|\Psi_i\rangle$, the density matrix is modified to be $\rho = \frac{1}{d}\sum_{i=1}^{d}|\Psi_i\rangle\langle\Psi_i|$. The particle entanglement spectrum carries information about the number of allowed quasi-hole states. It was conjectured and numerically checked for many models that the number of states in the low-energy part of the particle entanglement spectrum matches the number of quasi-hole states for N_A particles in N_O orbitals. This number is identical to the number of allowed configurations that respect the Haldane generalized exclusion principle [89].

In Figure 3.2(d), we calculate the particle entanglement spectrum for the 3-degenerate ground states obtained on a geometry of $N = 8$ particles in a $N_x \times N_y = 4 \times 6$ lattice. We trace out $N_B = 5$ particles and keep $N_A = 3$. The spectrum is labeled by the total momentum $K_x^A + N_x K_y^A$ since it is still a good quantum number after partitioning the system. We observe a clear gap which is essential in defining the low-energy part of the entanglement spectrum. There are 1088 states below this gap. For a Laughlin state on the torus at filling $\nu = 1/3$, the admissible configuration are those which have one particle at most in each 3 consecutive orbitals. For a system with $N_A = 3$ particles in a 4×6 lattice, the number of configurations with at most one particle in each 3 consecutive orbitals is exactly 1088 which is the same number of states below the gap in the particle entanglement spectrum. This therefore provides a smoking gun evidence that the FCI state obtained here is in the same universality class as the Laughlin state.

3.2.5 Higher Chern Number FCIs

It is possible to demonstrate adiabatic continuity between the FCI states in bands with Chern number $|C| = 1$ and the corresponding FQH states. The FCI states are obtained in lattice systems while the FQH states are obtained in the continuum. However, it is possible to construct Wannier wavefunctions on the lattice that mimics Landau levels in the Landau gauge [97] thus allowing a direct comparison between the two.

On the other hand, FCI states have been shown to occur in bands with higher Chern number $|C| > 1$ [98]. The ground state degeneracies and entanglement spectrum properties reveal that those higher Chern number FCI states share lots of similarities with usual FQH states. By formulating a lattice composite fermions theory [99], it is possible to predict a series of filling fractions at which FCI states are possible. For fermions, they are given by

$$\nu = \frac{r}{r|kC| + 1} \tag{3.23}$$

with r is a non-zero integer and k is an even positive integer. An important distinction compared to the $|C| = 1$ case is that a generic $|C| > 1$ band cannot be mapped into C decoupled Landau levels. So the FCI states in higher Chern number bands do not have a straightforward continuum Landau levels counterpart in that sense. Nevertheless, it is possible to construct a Bloch-like basis in C component Landau levels that allows direct comparison between FCI states and FQH states [100]. Although those bases entangle the real space degrees of freedom with internal degrees of freedom that comes from the higher Chern number, their presence allows us to determine all the model FQH states and pseudopotentials that have generic FCI counterparts.

3.3 Ideal Chern Bands

In the previous sections, we have provided evidence that it is generally desirable to have Chern bands that mimic the properties of the lowest Landau level (LLL) such that fractional filling of these Chern bands could give rise to FCIs. The purpose of this section is to phrase these observations in a more concrete way. In order to do that, we need to study the properties of the lowest Landau level and identify conditions under which a generic Chern band is similar.

3.3.1 The GMP Algebra

We are interested in studying the algebra of density operators in the lowest Landau level. The density operator in momentum space is defined as $\rho_{\mathbf{q}} = e^{i\mathbf{q}\cdot\hat{\mathbf{r}}}$. Recall in section 2.1.1, the position operator $\hat{\mathbf{r}}$ can be decomposed into two operators corresponding to the relative and guiding center coordinates $\boldsymbol{\eta}$ and $\mathbf{R}$ respectively as shown in equation (2.16).

Since, we are only interested in the lowest Landau level (LLL), we project our density operator to this level, $\bar{\rho}_{\mathbf{q}} \equiv \mathcal{P}_{\mathrm{LLL}}\rho_{\mathbf{q}}\mathcal{P}_{\mathrm{LLL}}$ where $\mathcal{P}_{\mathrm{LLL}}$ is a projector to LLL. This gives us $\bar{\rho}_{\mathbf{q}} = e^{-q^2 l_B^2/4} e^{i\mathbf{q}\cdot\mathbf{R}}$. To see this, recall that the Hamiltonian (2.4) commutes with the operator $\mathbf{R}$ and is only a function of $\boldsymbol{\eta}$. The operator $\boldsymbol{\eta}$ is the same operator as $\boldsymbol{\Pi}$ in equation (2.4) (multiplied by the square of the magnetic length) which can be decomposed into the annihilation and creation operators a and $a^\dagger$ defined in equation (2.5) so that $\eta_x \sim a^\dagger + a$ and $\eta_y \sim a^\dagger - a$. The calculation is quite similar to evaluating expectation values of position and momentum operators in the standard problem of the Harmonic oscillator. After some lengthy algebra and using that the lowest Landau level $|\psi\rangle_{\text{LLL}}$ is annihilated by the operator a, one gets the stated result above.

The operator $e^{i\mathbf{q}\cdot\mathbf{R}}$ can be understood as the generator of center of mass (guiding center) translations which generates the massively degenerate states in a single Landau level. The projected densities $\bar{\rho}_{\mathbf{q}}$ obey the following algebra,

$$[\bar{\rho}_{\mathbf{q}_1}, \bar{\rho}_{\mathbf{q}_2}] = 2i\sin(\frac{\mathbf{q}_1 \wedge \mathbf{q}_2 l_B^2}{2})e^{\mathbf{q}_1\cdot\mathbf{q}_2 l_B^2/2}\bar{\rho}_{\mathbf{q}_1+\mathbf{q}_2} \tag{3.24}$$

where $\mathbf{q}_1 \wedge \mathbf{q}_2 = \hat{z}\cdot(\mathbf{q}_1 \times \mathbf{q}_2)$. This algebra is known as the Girvin-MacDonald-Platzman (GMP) algebra [101] or the W_∞ algebra. It shows up in different contexts in the quantum Hall problem, most notably in calculating magneto-roton excitations of the quantum Hall liquid. It is easily derived by using the commutation relations $[R_x, R_y] = -il_B^2$.

Next, for a Chern band, we would like to derive the corresponding expression for the projected density operator. Assuming we have an N band model of the form (2.26), the projector to the Chern band of interest is given by $P_n = \sum_{\mathbf{k}} |\mathbf{k}, n\rangle \langle\mathbf{k}, n|$. Therefore, the projected density operator is defined as $P_n\rho_{\mathbf{q}}P_n \equiv \bar{\rho}_{\mathbf{q}}$. To first order in $\mathbf{q}$, the commutator $[\bar{\rho}_{\mathbf{q}_1}, \bar{\rho}_{\mathbf{q}_2}]$ gives

$$[\bar{\rho}_{\mathbf{q}_1}, \bar{\rho}_{\mathbf{q}_2}] = i\mathbf{q}_1 \wedge \mathbf{q}_2 \sum_{\mathbf{k}} \Omega^n(\mathbf{k})\,|\mathbf{k}, n\rangle\langle\mathbf{k}, n| + O(q^2) \tag{3.25}$$

where $\Omega^n(\mathbf{k})$ is the Berry curvature (2.30) of the band n. The expression (3.25) agrees with the GMP algebra (3.24) to first order in $\mathbf{q}$ if the Berry curvature $\Omega^n(\mathbf{k})$ is constant in momentum space $\Omega^n(\mathbf{k}) = \bar{\Omega}^n$ which supports the expectation that minimal Berry curvature fluctuations are preferred.

However, this agreement is only in the long wavelength limit where the algebra closes. Assuming, the Berry curvature is constant and moving on to higher orders in $\mathbf{q}$, one finds [102] to third order,

$$\begin{aligned}[\bar{\rho}_{\mathbf{q}_1}, \bar{\rho}_{\mathbf{q}_2}] &= i\mathbf{q}_1 \wedge \mathbf{q}_2\bar{\Omega}^n(P_n - iP_n(\mathbf{q}_1+\mathbf{q}_2)\cdot\hat{\mathbf{r}}P_n) \\ &-\frac{i}{2}\sum_{a,b,c}\Bigg(\frac{q_{1a}q_{2b}q_{2c}}{2}[P_n\hat{r}_aP_n, P_n(\hat{r}_bQ_n\hat{r}_c + \hat{r}_cQ_n\hat{r}_b)] \\ &-\frac{q_{1a}q_{1b}q_{2c}}{2}[P_n\hat{r}_cP_n, P_n(\hat{r}_aQ_n\hat{r}_b + \hat{r}_bQ_n\hat{r}_a)]\Bigg) + O(q^4)\end{aligned} \tag{3.26}$$

With $Q_n = 1 - P_n$. We see that the expression (3.26) agrees with (3.24) to third order if the last two terms vanish. This will happen if the Fubini-Study metric

$g^n_{ab}(\mathbf{k})$ of the band is constant. To see this, recall the definition of the Fubini-Study metric in equation (2.29) and notice that the operator $\hat{\mathbf{r}}$ is a derivative in momentum space.

So in addition to the constancy of the Berry curvature, we require the Fubini-Study metric of the Chern band also to be constant so that the GMP algebra is satisfied up to third order. This analysis introduces the fluctuations of the Fubini-Study metric in momentum space as another ingredient for identifying suitable bands for FCIs. Indeed, the Fubini-Study metric in a Landau level is constant [103]. The last ingredient we need for the density operators to satisfy the GMP algebra (or more precisely a metric-dependent generalization) at all orders is the saturation of the inequality (2.31) which means that $\mathrm{tr}R^n_{ab}(\mathbf{k}) = 0$ or $\mathrm{tr}g^n(\mathbf{k}) = |\Omega^n(\mathbf{k})|$ at all momentum points. Writing this condition explicitly gives us

$$\langle \mathbf{k}, n| \, (\hat{x} + i\hat{y}) Q_n (\hat{x} - i\hat{y}) \, |\mathbf{k}, n\rangle = 0 \tag{3.27}$$

which is equivalent to the condition,

$$Q_n(\hat{x} - i\hat{y})P_n = P_n(\hat{x} + i\hat{y})Q_n = 0. \tag{3.28}$$

Writing the density operators as $\rho_{\mathbf{q}} = e^{\frac{i}{2}(q_x - iq_y)(x+iy) + \frac{i}{2}(q_x+iq_y)(x-iy)}$ and using the condition (3.28) while still assuming that both the Berry curvature and the Fubini-Study metric are constants in the Brillouin zone, the projected density operators are found to satisfy the following algebra

$$[\bar{\rho}_{\mathbf{q}_1}, \bar{\rho}_{\mathbf{q}_2}] = 2i \sin\left(\frac{\mathbf{q}_1 \wedge \mathbf{q}_2 l_B^2}{2}\right) e^{q_{1a} g^n_{ab} q_{2b}} \bar{\rho}_{\mathbf{q}_1+\mathbf{q}_2} \tag{3.29}$$

which is a metric-dependent generalization of the algebra (3.24).

To summarize, in order for a Chern band to resemble the lowest Landau level from an algebraic point of view, the Berry curvature and the Fubini-Study metric have to be constant in the Brillouin zone in addition to the saturation of the inequality (2.31), also known as the *trace condition*. The algebra (3.29) is quite special and in fact cannot be satisfied in any lattice model described by a tight-binding Hamiltonian as we proved in Paper III [50].

3.3.2 Remarks Regarding the Trace Condition

We have seen that FQH model wavefunctions are quite special. For instance, we have shown in section 3.1.2 that the Laughlin state is an exact zero energy state for a specific short ranged interaction defined by a set of Haldane psuedopotentials. Many FQH states are zero modes for toy Hamiltonians describing short-ranged interactions. This property does not necessarily rely on the Berry curvature or the Fubini-Study metric to be constant but it does rely on satisfying the trace condition (2.31) (in another words, $\mathrm{tr}g^n(\mathbf{k}) = |\Omega^n(\mathbf{k})| \;\forall\mathbf{k}$).

We will not discuss the details of this but it is worth mentioning that starting from a Chern band that satisfies the trace condition, it is possible to derive to an exact lowest Landau level description [104, 105]. This description utilises continuum descriptions of lattice models instead of tight-binding descriptions. We shall see in the next chapter examples of continuum descriptions of lattice systems in the context of moiré superlattices. The band geometry fluctuations are generally reflected on the effective interaction in the lowest Landau level description that becomes no longer fully rotationally invariant or independent of the center of mass coordinates but certain properties are preserved such as the existence of zero modes for special short-ranged interactions.

Chapter 4

A Survey of Moiré Systems

In this chapter, we discuss the physics of a new class of Van der Waals heterostructures that has been shown to be a versatile platform for strongly correlated physics. We follow the recent literature and refer to them as moiré systems since they show moiré patterns, that is the emergence of a large unit cell structure due to a relative twist or a slight mismatch in the lattice constants between two adjacent materials.

First we briefly review the physics of graphene that serves as a building block for many of the moiré systems we are interested in. After, we discuss a number of graphene-based moiré systems. We conclude the chapter by a brief introduction to semiconductor transition metal dichalcogenides (TMDs) and their moiré heterostructures.

4.1 Graphene

Graphene is a two dimensional material made of carbon atoms with a hexagonal lattice structure. It shows a unique set of properties that distinguish it from other two dimensional materials in terms of thickness, strength, electron mobility and thermal and electrical conductivity making it promising for numerous applications (For a comprehensive review, see Ref. [1]).

The electronic properties of graphene are mainly governed by electrons in the π bonds that are made out of the p_z orbitals on the hexagonal lattice while the other s, p_x and p_y orbitals combine in a sp^2 hybridized orbital resulting in the so-called σ bond. The overlap between the p_z orbitals and the other orbitals is zero so they can be treated separately. The problem of electrons hopping on a hexagonal lattice has been studied theoretically long before graphene was made in the lab [106]. Such a problem shows many interesting aspects in relation to relativistic high energy physics. The electrons around the Fermi level have a linear dispersion analogous to relativistic massless Dirac fermions.

4.1.1 Tight Binding Model

We encountered a similar problem for the Haldane model discussed in section 2.4. The difference here is that we consider only real next nearest hoppping ($\phi = 0$ in equation (2.34)). For completeness, we will re-derive again the result here. A tight binding Hamiltonian that takes into account nearest neighbor and next neighbor hopping is then given by

$$H = -\sum_{\langle i,j\rangle} t_0 c^\dagger_{i,A} c_{j,B} - \sum_{\langle\langle i,j\rangle\rangle} \gamma_0 (c^\dagger_{i,A} c_{j,A} + c^\dagger_{i,B} c_{j,B}) + \text{h.c} \tag{4.1}$$

where $c^\dagger_{i,\alpha}(c_{i,\alpha})$ creates (annhilates) an electron on site $\mathbf{R}_i$ and sublattice $\alpha = A, B$. There are 3 nearest neighbors given by the vectors $\boldsymbol{\delta}_1 = a(\frac{\sqrt{3}}{2}, \frac{1}{2})$, $\boldsymbol{\delta}_2 = a(-\frac{\sqrt{3}}{2}, \frac{1}{2})$ and $\boldsymbol{\delta}_3 = a(0, -1)$ shown in Figure 4.1(a) with a the carbon-carbon atomic distance.

In addition, there are 6 next-nearest neighbors given by the primitive lattice vectors $\mathbf{a}_1 = \sqrt{3}a(1, 0)$, $\mathbf{a}_2 = \sqrt{3}a(\frac{1}{2}, -\frac{\sqrt{3}}{2})$, $-\mathbf{a_1}$, $-\mathbf{a}_2$, $\mathbf{a}_1 - \mathbf{a}_2$, and $\mathbf{a}_2 - \mathbf{a}_1$. The reciprocal lattice is also a triangular lattice spanned by the vectors $\mathbf{G}_i$, defined through $\mathbf{a}_i \cdot \mathbf{G}_j = 2\pi\delta_{ij}$, and given by $\mathbf{G}_1 = \frac{4\pi}{3a}(\frac{\sqrt{3}}{2}, \frac{1}{2})$ and $\mathbf{G}_2 = \frac{4\pi}{3a}(0, 1)$. The resulting first Brillouin zone is a hexagon as shown in Figure 4.1(b). To obtain the dispersion, we Fourier transform the Hamiltonian (4.1) to momentum space by defining $c_{\mathbf{k},\alpha} = \frac{1}{\sqrt{N}} \sum_i c_{i,\alpha} e^{-i\mathbf{k}\cdot\mathbf{R}_i}$ for N unit cells and making use of the orthogonality relations. We end up with,

$$H = \sum_{\mathbf{k}} (c^\dagger_{\mathbf{k},A} \;\; c^\dagger_{\mathbf{k},B}) \begin{pmatrix} -\gamma_0 f_2(\mathbf{k}) & -t_0 f_1^*(\mathbf{k}) \\ -t_0 f_1(\mathbf{k}) & -\gamma_0 f_2(\mathbf{k}) \end{pmatrix} \begin{pmatrix} c_{\mathbf{k},A} \\ c_{\mathbf{k},B} \end{pmatrix} \tag{4.2}$$

with

$$\begin{aligned} f_1(\mathbf{k}) &= (2e^{-ik_y \frac{a}{2}} \cos(\frac{\sqrt{3}}{2} k_x a) + e^{ik_y a}) \\ f_2(\mathbf{k}) &= (2\cos(\sqrt{3}k_x a) + 4\cos(\frac{3}{2}k_y a)\cos(\frac{\sqrt{3}}{2}k_x a). \end{aligned} \tag{4.3}$$

The energy eigenvalues are then given by

$$E(\mathbf{k}) = \pm t_0 \sqrt{3 + f_2(\mathbf{k})} - \gamma_0 f_2(\mathbf{k}). \tag{4.4}$$

The resulting band structure is shown in Figure 4.1(c). We notice that the valence and conduction bands touch at the Brillouin zone corners, $\mathbf{K}_+$ and $\mathbf{K}_-$.

4.1.2 Low Energy Model

Many of the peculiar properties of graphene come from the behavior in the low energy limit, i.e. around the band touching points. The momentum points that

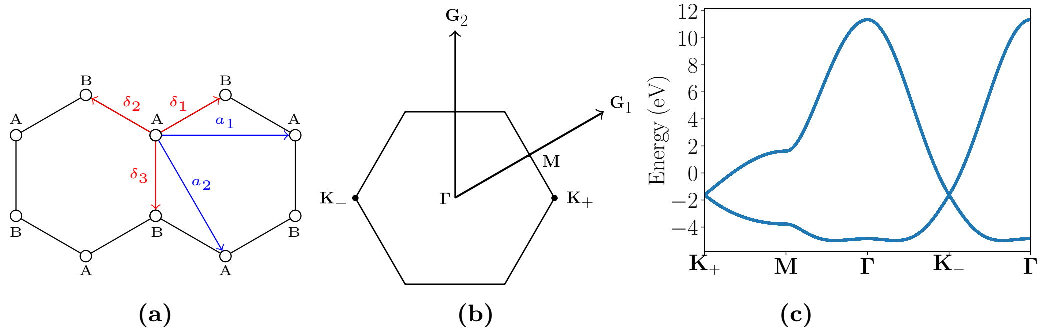

Figure 4.1: (a) Graphene real space lattice with the relevant nearest and next nearest hopping vectors. (b) Graphene Brillouin zone with the two Dirac points $\mathbf{K}_+$ and $\mathbf{K}_-$. (c) Band structure of graphene with $t_0 = 2.7\text{eV}$ and $\gamma_0 = 0.2t_0$ along a symmetry cut in the Brillouin zone.

contribute to this limit lie around the Brillouin zone corners. Out of the six corners, only two corners are inequivalent. Let us denote them by $\mathbf{K}_+ = \frac{4\pi}{3\sqrt{3}a}(1,0)$ and $\mathbf{K}_- = \frac{4\pi}{3\sqrt{3}a}(-1,0)$. The rest of the corners are related to these two points by appropriate translations by reciprocal lattice vectors. Expanding the dispersion relation (4.4) around the points $\mathbf{K}_+$ and $\mathbf{K}_-$, up to first order in momentum, yields

$$E(\mathbf{K}_+ + \mathbf{k}) = E(\mathbf{K}_- + \mathbf{k}) = 3\gamma_0 \pm v|\mathbf{k}| \tag{4.5}$$

with $v = 3t_0a/2$. The dispersion is linear in momentum and hence reminiscent of massless Dirac fermions but with a Dirac velocity v. For this reason, the points $\mathbf{K}_+$ and $\mathbf{K}_-$ are commonly referred to as Dirac points. It is not only the dispersion that is analogous to the dispersion of massless Dirac fermions but also the Hamiltonian around the Dirac points takes the form of a massless Dirac Hamiltonian. To see this, one expands (4.2) around the Dirac points. Defining $\Psi_\pm(\mathbf{k}) = (\psi_{\pm,A}(\mathbf{k}) \equiv c_{\mathbf{K}_\pm+\mathbf{k},A}, \psi_{\pm,B}(\mathbf{k}) \equiv c_{\mathbf{K}_\pm+\mathbf{k},B})^T$, we get up to first order dropping all constant energy shift terms,

$$\begin{aligned} H^+ &= \sum_{\mathbf{k}} \Psi_+^\dagger(\mathbf{k})(-v\mathbf{k}\cdot\boldsymbol{\sigma})\Psi_+(\mathbf{k}) \\ H^- &= \sum_{\mathbf{k}} \Psi_-^\dagger(\mathbf{k})(v\mathbf{k}\cdot\boldsymbol{\sigma}^*)\Psi_-(\mathbf{k}) \end{aligned} \tag{4.6}$$

with $\boldsymbol{\sigma} = (\sigma_x, \sigma_y)$ a vector of Pauli matrices. The momentum $\mathbf{k}$ is measured relative to the Dirac points. We see that up to first order in momentum, the Hamiltonian is decoupled into two massless Dirac Hamiltonians around each Dirac point.

The low energy physics comes from the two Dirac points at which the energy

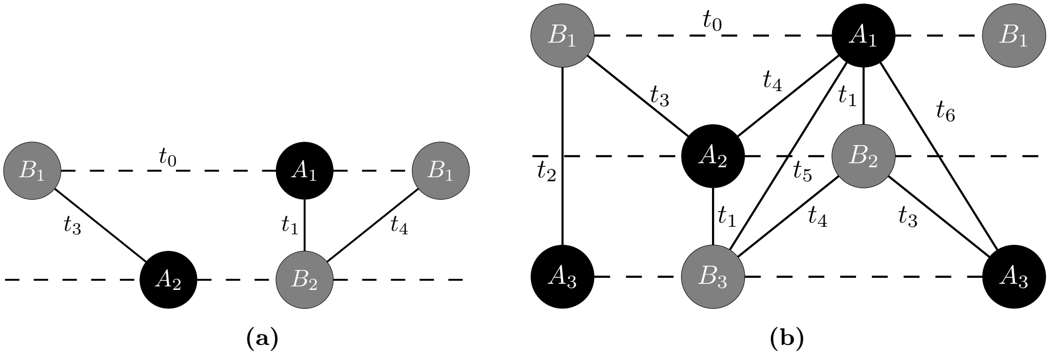

Figure 4.2: A side view of (a) AB stacked bilayer graphene and (b) ABC stacked trilayer graphene. The set of parameters $\{t_i\}$ denote various interlayer and intralayer hopping processes.

dispersion is maximum (minimum) for the valence (conduction) band. Each of these are commonly referred to as a *valley*. The valley is an emergent quantum number that the electrons acquire in the low energy limit. The Hamiltonian around one valley (equivalently one Dirac point) is related to the other by a spinless time reversal symmetry $\mathcal{T}$ that acts on the first quantized Hamiltonians as $h^{\pm}(\mathbf{k})$ as $\mathcal{T}h^{\pm}(\mathbf{k})\mathcal{T}^{-1} = h^{\pm}(-\mathbf{k})^* = h^{\mp}(-\mathbf{k})$.

4.2 Multilayer Graphene

In this section, we study generalizations of monolayer graphene to multiple layers. Similar to the previous sections, we are particularly interested in writing down a tight-binding model for a multilayer graphene system and study it in the low-energy limit retaining only the relevant degrees of freedom.

4.2.1 Bilayer Graphene

We begin by studying bilayer graphene formed by stacking two layers of graphene. Of particular importance is the type of stacking. Bilayer graphene exists in two stacking arrangements. AA stacking which means that the A(B) sublattices of the first layer are exactly aligned with the A(B) sublattices of the second layer and AB (Bernel) stacking where A sublattices of the first layer are aligned with B sublattices of the second layer. We will focus on AB stacked bilayer graphene since it is more stable than AA stacked bilayer graphene [107]. A schematic of the stacking of the layers is shown in Figure 4.2(a).

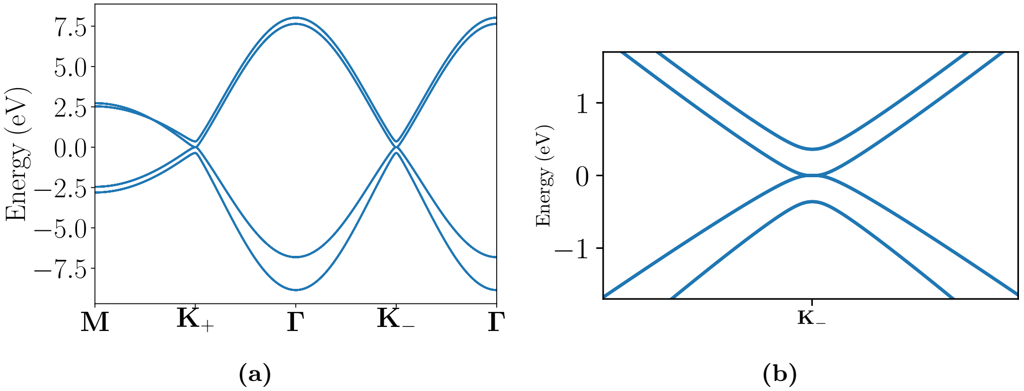

Figure 4.3: (a) Band structure of AB stacked bilayer graphene along a symmetry cut in the Brillouin zone (Figure 4.1(b)). (b) AB stacked bilayer graphene shows a quadratic dispersion around the Dirac points.

Working directly in momentum space, a tight-binding Hamiltonian for bilayer graphene is

$$H_{\mathrm{BLG}} = \sum_{\mathbf{k}} \begin{pmatrix} c^\dagger_{\mathbf{k},A_1} & c^\dagger_{\mathbf{k},B_1} & c^\dagger_{\mathbf{k},A_2} & c^\dagger_{\mathbf{k},B_2} \end{pmatrix} \begin{pmatrix} 0 & -t_0 f_1(\mathbf{k}) & -t_4 f_1^*(\mathbf{k}) & -t_1 \\ -t_0 f_1^*(\mathbf{k}) & 0 & -t_3 f_1(\mathbf{k}) & -t_4 f_1^*(\mathbf{k}) \\ -t_4 f_1(\mathbf{k}) & -t_3 f_1^*(\mathbf{k}) & 0 & -t_0 f_1(\mathbf{k}) \\ -t_1 & -t_4 f_1(\mathbf{k}) & -t_0 f_1^*(\mathbf{k}) & 0 \end{pmatrix} \begin{pmatrix} c_{\mathbf{k},A_1} \\ c_{\mathbf{k},B_1} \\ c_{\mathbf{k},A_2} \\ c_{\mathbf{k},B_2} \end{pmatrix} \tag{4.7}$$

where we took into account only nearest neighbor hopping. $f_1(\mathbf{k})$ is the nearest neighbor hopping function given in (4.3). In the low energy limit around the Dirac points, $f_1(\mathbf{K}_\pm + \mathbf{k}) \approx \frac{3}{2}a(\mp k_x + ik_y)$. The band structure along a symmetry cut is shown in Figure 4.3(a).

Due to the strong interlayer coupling t_1, the A_1 and B_2 degrees of freedom will *dimerize* meaning that they form bonding and anti-bonding states. This energy scale is captured by the top-most conduction band and the bottom-most valence band whereas the lower energy bands around the Dirac points arise mainly from hopping between the *non-dimer* B_1 and A_2 sites. In this case, it is possible to derive an effective Hamiltonian that keeps only B_1 and A_2. This Hamiltonian is valid in the low energy limit $|E| \ll t_0, t_1$ and well captures the physics around the Dirac point. To this end, we briefly outline a general recipe for integrating out higher energy degrees of freedom following [108].

We begin by arranging the basis of a generic Hamiltonian as $\Psi = (\Theta, \chi)^T$ where

Θ is a vector containing the low energy degrees of freedom which corresponds to the non-dimer lattice sites in our case and χ is a vector containing the remaining higher energy degrees of freedom corresponding to the dimer sites. In bilayer graphene, this means that $\Theta = (\psi_{B_1}(\mathbf{k}), \psi_{A_2}(\mathbf{k}))^T$ and $\chi = (\psi_{A_1}(\mathbf{k}), \psi_{B_2}(\mathbf{k}))^T$. with $\psi_\alpha(\mathbf{k})$ is the wavefunction component on a sublattice α. The eigenvalue equation of the Hamiltonian then reads

$$\begin{pmatrix} h_\Theta & u \\ u^\dagger & h_\chi \end{pmatrix} \begin{pmatrix} \Theta \\ \chi \end{pmatrix} = E \begin{pmatrix} \Theta \\ \chi \end{pmatrix}. \tag{4.8}$$

By using the second row of the above Hamiltonian, we can express χ as $\chi = (E - h_\chi)^{-1} u^\dagger \Theta$ then substituting back into the equation obtained from the first row which gives us,

$$\left[h_\Theta + u(E - h_\chi)^{-1} u^\dagger\right]\Theta = E\Theta. \tag{4.9}$$

Now we expand the above expression up to first order in E, yielding

$$\left[h_\Theta - u h_\chi^{-1} u^\dagger\right]\Theta = E(1 + u h_\chi^{-2} u^\dagger)\Theta. \tag{4.10}$$

Defining $\Phi = (1 + u h_\chi^{-2} u^\dagger)^{1/2}\,\Theta$ such that $\Phi^\dagger \Phi \approx 1$ to first order in E, we have $H^{\text{eff}}\Phi = E\Phi$ with the effective first quantized Hamiltonian,

$$\mathcal{H}^{\text{eff}} = (1 + u h_\chi^{-2} u^\dagger)^{-1/2}\left[h_\Theta - u h_\chi^{-1} u^\dagger\right](1 + u h_\chi^{-2} u^\dagger)^{-1/2}. \tag{4.11}$$

Expanding the Hamiltonian (4.7) around the Dirac points through $f_1(\mathbf{K}_\pm + \mathbf{k}) \approx \frac{3}{2} a(\mp k_x + i k_y)$ and then eliminating the dimer degrees of freedom A_1 and B_2 by using (4.11) gives us an a two-band effective Hamiltonian valid in the low energy limit $|E| \ll t_0, t_1$ around the Dirac points. The dominant contribution to the effective Hamiltonian around both valleys ± is given by

$$\mathcal{H}^{\text{eff}}_{\text{BLG},\pm} \approx \frac{-v^2}{t_1} \begin{pmatrix} 0 & (\mp k_x - i k_y)^2 \\ (\mp k_x + i k_y)^2 & 0 \end{pmatrix}. \tag{4.12}$$

We notice that the effective low energy Hamiltonian for bilayer graphene is quadratic in momentum hence it describes chiral quasiparticles with non-zero effective mass $\frac{1}{m_{\text{eff}}} = \frac{1}{\hbar^2}\frac{\partial^2 E}{\partial k^2}$, in contrast to the mono-layer case. Indeed this is the case if we zoom in around one of the Dirac points as indicated in Figure 4.3(b).

4.2.2 Trilayer Graphene

Adding one more layer of graphene enriches the stacking possibilities. We will focus on ABC stacked trilayer graphene [22] schematically shown in Figure 4.2(b).

A full tight binding Hamiltonian can be written in the basis of the two sublattices in each layer, however, we are only concerned here with the low energy limit near the Dirac points. Similar to bilayer graphene, the stronger coupling t_1 between aligned sublattices A_1 — B_2 and A_2 — B_3 will lead to dimerization accounting for four higher energy bands leaving two bands around the Dirac points. Integrating out the high energy degrees of freedom corresponding to dimer sites, using the same recipe described above for bilayer graphene, gives us a low-energy effective Hamiltonian in the basis of the non-dimer sites $(c_{\mathbf{k},A_1}, c_{\mathbf{k},B_3})^T$ with a dominant contribution,

$$\mathcal{H}^{\text{eff}}_{\text{TLG},\pm} \approx \frac{v^3}{t_1^2} \begin{pmatrix} 0 & (\mp k_x - ik_y)^3 \\ (\mp k_x + ik_y)^3 & 0 \end{pmatrix}. \tag{4.13}$$

The low energy Hamiltonian is cubic in momentum and describes also chiral electrons but with a higher degree of chirality.

Extending this analysis to N multilayers of graphene with Bernel stacking ($ABCDE\ldots$), the relevant low energy degrees of freedom are the two non-dimer sites, A_1 of the first layer and B_N of the N-th layer [109]. The low energy Hamiltonian around the Dirac points is then given by

$$\mathcal{H}^{\text{eff}}_{\text{N layers},\pm} \approx \frac{v^N}{(-t_1)^{N-1}} \begin{pmatrix} 0 & (\mp k_x - ik_y)^N \\ (\mp k_x + ik_y)^N & 0 \end{pmatrix}. \tag{4.14}$$

This defines a family of chiral electron Hamiltonians with degree of chirality N. When $N = 1$, corresponding to the monolayer graphene cases, the effective mass of the quasi-particles is zero while it is non-zero for $N > 1$.

4.3 Twisted Bilayer Graphene

We now turn to introduce twisted bilayer graphene (TBG) formed by taking two layers of monolayer graphene and twisting them relative to each other (Figure 1.2(a)). For tiny relative twists, the system acquires a new periodicity on a much bigger scale. The new moiré superlattice constant a_M scales roughly like $a_M \propto a/\theta$ for small twist angles θ where a is the lattice constant of monolayer graphene. Consequently, the new Brillouin zone, dubbed the moiré Brillouin zone (mBZ) is much smaller than the original monolayer graphene Brillouin zone.

The moiré superlattice is a triangular lattice with three important regions, AA, AB and BA as highlighted in Figure 4.4(a). The AA regions denote configurations where the A and B sublattices of one layer are locally aligned with the A and B sublattices of the other layer respectively where AB and BA denotes, as usual, alignment of different sublattices of the two layers.

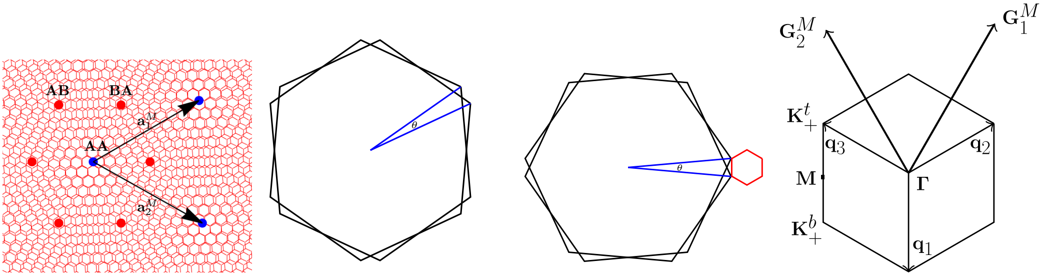

(a) **(b)** **(c)** **(d)**

Figure 4.4: (a) The moiré superlattice of twisted bilayer graphene. (b) A schematic of two twisted hexagons that is used for figuring out the crystallographic symmetries. (c) The rotated Brillouin zone of both layers results in a smaller moiré Brillouin zone shown in red. (d) The moiré Brillouin zone along with the relevant hopping vectors $\{\mathbf{q}_i\}$, the moiré Dirac points and the moiré reciprocal lattice vectors.

The moiré supercell is exactly periodic only at specific values of twist angles. The set of twist angles that gives rise to a commensurate structure are given by

$$\cos\theta(m,r) = \frac{3m^2+3mr+r^2/2}{3m^2+3mr+r^2} \tag{4.15}$$

where m and r are two positive coprime integers [110]. That being said, our goal here is to derive a continuum low energy model that captures all the low energy aspects at small twist angles regardless of if the actual system is commensurate or not. This has been done by Bistritzer and MacDonald [9] building on an earlier model [8].

4.3.1 The Continuum Model (CM)

Schematically the Hamiltonian of twisted bilayer graphene, denoted H_{TBG} can be decomposed to $H_{\text{TBG}} = H_0 + H_T$ where H_0 describes the physics within each individual layer and H_T describes tunneling between the two layers. H_0 is already known, it is the monolayer graphene Hamiltonian in the rotated coordinates. Our goal is to derive an expression for H_T.

In each layer of graphene, we expand the original Bloch wavefunctions at momentum $\mathbf{k}$ in terms of Wannier orbitals $|\mathbf{R}+\boldsymbol{\tau}_\alpha\rangle$ at each lattice site $\mathbf{R}+\boldsymbol{\tau_\alpha}$ in the layer where $\boldsymbol{\tau_A} = 0$ for sublattice A and $\boldsymbol{\tau_B} = \boldsymbol{\delta}_3 \equiv \tau_0$ for sublattice B (Figure

4.1(a)). This gives us

$$|\psi^t_{\mathbf{k}\alpha}\rangle = \frac{1}{\sqrt{N}} \sum_{\mathbf{R}} e^{i\tilde{\mathbf{k}}\cdot(\tilde{\mathbf{R}}+\tilde{\boldsymbol{\tau}}_\alpha)} \, |\tilde{\mathbf{R}} + \tilde{\boldsymbol{\tau}}_\alpha\rangle \tag{4.16}$$

$$|\psi^b_{\mathbf{p}\beta}\rangle = \frac{1}{\sqrt{N}} \sum_{\mathbf{R}'} e^{i\tilde{\mathbf{p}}\cdot(\tilde{\mathbf{R}}'+\tilde{\boldsymbol{\tau}}_\beta)} e^{i\tilde{\mathbf{p}}\cdot\boldsymbol{\Delta}} \, |\tilde{\mathbf{R}}' + \tilde{\boldsymbol{\tau}}_\beta\rangle \, . \tag{4.17}$$

The tilde over the coordinates implies that the coordinates have been rotated in each layer with the respective twist angle. This implies that in the top layer, $\tilde{\mathbf{k}} = \mathcal{R}_{\theta/2}\mathbf{k}$ and $\tilde{\mathbf{R}} = \mathcal{R}_{\theta/2}\mathbf{R}$ while in the bottom layer, $\tilde{\mathbf{p}} = \mathcal{R}_{-\theta/2}\mathbf{p}$ and $\tilde{\mathbf{R}}' = \mathcal{R}_{-\theta/2}\mathbf{R}'$. $\mathcal{R}_\theta$ is the rotation matrix with angle θ counterclockwise. Keeping that in mind and for convenience, we will drop the tilde.

The vector $\boldsymbol{\Delta}$ in the expression of the bottom layer Bloch function takes into account any relative displacement between the two layers. The tunneling matrix elements between sublattice α in the top latter and sublattice β in the bottom layer, denoted as $T^{\alpha\beta}_{kp}$, are given by

$$T^{\alpha\beta}_{kp} = \langle\psi^b_{\mathbf{p}\beta}|\, H_T \,|\psi^t_{\mathbf{k}\alpha}\rangle = \frac{1}{N} \sum_{\mathbf{R},\mathbf{R}'} e^{-i\mathbf{p}\cdot(\mathbf{R}'+\boldsymbol{\tau}_\beta+\boldsymbol{\Delta})} e^{i\mathbf{k}\cdot(\mathbf{R}+\boldsymbol{\tau}_\alpha)} \, \langle\mathbf{R}'+\boldsymbol{\tau}_\beta|\, H_T \,|\mathbf{R}+\boldsymbol{\tau}_\alpha\rangle. \tag{4.18}$$

So far, no approximations have been made but it is difficult to proceed without knowing the exact form of $\langle\mathbf{R}'+\boldsymbol{\tau}_\beta|\, H_T \,|\mathbf{R}+\boldsymbol{\tau}_\alpha\rangle$. We assume that the tunneling is a smooth function $t(\mathbf{r})$ of the spatial separation between the Wannier orbitals projected onto the graphene planes so that $\langle\mathbf{R}'+\boldsymbol{\tau}_\beta|\, H_T \,|\mathbf{R}+\boldsymbol{\tau}_\alpha\rangle = t(\mathbf{R}'+\boldsymbol{\tau}_\beta - \mathbf{R}+\boldsymbol{\tau}_\alpha)$. We then Fourier expand it, $t(\mathbf{r}) = \frac{1}{A}\int d^2q \, t_{\mathbf{q}} e^{i\mathbf{q}\cdot\mathbf{r}}$ where A is the area of the unit cell, giving us

$$T^{\alpha\beta}_{kp} = \frac{1}{NA} \int d^2q \sum_{\mathbf{R},\mathbf{R}'} e^{-i(\mathbf{p}-\mathbf{q})\cdot(\mathbf{R}'+\boldsymbol{\tau}_\beta+\boldsymbol{\Delta})} e^{i(\mathbf{k}-\mathbf{q})\cdot(\mathbf{R}+\boldsymbol{\tau}_\alpha)} t_{\mathbf{q}}. \tag{4.19}$$

Using orthonormality properties, the above expression is non-zero only if $\mathbf{p}-\mathbf{q} = \mathbf{G}^b_i$ and $\mathbf{k}-\mathbf{q} = \mathbf{G}^t_j$ for reciprocal lattice vectors of the top and bottom layers, $\mathbf{G}^t_i$ and $\mathbf{G}^b_j$ respectively. Substituting with the allowed values of $\mathbf{q}$ in the above expression, we end up with

$$T^{\alpha\beta}_{kp} = \sum_{\mathbf{G}^b_j,\mathbf{G}^t_i} t_{\mathbf{k}-\mathbf{G}^t_i} \, e^{-i\mathbf{G}^b_j\cdot(\boldsymbol{\tau}_\beta+\boldsymbol{\Delta})} \, e^{i\mathbf{G}^t_i\cdot\boldsymbol{\tau}_\alpha} \, \delta_{\mathbf{k}-\mathbf{G}^t_i,\mathbf{p}-\mathbf{G}^b_i}. \tag{4.20}$$

We see that momentum is conserved up to a difference of reciprocal lattice vectors of both layers, $\mathbf{k}-\mathbf{p} = \mathbf{G}^t_i - \mathbf{G}^b_j$. This further allows us to define moiré reciprocal lattice vectors $\{\mathbf{G}^M_{ij}\} = \{\mathbf{G}^t_i - \mathbf{G}^b_j\}$. In this formulation, the moiré superlattice periodicity is obtained by a linear combination of reciprocal lattice vectors of both layers. The basis vectors of the moiré reciprocal space $\mathbf{G}^M_1$ and $\mathbf{G}^M_2$ — such that any moiré reciprocal vector can be written as $\mathbf{G}^M_{mn} = m\mathbf{G}^M_1 + n\mathbf{G}^M_2$ for integer m and n, are then given by the smallest possible vectors obtained from taking linear combination of the set $\{\mathcal{R}_{\theta/2}\mathbf{G}_1, \mathcal{R}_{\theta/2}\mathbf{G}_2, \mathcal{R}_{-\theta/2}\mathbf{G}_1, \mathcal{R}_{-\theta/2}\mathbf{G}_2\}$ where $\mathbf{G}_1$ and $\mathbf{G}_2$ are the two reciprocal lattice basis vectors of monolayer graphene. This gives us

$$\mathbf{G}^M_1 = \mathcal{R}_{\theta/2}\mathbf{G}_1 - \mathcal{R}_{-\theta/2}\mathbf{G}_1 \;\;\&\;\; \mathbf{G}^M_2 = \mathcal{R}_{\theta/2}\mathbf{G}_2 - \mathcal{R}_{-\theta/2}\mathbf{G}_2. \tag{4.21}$$

Till now, the momentum $\mathbf{k}$ of the top layer and $\mathbf{p}$ of the bottom layer are measured with respect to the origin of the Brillouin zone of the monolayer graphene. With respect to a single valley (say valley $\mathbf{K}_+$), the momentum conservation condition is given by

$$\begin{aligned}(\mathbf{k} - \mathbf{K}^t_+) - (\mathbf{p} - \mathbf{K}^b_+) &= \mathcal{R}_{\theta/2}\mathbf{G}_i - \mathcal{R}_{-\theta/2}\mathbf{G}_j + \mathbf{q}_1\\ \bar{\mathbf{k}} - \bar{\mathbf{q}} &= \mathcal{R}_{\theta/2}\mathbf{G}_i - \mathcal{R}_{-\theta/2}\mathbf{G}_j + \mathbf{q}_1\end{aligned} \tag{4.22}$$

where $\bar{\mathbf{k}}$ and $\bar{\mathbf{q}}$ are momenta relative to valley $\mathbf{K}_+$ in the top and bottom layer respectively and $\mathbf{q}_1 = \mathbf{K}^b_+ - \mathbf{K}^t_+ = \mathcal{R}_{-\theta/2}\mathbf{K}_+ - \mathcal{R}_{\theta/2}\mathbf{K}_+$. An important observation from ab-initio calculations [8] is that $t_\mathbf{q}$ decays quickly with $\mathbf{q}$. We want to keep only the terms that minimizes $\mathbf{k} - \mathbf{G}^t_i$ in equation (4.20) where $\mathbf{k}$ now is in the vicinity of one valley. There are 3 such terms that contribute the most to $t_{\mathbf{k}-\mathbf{G}^t_i}$ and give rise to three distinct tunneling processes:

1. $\mathbf{G}^t_i = 0$ then $\bar{\mathbf{k}} - \bar{\mathbf{q}} = \mathbf{q}_1$
2. $\mathbf{G}^t_i = \mathcal{R}_{\theta/2}\mathbf{G}_3$ then $\bar{\mathbf{k}} - \bar{\mathbf{q}} = \mathcal{R}_{\theta/2}\mathbf{G}_3 - \mathcal{R}_{-\theta/2}\mathbf{G}_3 + \mathbf{q}_1 \equiv \mathbf{q}_2$
3. $\mathbf{G}^t_i = -\mathcal{R}_{\theta/2}\mathbf{G}_1$ then $\bar{\mathbf{k}} - \bar{\mathbf{q}} = \mathcal{R}_{-\theta/2}\mathbf{G}_1 - \mathcal{R}_{\theta/2}\mathbf{G}_1 + \mathbf{q}_1 \equiv \mathbf{q}_3$.

The second and third terms come from the fact that $\mathbf{G}_1$ and $-\mathbf{G}_3$ would take the valley $\mathbf{K}_+$ to the other two equivalent points in the monolayer graphene Brillouin zone. Keeping only these terms, we write the interlayer hopping (4.20) around one valley in a compact form in terms of a matrix where the diagonal terms represent hopping between the same sublattices (AA or BB) and the off diagonal terms represent hopping between different sublattices (AB or BA)

$$\begin{aligned}T(\mathbf{q}_1) &= \begin{pmatrix} w_0 & w_1 \\ w_1 & w_0 \end{pmatrix},\\ T(\mathbf{q}_2) &= e^{-i(\mathcal{R}_{-\theta/2}\mathbf{G}_3)\cdot\mathbf{\Delta}} \begin{pmatrix} w_0 & w_1 z \\ w_1 z^* & w_0 \end{pmatrix},\\ T(\mathbf{q}_2) &= e^{i(\mathcal{R}_{-\theta/2}\mathbf{G}_1)\cdot\mathbf{\Delta}} \begin{pmatrix} w_0 & w_1 z^* \\ w_1 z & w_0 \end{pmatrix}\end{aligned} \tag{4.23}$$

where $z = e^{-i\mathbf{G}_3\cdot\boldsymbol{\tau}_B}$. We notice that $\mathbf{G}_3\cdot\boldsymbol{\tau}_B = \mathbf{G}_1\cdot\boldsymbol{\tau}_B = -2\pi/3$. w_0 and w_1 describe the strength of same sublattice hopping and different sublattice hopping respectively and in principle can differ. In fact, the so-called relaxation effects, $w_0 \neq w_1$, play an important role for twisted bilayer graphene [111] and other moiré systems. By proper redefinition of the Bloch wavefunctions (4.16), the phases in front of $T(\mathbf{q}_n)$ (4.23) can be gauged away and we arrive at a general form of the interlayer hopping,

$$T(\mathbf{q}_n) = w_0 I + w_1\cos(2\pi(n-1)/3)\sigma_x + w_1\sin(2\pi(n-1)/3)\sigma_y \tag{4.24}$$

with $n = 1, 2, 3$. A similar calculation can be repeated for the other valley $\mathbf{K}_-$ to obtain a similar expression.

It is instructive to write the Hamiltonian we derived around one valley in the second quantized form,

$$\begin{aligned} H^+_{\text{TBG}} = \sum_{\mathbf{k}}(\Psi^\dagger_{t,+}(\mathbf{k})h^+_{\theta/2}(\mathbf{k})\Psi_{t,+}(\mathbf{k}) + \Psi^\dagger_{b,+}(\mathbf{k})h^+_{-\theta/2}(\mathbf{k})\Psi_{b,+}(\mathbf{k})) \\ + \sum_{\mathbf{k},i=1,2,3}\Psi^\dagger_{b,+}(\mathbf{k}+\mathbf{q}_i)T(\mathbf{q}_i)\Psi_{t,+}(\mathbf{k}) + \text{h.c} \end{aligned} \tag{4.25}$$

where $\Psi^\dagger_{l,+}(\mathbf{k}) = (\psi^{\dagger A}_{l,+}(\mathbf{k}), \psi^{\dagger B}_{l,+}(\mathbf{k}))^T$ with $\psi^{\dagger\alpha}_{l,+}(\mathbf{k})$ an operator that creates an electron with momentum $\mathbf{k}$ around valley $\mathbf{K}_+$ in layer $l = t, b$ and sublattice $\alpha = A, B$. $h^+_\theta(\mathbf{k})$ is the monolayer graphene low energy Hamiltonian around valley $\mathbf{K}_+$ rotated with angle θ, $h^+_\theta(\mathbf{k}) = h^+(\mathcal{R}_\theta\mathbf{k})$ with $h^+ = -v\mathbf{k}\cdot\boldsymbol{\sigma}$ is the low energy Dirac Hamiltonian we derived in equation (4.6). The Hamiltonian around the other valley $\mathbf{K}_-$ could be obtained by applying a time reversal transformation to (4.25).

4.3.2 Band Structure

A remarkable feature of twisted bilayer graphene, arguably the most prominent one, is the existence of flat bands with very narrow bandwidth around charge neutrality when the twist angle takes certain values referred to as *magic* angles. The first of these angles, and the most relevant to recent experiments, occurs around $\theta = 1.0° - 1.2°$. Around the first magic angle, the dispersion of the valence and conduction band is very small and the band velocity approaches zero. In Figure 4.5, the band structure of TBG near valley $\mathbf{K}_+$ is plotted around charge neutrality for different values of twist angles. One notices that the valence and conduction bands around the zero energy always cross at the new Dirac points $\mathbf{K}^t_+$ and $\mathbf{K}^b_+$ of the moiré Brillouin zone (Figure 4.4(d)). This can be attributed to a symmetry constraint that will be discussed later. The Dirac velocity around these points is

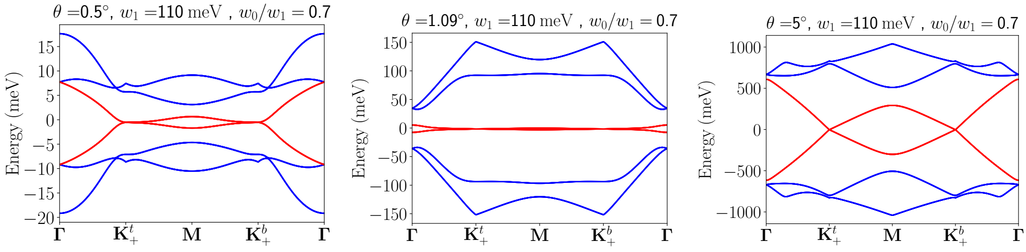

(a) **(b)** **(c)**

Figure 4.5: Band structure of twisted bilayer graphene along a symmetry cut in the moiré Brillouin zone (Figure 4.4(d)) for a number of twist angles. The valence and conduction bands are colored in red.

strongly renormalized compared to the original Dirac velocity of the single layer graphene and it almost vanishes near the magic angles (Figure 4.5(b)).

To gain some insights about the renormalization of the velocity near the Dirac points of the moiré Brillouin zone, we derive an effective Hamiltonian around these points. To do so, we examine the Hamiltonian (4.25) perturbatively in the limit $\mathbf{k} \to 0$ which corresponds to momenta near the Dirac point $\mathbf{K}^t_+$. We will consider a momentum cutoff corresponding to an 8 band Hamiltonian given by

$$\mathcal{H} = \begin{pmatrix} h^+_{\theta/2}(\mathbf{k}) & T(\mathbf{q}_1) & T(\mathbf{q}_2) & T(\mathbf{q}_3) \\ T^\dagger(\mathbf{q}_1) & h^+_{-\theta/2}(\mathbf{k}+\mathbf{q}_1) & 0 & 0 \\ T^\dagger(\mathbf{q}_2) & 0 & h^+_{-\theta/2}(\mathbf{k}+\mathbf{q}_2) & 0 \\ T^\dagger(\mathbf{q}_3) & 0 & 0 & h^+_{-\theta/2}(\mathbf{k}+\mathbf{q}_3) \end{pmatrix} \tag{4.26}$$

written in the basis $\Psi = (\Psi_{t,+}(\mathbf{k}), \Psi_{b,+}(\mathbf{k}+\mathbf{q}_1), \Psi_{b,+}(\mathbf{k}+\mathbf{q}_2), \Psi_{b,+}(\mathbf{k}+\mathbf{q}_3))$. The 8 band Hamiltonian serves as a good first approximation to the band structure of TBG. In addition, the parameter dependence of the low energy monolayer graphene Hamiltonian $h^+_\theta(\mathbf{k})$ on the angle θ is negligible for small twist angles, and therefore we will assume $h^+_\theta(\mathbf{k}) \approx -v\mathbf{k}\cdot\boldsymbol{\sigma}$.

The Hamiltonian (4.26) can be further decomposed to a $\mathbf{k}$ independent part $\mathcal{H}^{(0)}$ and a $\mathbf{k}$ dependent part $\mathcal{H}^{(1)}$ given by,

$$\mathcal{H}^{(0)} = \begin{pmatrix} h_0 & T(\mathbf{q}_1) & T(\mathbf{q}_2) & T(\mathbf{q}_3) \\ T^\dagger(\mathbf{q}_1) & h_1 & 0 & 0 \\ T^\dagger(\mathbf{q}_2) & 0 & h_2 & 0 \\ T^\dagger(\mathbf{q}_3) & 0 & 0 & h_3 \end{pmatrix} \tag{4.27}$$

$$\mathcal{H}^{(1)} = \begin{pmatrix} -v\mathbf{k}\cdot\boldsymbol{\sigma} & 0 & 0 & 0 \\ 0 & -v\mathbf{k}\cdot\boldsymbol{\sigma} & 0 & 0 \\ 0 & 0 & -v\mathbf{k}\cdot\boldsymbol{\sigma} & 0 \\ 0 & 0 & 0 & -v\mathbf{k}\cdot\boldsymbol{\sigma} \end{pmatrix} \tag{4.28}$$

where $h_0 = \lim_{\mathbf{k}\to 0} h_0^+(\mathbf{k})$ and $h_i = -v\mathbf{q}_i \cdot \boldsymbol{\sigma}$ for $i = 1, 2, 3$. Our goal is to find the zero modes of $\mathcal{H}^{(0)}$ and derive around them an approximate perturbative Hamiltonian. Let $\Psi_0 = (\psi_0, \psi_1, \psi_2, \psi_3)^T$ is the spinor corresponding to the zero modes of $\mathcal{H}^{(0)}$. Being a zero mode implies the following constraints on the components,

$$h_0\psi_0 + \sum_{i=1,2,3} T(\mathbf{q}_i)\psi_i = 0 \tag{4.29}$$

$$\psi_i = -h_i^{-1} T^\dagger(\mathbf{q}_i)\psi_0 \text{ for } i = 1, 2, 3. \tag{4.30}$$

After a series of algebraic manipulations, one can show that $\sum_i T(\mathbf{q}_i) h_i^{-1} T^\dagger(\mathbf{q}_i) = 0$. So the first constraint (4.29) simplifies to $h_0\psi_0 = 0$ which further implies there are two zero modes (denote them by Ψ_0^1 and Ψ_0^2) of the 8 band model that are completely determined by the two zero modes $\psi_0 = |1\rangle, |2\rangle$ of the isolated monolayer graphene Hamiltonian h_0. The two zero modes $|1\rangle$ and $|2\rangle$ are orthonormal $\langle i|j\rangle = \delta_{ij}$ and span a two dimensional subspace. Knowing ψ_0, one can determine the rest of the components of Ψ_0 through the relation (4.30) but we need first to normalize the spinors of the two zero modes Ψ_0^i. We have

$$|\Psi_0^i|^2 = \langle i| (I + \sum_{j=1,2,3} T(\mathbf{q}_j)(h_j^-)^\dagger h_j^{-1} T^\dagger(\mathbf{q}_j)) |i\rangle \tag{4.31}$$

with I is the identity matrix. We notice that

$$\begin{aligned} h_j^{-1} &= -\frac{h_j}{v^2|\mathbf{q}_j|^2} \\ h_j^2 &= v^2|\mathbf{q}_j|^2. \\ \sum_{j=1,2,3} T(\mathbf{q}_j)T^\dagger(\mathbf{q}_j) &= 3(w_0^2 + w_1^2)I \end{aligned} \tag{4.32}$$

Substituting this above, we get

$$|\Psi_0^1|^2 = |\Psi_0^2|^2 \equiv |\Psi_0|^2 = 1 + 3\frac{w_0^2 + w_1^2}{v^2|\mathbf{q}_1|^2} \equiv 1 + 6\tilde{\alpha}^2 \tag{4.33}$$

where we defined $\tilde{\alpha} = \frac{\sqrt{w_0^2+w_1^2}}{\sqrt{2}v|\mathbf{q}|}$ and used that $|\mathbf{q}_1|^2 = |\mathbf{q}_2|^2 = |\mathbf{q}_3|^2$. Now, to first order in $\mathbf{k}$, the effective Hamiltonian matrix elements $\mathcal{H}_{ij}$ in the zero mode bases,

$\mathcal{H}_{ij} = \langle \Psi_0^i | \mathcal{H}^{(1)} | \Psi_0^j \rangle / |\Psi_0|^2$, are given by

$$\mathcal{H}_{ij} = \frac{-v}{1+6\tilde{\alpha}^2} \langle i | \left(\mathbf{k}\cdot\boldsymbol{\sigma} + \sum_{n=1,2,3} T(\mathbf{q}_n)(h_n^{-1})^\dagger \mathbf{k}\cdot\boldsymbol{\sigma} h_n^{-1} T^\dagger(\mathbf{q}_n) \right| j \rangle . \tag{4.34}$$

To evaluate the above expression, we notice that $\mathbf{k}\cdot\boldsymbol{\sigma} h_n^{-1} = -h_n^{-1}\mathbf{k}\cdot\boldsymbol{\sigma} + \{\mathbf{k}\cdot\boldsymbol{\sigma}, h_n^{-1}\} = -h_n^{-1}\mathbf{k}\cdot\boldsymbol{\sigma} + \frac{-4}{v|\mathbf{q}|^2}\mathbf{q}_n \cdot \mathbf{k}\, I$. Explicit evaluation of the summation gives us $\sum_{n=1,2,3} T(\mathbf{q}_n)(h_n^{-})^\dagger h_n^{-1}\mathbf{k}\cdot\boldsymbol{\sigma} T^\dagger(\mathbf{q}_n) = 3\frac{w_0^2}{v^2|\mathbf{q}|^2}\mathbf{k}\cdot\boldsymbol{\sigma}$ and $\sum_{n=1,2,3} T(\mathbf{q}_n)(h_n^{-})^\dagger \mathbf{q}_n \cdot \mathbf{k} T^\dagger(\mathbf{q}_n) = \frac{3(w_0^2-w_1^2)}{4v}\mathbf{k}\cdot\boldsymbol{\sigma}$ where we made use also of the identities (4.32). Putting everything together and defining $\alpha = \frac{w_1}{v|\mathbf{q}_1|}$, we get

$$\mathcal{H}_{ij} = -v\frac{1-3\alpha^2}{1+6\tilde{\alpha}^2} \langle i | \mathbf{k}\cdot\boldsymbol{\sigma} | j \rangle . \tag{4.35}$$

We see that up to first order, the effective Hamiltonian around the moiré Dirac point (4.35) has the same form as the low energy Dirac Hamiltonian of monolayer graphene except that moiré Dirac velocity v^* is renormalized through [1]

$$v^* = v\frac{1-3\alpha^2}{1+6\tilde{\alpha}^2}. \tag{4.36}$$

Furthermore, we have that $|\mathbf{q}_1| = 2K_D \sin(\theta/2)$ where K_D is the length of one corner of the monolayer graphene Brillouin zone, i.e $K_D = |\mathbf{K}_+| = |\mathbf{K}_-|$. The velocity (4.36) vanishes in the limit $\alpha = \frac{w_1}{2vK_D\sin(\theta/2)} \rightarrow 1/\sqrt{3}$ which corresponds to twist angle $\theta = 1.09°$ or the first magic angle in our case.

4.3.3 Symmetries of the Continuum Model

After presenting the band structure of the continuum model, we now turn to discuss its symmetries. We start by focusing on the whole system with the two valleys. We first investigate the point group symmetries of real space twisted hexagons (Figure 4.4(b)) where we take our twist origin to be at the hexagon center.. In general, the crystallographic symmetries depend on any initial displacement between the two layers before twisting. However it can be shown [9] that the continuum model is insensitive to any relative displacement between the two layers as those can be gauged away so one can safely take the twist origin to at the center of the hexagon.

Immediately, one sees that there is a C_6 rotational symmetry. In addition, there is a mirror symmetry that consists of a two-fold inversion. The first one is around a plane perpendicular to the twisted hexagons plane such that $(x, y) \to (x, -y)$ and the second one is around a plane parallel to the twisted hexagons plane where the top and bottom layers are swapped. Effectively, it acts as a mirror M_y when restricted to two dimensions. On top of the point group symmetries, there is a lattice translation symmetry by the moiré lattice vectors t_{a_M} and a time reversal symmetry $\mathcal{T}$. Explicitly, these symmetries act on the Dirac spinors $\Psi_{l,\pm}(\mathbf{k})$ in the following way

---

[1] In the limit $w_0 = w_1$ and $\tilde{\alpha} = \alpha$, the formula reduces to the one derived in the original paper [9].

- Moiré translation symmetry :

$$t_{\mathbf{r}} \Psi_{l,\pm}(\mathbf{k}) t_{\mathbf{r}}^{-1} = e^{i\mathbf{k}\cdot\mathbf{r}} \Psi_{l,\pm}(\mathbf{k}) \tag{4.37}$$

  where $\mathbf{r} = m\mathbf{a}_1^M + n\mathbf{a}_2^M$ with $m, n \in Z$ and $\mathbf{a}_1^M$, $\mathbf{a}_2^M$ are the two bases for the moiré superlattice.

- C_6 rotational symmetry :

$$C_6 \Psi_{l,\pm}(\mathbf{k}) C_6^{-1} = \sigma_x e^{\mp i(2\pi/3)\sigma_z} \Psi_{l,\mp}(C_6\mathbf{k}) \tag{4.38}$$

- Mirror symmetry :

$$M_y \Psi_{l,\pm}(\mathbf{k}) M_y^{-1} = \sigma_x \Psi_{M_y[l],\pm}(M_y\mathbf{k}) \tag{4.39}$$

  with $M_y\mathbf{k} = M_y(k_x, k_y) = (k_x, -k_y)$ and $M_y[l]$ swaps the layer index, $M_y[t] = b$ and vise versa.

- Time reversal symmetry $\mathcal{T}$:

$$\mathcal{T} \Psi_{l,\pm}(\mathbf{k}) \mathcal{T}^{-1} = \Psi_{l,\mp}(-\mathbf{k}). \tag{4.40}$$

One can readily check that the above transformations keep the total Hamiltonian $H_{\text{TBG}} = H_{\text{TBG}}^+ + H_{\text{TBG}}^-$ invariant.

The Single-Valley Problem

The moiré Brillouin Zone is much smaller than the original Brillouin zone at small twist angles (Figure 4.4(c)). This allows us to treat both valleys separately as the momentum difference between the two valleys is much greater than the size of the moiré Brillouin zone therefore we will focus on the single-valley problem. We notice that the moiré translation symmetry $t_{\mathbf{r}}$ and the mirror symmetry M_y preserves the valley index while both C_6 and $\mathcal{T}$ flips it. However, the product $C_6\mathcal{T}$ still preserves the valley index. So the point group symmetries of the single valley are now generated by $C_6\mathcal{T}$ and the mirror M_y. We also notice that $(C_6\mathcal{T})^2 = C_3$ and $(C_6\mathcal{T})^3 = C_2\mathcal{T}$. Explicitly, the action of those single-valley preserving symmetries is obtained using the actions of the C_6 (4.38) and $\mathcal{T}$ (4.40) symmetry operators of the two-valley problem. We then have,

$$C_6\mathcal{T}\Psi_{l,\pm}(\mathbf{k})(C_6\mathcal{T})^{-1} = \sigma_x e^{\pm i(2\pi/3)\sigma_z}\Psi_{l,\pm}(-C_6\mathbf{k}) \tag{4.41}$$

$$C_3\Psi_{l,\pm}(\mathbf{k})C_3^{-1} = e^{\mp i(2\pi/3)\sigma_z}\Psi_{l,\pm}(C_3\mathbf{k}) \tag{4.42}$$

$$C_2\mathcal{T}\Psi_{l,\pm}(\mathbf{k})(C_2\mathcal{T})^{-1} = \sigma_x\Psi_{l,\pm}(\mathbf{k}). \tag{4.43}$$

The transformations generated by $C_6\mathcal{T}$ (equations (4.41),(4.42) and (4.43)) in addition to the moiré translation symmetry (4.37) and the mirror symmetry (4.39) will keep the single valley Hamiltonian $H^{\pm}_{\mathrm{TBG}}$ invariant.

The symmetry transformations have lots of implications on the single-valley spectrum of the continuum model. Apart from the moiré lattice translation symmetry that is crucial in order to define the moiré Brillouin zone, the C_3 symmetry (4.42) allows us to label the energy bands at the C_3 invariant momenta, $\mathbf{K}^t_+$ and $\mathbf{K}^b_+$ by their C_3 eigenvalues $e^{i\,2n\pi/3}$ with $n = 0, 1, 2$.

Moreover, the $C_2\mathcal{T}$ symmetry (4.43) takes a C_3 eigenstate to another C_3 eigenstate at the same point. To see this, let $|\mathbf{K}^t_+\rangle$ be a Bloch state at momentum $\mathbf{K}^t_+$ and let $e^{i\phi}$ be its eigenvalue under C_3 such that $C_3\,|\mathbf{K}^t_+\rangle = e^{i\phi}\,|\mathbf{K}^t_+\rangle$. We want to evaluate $C_3C_2\mathcal{T}\,|\mathbf{K}^t_+\rangle$. We notice that C_3 and $C_2\mathcal{T}$ commute since they are both products of the same $C_6\mathcal{T}$ operator. We have then $C_3C_2\mathcal{T}\,|\mathbf{K}^t_+\rangle = C_2\mathcal{T}C_3\,|\mathbf{K}^t_+\rangle = C_2\mathcal{T}e^{i\phi}\,|\mathbf{K}^t_+\rangle = e^{-i\phi}C_2\mathcal{T}\,|\mathbf{K}^t_+\rangle$ where the last step is obtained by noticing that the representation of $C_2\mathcal{T}$ when acting on single particle states is given by $C_2\mathcal{T} = \sigma_x\mathcal{K}$ where $\mathcal{K}$ denotes complex conjugation.

So if we have a state at the point $\mathbf{K}^t_+$ with C_3 eigenvalue $w = e^{i\phi} \neq 1$, there has to exist another state at the same point with the same energy and C_3 eigenvalue w^*. Indeed the valence and conduction bands that always cross at this point (Figure 4.5) correspond exactly to this case. These two bands form a two dimensional representation of the combined C_3 and $C_2\mathcal{T}$ symmetry group which has been also confirmed in numerics [112]. These band crossings are therefore locally stable as long as the $C_2\mathcal{T}$ symmetry is preserved.

Finally, it is sufficient to focus only on one moiré Dirac point as we are guaranteed to have exactly the same physics at the other point by the mirror symmetry M_y (4.39) that maps the two moiré Dirac points to each other. Such a symmetry ensures that the bands at the two points have the same energy.

4.4 Graphene-Based Models Without C_2 Symmetry

We have argued that the $C_2\mathcal{T}$ symmetry in the single-valley problem of twisted bilayer graphene protects the crossings of the valence and conduction bands at the $\mathbf{K}^t_+$ and $\mathbf{K}^b_+$ points. However, this combined symmetry is not always present in graphene moiré materials. The C_2 symmetry depends on the atomic configuration of the monolayers that form the moiré superlattice. We discuss next some moiré materials that do not possess this symmetry.

4.4.1 Graphene Aligned With Boron Nitride

Two dimensional hexagonal boron nitride (hBN) has the same honeycomb lattice structure as graphene, however, the two sublattices correspond to two different atoms (boron and nitrogen) so it is not C_2 invariant. In addition, the lattice constant of hBN is about 1.7 % greater than graphene's therefore when graphene is aligned with hBN, this tiny lattice mismatch results in a moiré pattern in the combined heterostructure.

hBN is a strong electrical insulator so at low energies, it is possible to integrate out its degrees of freedom restricting the dynamics only to graphene resulting in an effective superlattice potential $V_{\text{hBN}}(\mathbf{r})$ that the electrons in the graphene layer aligned with hBN experience [113]. The potential $V_{\text{hBN}}(\mathbf{r})$ is periodic $V_{\text{hBN}}(\mathbf{r}+\mathbf{R}_n) = V_{\text{hBN}}(\mathbf{r})$ with $\{\mathbf{R}_n\}$ the lattice vectors of the hBN-graphene superlattice. The periodic potential $V_{\text{hBN}}(\mathbf{r})$ admits a Fourier expansion $V_{\text{hBN}}(\mathbf{r}) = \sum_{\mathbf{G}_i} V_{\text{hBN}}(\mathbf{G}_i)e^{i\mathbf{G}_i\cdot\mathbf{r}}$ in terms of the reciprocal lattice vectors of the hBN-graphene superlattice.

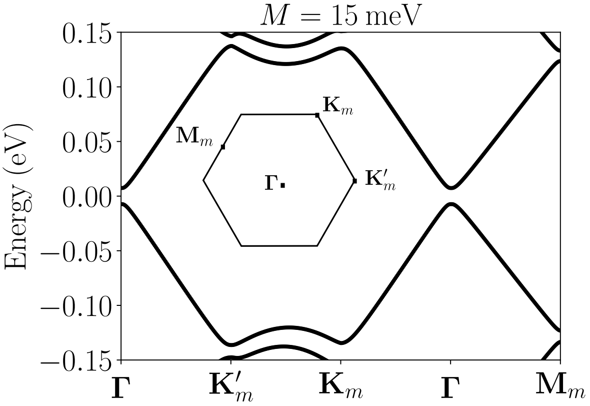

Figure 4.6: Band structure of graphene aligned with boron nitride along a cut in the moiré Brillouin zone shown in the inset.

The role of the superlattice potential is to fold the graphene hexagonal Brillouin zone into a smaller one, i.e. the moiré Brillouin zone which has the same orientation. The folding is done by identifying momentum $\mathbf{k}$ and $\mathbf{k}+\mathbf{G}_i$. In addition to the superlattice potential, the alignment with hBN will introduce a staggered sublattice potential in the graphene layers. This leads to the following Hamiltonian around one valley,

$$H^{+}_{\mathrm{G/hBN}} = \sum_{\mathbf{k}} \Psi^{\dagger}_{+}(\mathbf{k})(-v\mathbf{k}\cdot\boldsymbol{\sigma} + M\sigma_z)\Psi_{+}(\mathbf{k}) + \sum_{\mathbf{G}_i}\sum_{\mathbf{k}} \Psi^{\dagger}_{+}(\mathbf{k}+\mathbf{G}_i)V_{\mathrm{hBN}}(\mathbf{G}_i)\Psi_{+}(\mathbf{k}) \tag{4.44}$$

where $\Psi_{+}(\mathbf{K}) = (\Psi_{+,A}(\mathbf{k}), \Psi_{+,B}(\mathbf{k}))^T$ is the usual two component graphene spinor and M is a mass term induced by the alignment of hBN. The second term represents the moiré superlattice potential. The moiré potential components $\{V_{\mathrm{hBN}}(\mathbf{G}_i)\}$ can be obtained from ab-initio calculations [113].

A very accurate description is obtained by keeping only six moiré reciprocal vectors $\mathbf{G}_{\mathrm{i}=1,\dots,6} = R_{(i-1)\pi/3}\mathbf{G}_1$ with $\mathbf{G}_1 = (0, 4\pi/\sqrt{3}a_M)$ with a_M the lattice constant of the moiré superlattice. R_θ is a counter-clockwise rotation with an angle θ. Furthermore, the potential can be expanded as $V_{\mathrm{hBN}}(\mathbf{G}_i) = V_0(\mathbf{G}_i) + V_z(\mathbf{G}_i)\sigma_z + \mathrm{Re}(V_{AB}(\mathbf{G}_i))\sigma_x + \mathrm{Im}(V_{AB}(\mathbf{G}_i))\sigma_y$

For completeness, we list here the moiré potential components,

$$\begin{aligned} V_a(\mathbf{G}_1) = V_a(\mathbf{G}_3) = V_a(\mathbf{G}_5) = C_a e^{i\phi_a} \\ V_a(\mathbf{G}_2) = V_a(\mathbf{G}_4) = V_a(\mathbf{G}_6) = C_a e^{-i\phi_a} \end{aligned} \tag{4.45}$$

for $a = 0, z$, $C_0 = -10.13\mathrm{meV}$, $\phi_0 = 86.53°$, $C_z = -9.01\mathrm{meV}$ and $\phi_z = 8.43°$. The remaining components are given by

$$\begin{aligned} V_{AB}(\mathbf{G}_1) = V_{AB}(\mathbf{G}_4)^* = C_{AB}e^{i(\frac{2\pi}{3}-\phi_{AB})} \\ V_{AB}(\mathbf{G}_3) = V_{AB}(\mathbf{G}_2)^* = C_{AB}e^{-i(\phi_{AB})} \\ V_{AB}(\mathbf{G}_5) = V_{AB}(\mathbf{G}_6)^* = C_{AB}e^{i(-\frac{2\pi}{3}-\phi_{AB})} \end{aligned} \tag{4.46}$$

with $C_{AB} = 11.34\mathrm{meV}$ and $\phi_{AB} = 19.60°$. In Figure 4.6, we show the band structure around the charge neutrality. The sublattice potential opens a gap at the Dirac points as it breaks the C_2 symmetry of graphene.

4.4.2 Twisted Bilayer Graphene Aligned With Boron Nitride

In a conventional Van der Waals heterostructure, twisted bilayer graphene is often accompanied with hexagonal boron nitride (hBN) that acts as a substrate. Aligning boron nitride with one of the graphene layers affect the underlying physics as this breaks the C_2 symmetry of twisted bilayer graphene, hence the single valley problem is no longer $C_2\mathcal{T}$ symmetric which means that the valence and conduction bands crossings can be gapped out as they are no longer protected by any symmetry.

As discussed in the previous section, the effect of aligning boron nitride with a graphene layer is two-fold. The alignment induces a staggered sublattice potential

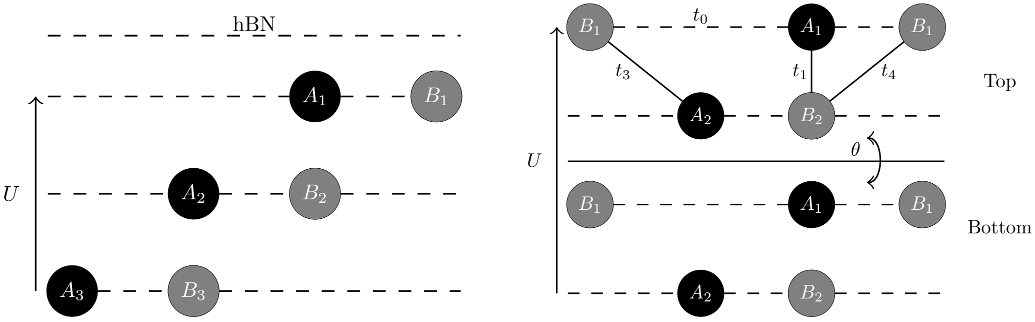

(a) **(b)**

Figure 4.7: (a) A schematic of ABC stacked trilayer graphene aligned with Boron Nitride with an applied gate potential U. (b) A schematic of twisted double bilayer graphene made of two layers of AB stacked bilayer graphene.

within the graphene layer in the vicinity of hBN and it generates an additional moiré pattern because of the lattice constant mismatch.

The hBN-graphene superlattice is not commensurate with the twisted bilayer graphene superlattice so it is not possible to construct a unified unit cell. However, ab-initio calculations [113] estimates $V_{\text{hBN}} \sim 10$meV. This is much smaller than TBG interlayer tunneling strength $w_0 \sim 110$meV and still smaller than the strength of the staggered potential M estimated to be $M \sim 15$meV so as an approximation, we neglect the hBN-graphene moiré pattern and the Hamiltonian becomes the original Hamiltonian of TBG in addition to a sublattice mass term in the top layer.

$$H^{+}_{\text{TBG/hBN}} \approx H^{+}_{\text{TBG}} + \sum_{\mathbf{k}} M\psi^{\dagger}_{t,+}(\mathbf{k})\sigma_z\psi_{t,+}(\mathbf{k}). \tag{4.47}$$

The band structure of the system around valley $\mathbf{K}_+$ is shown in Figure 4.8(a). There is a gap between the valence and conduction band as expected. Moreover, the two bands carry a non-zero Chern number, $C = 1$ and $C = -1$ respectively. The overall time reversal symmetry enforces opposite Chern numbers in the other valley. The flatness of the valence and conductions bands combined with the non trivial topology in terms of the non-zero Chern numbers render them as possible candidates for fractional Chern insulator (FCI) states which is the subject of Paper I [48].

4.4.3 Trilayer Graphene Aligned With Boron Nitride

Another moiré system that been shown to host flat bands with non-trivial correlated states is ABC stacked trilayer graphene aligned with boron nitride (TLG/hBN)

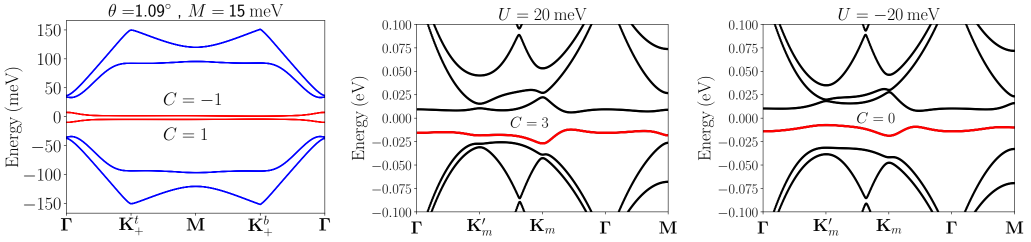

(a) **(b)** **(c)**

Figure 4.8: (a) Band structure of twisted bilayer graphene aligned with Boron Nitride. The alignment opens a gap between the valence and conduction bands rendering them topological. (b) and (c): Band structure of ABC stacked trilayer graphene aligned with Boron Nitride at positive and negative gate potential. The sign of the gate potentials controls the topology of the valence band shown in red. In generating these plots, we took into account remote hopping-term corrections as modeled in [20].

[20–25]. The setup of this system is shown schematically in Figure 4.7(a). A boron nitride layer is brought near the top layer of the trilayer graphene. In addition, a gate potential U is applied along the graphene layers. As discussed in section 4.2.2, the low energy degrees of freedom of trilayer graphene are mainly governed by electrons hopping in the top layer A and bottom layer B sublattices.

Focusing near one valley (valley $\mathbf{K}_+$ for example), the Hamiltonian of the system is given by

$$\begin{aligned} H_{\mathrm{TLG/hBN}} = \sum_k \Psi_+^\dagger(\mathbf{k}) \begin{pmatrix} 0 & \frac{v^3}{t_1^2}(-k_x - ik_y)^3 \\ \frac{v^3}{t_1^2}(-k_x + ik_y)^3 & 0 \end{pmatrix} \Psi_+(\mathbf{k}) \\ + \sum_k \Psi_+^\dagger(\mathbf{k}) U \sigma_z \Psi_+(\mathbf{k}) + \sum_{\mathbf{G}_i} \sum_{\mathbf{k}} \psi^\dagger_{A_1,+}(\mathbf{k}+\mathbf{G}_i)(V_0(\mathbf{G}_i) + V_z(\mathbf{G}_i))\psi_{A_1,+}(\mathbf{k}) \end{aligned} \tag{4.48}$$

where $\Psi_+ = (\psi_{A_1,+}, \psi_{B_3,+})^T$ describes the low energy degrees of freedom. U is a gate potential applied across the trilayer graphene. The third term describes the moiré potential $V_{\mathrm{hBN}}(\mathbf{r})$ generated in the graphene layer that is in proximity of boron nitride which we take to be the top layer. Since we are keeping only the A_1 sublattice in the top layer, only the diagonal components of the moiré potential (4.45) are taken into account.

In the band structure plotted in Figures 4.8(b,c), we notice the appearance of a narrow valence flat band around charge neutrality. It is topologically non-trivial with a Chern number $C = 3$ for a range of applied gate potentials. Upon switching

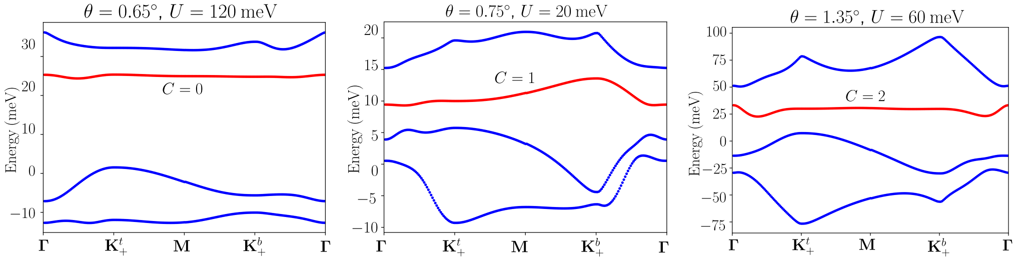

(a) **(b)** **(c)**

Figure 4.9: Band structure of twisted double bilayer graphene at a number of twists angles θ and gate potentials U. The first conduction band above charge neutrality is shown in red.

the sign of the potential, the band becomes topologically trivial with $C = 0$. We investigate the interaction physics in this band in Paper I [48] and Paper IV [51] , where we demonstrate the emergence of weakly interacting phases from a purely interacting problem.

4.4.4 Twisted Double Bilayer Graphene

A graphene-based moiré system that attracted recent interest due to the experimental realization of correlated phases is twisted double bilayer graphene [21, 27–35], made out of two bilayers of graphene with a relative twist as schematically shown in Figure 4.7(b). This configuration does not have C_2 symmetry by default. Also, unlike twisted bilayer graphene, the band gap and bandwidth can be controlled with an external electric field. In twisted bilayer graphene, an external electric field would result in breaking the mirror symmetry M_y. This would change the energy levels around the moiré Dirac points but cannot gap out the crossings [8, 114].

Moroever, the topology of the bands of twisted double bilayer graphene around charge neutrality can be controlled by tuning the twist angle and the strength of the applied electric field resulting in a rich phase diagram [31, 49].

We assume that the interlayer tunneling resulting from the relative twist is restricted to occur between the two middle layers, the bottom layer of the top bilayer and the top layer of the bottom bilayer. We can then use the continuum model we derived for twisted bilayer graphene in section 4.3.1 to also model the interlayer tunneling between the two twisted bilayers. Around valley $\mathbf{K}_+$, this gives us

$$H^+_{\text{TDBG}} = \sum_{\mathbf{k}} (\Psi^\dagger_{t,+}(\mathbf{k})\mathcal{H}^+_{\theta/2}(\mathbf{k})\Psi_{t,+}(\mathbf{k}) + \Psi^\dagger_{b,+}(\mathbf{k})\mathcal{H}^+_{-\theta/2}(\mathbf{k})\Psi_{b,+}(\mathbf{k})) + \sum_{\mathbf{k},i=1,2,3} \Psi^\dagger_{b,+}(\mathbf{k}+\mathbf{q}_i)\tilde{T}(\mathbf{q}_i)\Psi_{t,+}(\mathbf{k}) + \text{h.c} \quad (4.49)$$

where $\Psi^\dagger_{l,+}(\mathbf{k}) = (\psi^{\dagger A_1}_{l,+}(\mathbf{k}), \psi^{\dagger B_1}_{l,+}(\mathbf{k}), \psi^{\dagger A_2}_{l,+}(\mathbf{k}), \psi^{\dagger B_2}_{l,+}(\mathbf{k}))^T$, $\psi^{\dagger\alpha}_{l,+}(\mathbf{k})$ is an operator that creates an electron with momentum $\mathbf{k}$ around valley $\mathbf{K}_+$ in layer $l = t, b$ and sublattice $\alpha = A_1, B_1, A_2, B_2$. $\mathcal{H}^+_\theta(\mathbf{k}) = \mathcal{H}^+(R_\theta\mathbf{k})$ where $\mathcal{H}^+$ is the bilayer graphene Hamiltonian (4.7) around valley $\mathbf{K}_+$. The moiré tunnelling matrices $\tilde{T}(\mathbf{q}_i)$ are given by the following outer product between the layer and sublattice degrees of freedom so that it acts only between sublattices A_2, B_2 in the top layer and sublattices A_1 and B_1 in the bottom layer,

$$\tilde{T}(\mathbf{q}_i) = \begin{pmatrix} 0 & 1 \\ 0 & 0 \end{pmatrix}_{\text{layer}} \otimes T(\mathbf{q}_i), \quad (4.50)$$

where $T(\mathbf{q}_i)$ is given in (4.23). In addition, we add a gate potential U across the two bilayers.

In Figure 4.9, we show band structure at selected parameters corresponding to 3 different Chern numbers. We notice that the conduction band is relatively flat and also the topology of the band manifested in its Chern number can be tuned by changing the twist angle θ and the gate potential U to take values $C = 0, 1, 2$. We find (Paper II [49]) an abundance of gate-tunable fractional Chern insulator states in these flat bands.

4.5 Transition Metal Dichalcogenides

So far, we have been focusing on models where graphene is the basic building block. Transition metal dichalcogenides (TMDs) are another class of two dimensional materials that have long history in the last century dating before the discovery of graphene. TMDs as the name suggests are made of transition metal atoms. These are elements in groups (IV, V, VI, VII, IX or X) in the periodic table. That is in addition to chalcogens (S, Se or Te) atoms.

Technically, TMDs exist as bulk materials but very thin monolayers can be extracted the same way graphene is extracted from graphite. TMDs were known first as a platform for harbouring charge density waves [115]. In addition, TMDs are semiconductors which means they have significant band gaps. This is in a stark

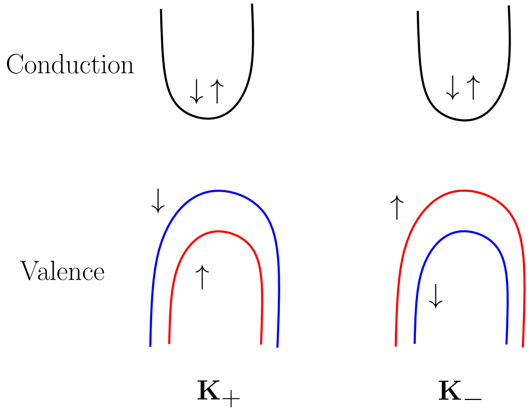

Figure 4.10: Schematic band structure for TMDs. Energy valleys exist around the corners of the Brillouin zone The strong spin-orbit coupling of the valence band near the corners of the Brillouin zone causes it to split in energy for up (red) and down (blue) spins.

contrast to pristine graphene that is semi-metallic. While graphene is promising for many applications, the lack of band gaps hinders its usage for electronics. The interest in TMDs has exploded after the first transistor was made from MoS_2. [116, 117].

A generic feature of the band structure of common TMDs is the existence of energy valleys around the corners of the Brillouin zone ($\mathbf{K}_+$ and $\mathbf{K}_-$ points) in addition to the $\mathbf{\Gamma}$ point. The exact energetics and which bands lie at which level is material dependent. Unlike graphene which has weak spin-orbit coupling, TMDs on the other hand show very strong spin-orbit coupling, specially for the valence bands that has spin splitting of the order $O(\mathrm{eV})$ from the strong spin-orbit coupling [118].

The origin of the spin-orbit coupling can be traced back to the lack of inversion symmetry in these materials [119]. The conduction band also has significant spin splitting but it is negligible compared to the valence band. Because of spinfull time-reversal symmetry that swaps the spins and the $\mathbf{K}_+$ and $\mathbf{K}_-$ points, the splitting is opposite around each valley. This leads to an effective *spin-valley locking* where the spin degree of freedom is tied to the valley. This is a peculiar feature of TMDs that are absent in graphene and offers a way to control magnetism by controlling the valley degree of freedom.

In Figure 4.10, we show a schematic of how the band structure of a given TMD can look like. In the vicinity of the valleys, effective Hamiltonians can be derived the same way it works for graphene layers. However this is a vast subject and we will not discuss this here.

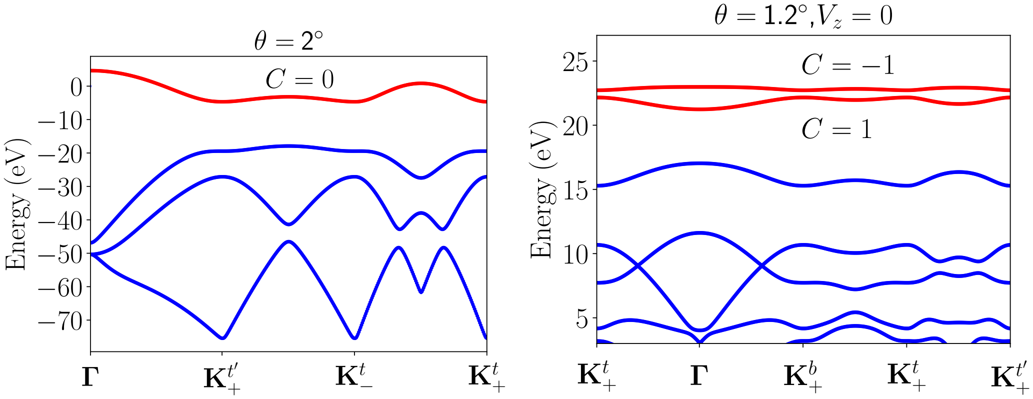

(a) **(b)**

Figure 4.11: (a) Band structure of $WSe_2/MoSe_2$ at twist angle $\theta = 2.0°$ around one valley. The top band is topologically trivial and can be used to simulate a Hubbard model. (b) Band structure of twisted $MoTe_2$ at twist angle $\theta = 1.2°$ and no applied electric field $V_z = 0$. The top-most pair of bands carry opposite Chern numbers $C = \pm 1$. There is another pair related by time-reversal symmetry at the other valley.

4.6 TMD Moiré Systems

In heterostructures made of TMDs, moiré patterns can arise in two different classes. TMD *heterobilayers* and TMD *homobilayers*. The heterobilayers are made of two different TMDs. In such a case, the moiré pattern comes from lattice constant mismatches similar to what discussed earlier for graphene aligned with boron nitride in addition to possible relative twists. For homobilayers, the moiré pattern only comes from twisting similar to twisted bilayer graphene. We will give here one example of each based on the proposals [120, 121]. In both examples, we consider only the valence band around the corners of the Brillouin zone where spin-orbit coupling is the strongest.

4.6.1 Heterobilayers

We start from two TMDs that have very similar lattice constants. For example, WSe_2 and $MoSe_2$. The valence band maxima of WSe_2 around the $\mathbf{K}_\pm$ points lie inside the band gap of $MoSe_2$ so the low energy physics comes mainly from the valence band of WSe_2. The moiré pattern can be then modelled as a superlattice potential acting on the states of the valence band of WSe_2. The moiré Hamiltonian around one valley is simply,

$$H^{+}_{\mathrm{WSe_2/MoSe_2}} = \sum_{\mathbf{k}} \Psi^{\dagger}_{+}(\mathbf{k}) \frac{(\mathbf{k}-\mathbf{K}^{\theta}_{+})^2}{2m^*} \Psi_{+}(\mathbf{k}) + \sum_{\mathbf{k},i=1,2,\ldots,6} \Psi^{\dagger}_{+}(\mathbf{k}+\mathbf{G}_i) V(\mathbf{G}_i) \Psi_{+}(\mathbf{k}) \tag{4.51}$$

where $\Psi^{\dagger}_{+}(\mathbf{k})$ is an operator that creates an electron in the rotated valley $\mathbf{K}^{\theta}_{+}$ with twist angle θ and spin $\uparrow$ because of the spin-valley locking. The valence band maxima is modelled as quadratic dispersion with an effective mass $m^* = 0.35m_e$. $\{V(\mathbf{G}_i)\}$ are the first six Fourier components of the moiré potential, $\mathbf{G}_i = R_{(i-1)\pi/3}\mathbf{G}_1$ with $\mathbf{G}_1 = (4\pi/\sqrt{3}a_M, 0)$ and a_M is the lattice constant of the moiré superlattice. $V(\mathbf{G}_1) = Ve^{i\psi}$ with $(V, \psi) = (6.6\,\mathrm{meV}, -94°)$ from ab-initio calculations. The C_3 symmetry of the model imposes $V(R_{2\pi/3}\mathbf{G}_i) = V(\mathbf{G}_i)$ and $V(\mathbf{G}_i) = V^*(-\mathbf{G}_i)$ which can be used to generate the other 5 components.

The band structure at twist angle $\theta = 2°$ is shown in Figure 4.11(a). The top band is flat and topologically trivial $C = 0$. A priori, this does not look interesting. However, it turns out that the real space structure of the Wannier orbitals constructed from the this band reveals that it is localized at a single moiré site in the unit cell that corresponds to the moiré potential maxima. (see Fig. 2(c) in Ref. [120]). This means that the top band could realize the classic Hubbard model. This is something that was not possible with graphene moiré systems such as twisted bilayer graphene due to the topological character of the bands that provides constraints against constructing localized lattice models [122–124]. Remarkably, the Hubbard model physics was indeed simulated in a TMD hetero-bilayer [38].

4.6.2 Homobilayers

Next, we discuss a model of TMD homobilayers. This is the model we use in Paper V [56] and was first presented in Ref. [121]. We consider twisted MoTe$_2$ focusing on the valence band maxima near the $\mathbf{K}_{\pm}$ points. Constructing a moiré Hamiltonian in this case follows a similar procedure as outlined earlier for twisted bilayer graphene. Because of the twist, we have a moiré Brillouin zone that has the same structure as shown in Figure 4.4(d). For one valley (equivalently one spin), we have

$$\begin{aligned} H^{+}_{\text{T-MoTe}_2} = &\sum_{\mathbf{k}} (\Psi^{\dagger}_{t,+}(\mathbf{k}) h^{+}_{\theta/2}(\mathbf{k}) \Psi_{t,+}(\mathbf{k}) + \Psi^{\dagger}_{b,+}(\mathbf{k}) h^{+}_{-\theta/2}(\mathbf{k}) \Psi_{b,+}(\mathbf{k})) \\ &+ \sum_{k} \Psi^{\dagger}_{+}(\mathbf{k}) V_z \sigma_z \Psi_{+}(\mathbf{k}) + \sum_{\mathbf{k},l_1,l_2,i=1,2,\ldots,6} \Psi^{\dagger}_{l_1,+}(\mathbf{k}+\mathbf{G}_i) T_{l_1 l_2}(\mathbf{G}_i) \Psi_{l_2,+}(\mathbf{k}) + \mathrm{h.c} \end{aligned} \tag{4.52}$$

where $\Psi^{\dagger}_{l,+}(\mathbf{k})$ is an operator that creates an electron with momentum $\mathbf{k}$ around valley $\mathbf{K}_+$ in layer $l = t, b$. $h^+_\theta(\mathbf{k})$ is the monolayer MoTe$_2$ low energy Hamiltonian around valley $\mathbf{K}_+$ rotated with angle θ. It is modelled as a free quadratic dispersion by $h^+_\theta(\mathbf{k}) = -\hbar^2(\mathbf{k} - \mathbf{K}^\theta_+)^2/2m^*$ with the effective mass $m^* = 0.51m_e$. V_z is an applied electric field between the top and bottom layers. The matrix $T_{l_1 l_2}(\mathbf{G}_i)$ describes the moiré potential with $\mathbf{G}_i = R_{(i-1)\pi/3}\mathbf{G}_1$ with $\mathbf{G}_1 = (4\pi/\sqrt{3}a_M, 0)$ and a_M is the lattice constant of the moiré superlattice. It's given by

$$T_{l_1 l_2}(\mathbf{G}_1) = \begin{pmatrix} Ve^{i\psi} & w \\ w & Ve^{-i\psi}. \end{pmatrix} \tag{4.53}$$

Also here the C_3 symmetry constrains $T_{l_1 l_2}(R_{2\pi/3}\mathbf{G}_i) = T_{l_1 l_2}(\mathbf{G}_i)$ and $T_{l_1 l_2}(\mathbf{G}_i) = T^*_{l_1 l_2}(-\mathbf{G}_i)$. For twisted MoTe$_2$, we have $(V, w, \psi) = (8\,\text{meV}, -8.5\,\text{meV}, -89.6°)$.

The diagonal terms of $T_{l_1 l_2}$ represent moiré potential in the same layer (top or bottom) while the off-diagonal terms represent interlayer hopping. In addition to the usual C_3 symmetry, the Hamiltonian (4.52) has a combined $C_{2y}\mathcal{T}$ when $V_z = 0$. This symmetry is a product of in-plane reflection C_{2y} that swaps the two layers and time-reversal symmetry $\mathcal{T}$ that swaps the valleys. It enforces a degeneracy at the moiré Brillouin zone corners $\mathbf{K}^t_+$ and $\mathbf{K}^b_+$.

In Figure 4.11(b), we show the band structure for $\theta = 1.2°$ in the absence of applied electric fields $V_z = 0$. We notice the emergence of a top-most pair of flat bands that carry Chern numbers $C = \pm 1$, separated by a gap to the rest of the spectrum.

The layer-projected wavefunctions of the topmost pair of bands are found [121] to be nearly localized on two atomic sites, R^M_X for the top layer and R^X_M for the bottom layer where R^α_β denotes atomic positions in the moiré unit cell where atom $\alpha = M, X$ of the top layer is locally aligned with atom $\beta = M, X$ in the bottom layer with M and X denoting metal and chalcogen atoms respectively. $M =$ Mo and $X =$ Te in our case. The atomic sites R^M_X and R^X_M form a honeycomb lattice which. Each site in this honeycomb lattice is accompanied with spin-valley degrees of freedom therefore the topmost pair of bands provides a realization of the Kane-Mele physics [125] at the non-interacting level.

However, in Paper V [56], we generally show that the non-interacting picture, manifested in possible Chern insulators at odd integer fillings of the flat bands, is quite fragile to interactions which give rise instead to layer-polarized states with ferroelectric order in addition to spin-valley ferromagnetism from strong interactions. The combined ferroelectricity and ferromagnetism is an example of multiferroicity [57].

Chapter 5

Discussion and Outlook

We have introduced in the previous chapters the theory of the quantum Hall effect, both integer and fractional and their lattice realizations, the Chern insulator. Then we moved on to discuss the tantalizing physics of moiré systems. A common theme between what is discussed so far is the existence of flat bands. The flat bands are the starting point for the microscopic analysis we carry out in the accompanying papers, of which we give below a brief summary of the main results.

5.1 Summary of Accompanying Papers

Paper I

In Paper I [48], we study two moiré systems. The first is ABC stacked trilayer graphene aligned with boron nitride discussed in section 4.4.3. As shown in Figure 4.8(b), the valence band is relatively flat and carries a Chern number $C = 3$. This led us to the initial conjecture that an FCI state is possible. However, we could not find signs of any FCI states upon fractionally filling this band.

Looking back at the problem of projected interactions in a single band, one notices that it is not particle-hole symmetric. Upon a particle hole transformation, there is an extra single-hole dispersion term that appears (see equations (3) and (4) in Paper I [48]). In the usual Landau level problem, such a term is constant so the problem within one Landau level is particle-hole symmetric and it suffices to study only filling fractions $\nu \leq 1/2$ [1].

On the other hand, the single-hole dispersion is usually non-constant in generic lattice models. For example, we plot it for trilayer graphene aligned with boron nitride and twisted bilayer graphene in Fig. 1 in Paper I [48] and it is quite clear that it is dispersive. At high fillings of electrons, corresponding to low fillings of holes, the single-hole dispersion is expected to dominate over the hole-hole interactions resulting in gapless Fermi liquid states [127]. This is due to the low density of holes in this case so interactions between the holes are generally weak.

---

[1] While particle-hole symmetry is present in a single Landau level, it's generally broken by Landau level mixing which could be important, for instance, in determining the nature of the $\nu = 5/2$ fractional quantum Hall state [126].

Quite remarkably, we found that such a behavior continues down to very low fillings of electrons $\nu \sim 1/3$. When looking at the electron occupation in the ground state (see Fig. 2(a) and Fig. 2(b) in Paper I [48]), obtained by exactly diagonalizing the system, we find that it correlates with the single-hole dispersion at all fillings. Electrons tend to occupy states with the highest hole energy. Down to $\nu \sim 1/3$, there is a a well-defined Fermi surface, i.e. a clear jump in the occupation that starts to disappear at lower fillings marking a transition to possibly non-Fermi liquid behavior. We conclude that a key parameter has been identified, that is the single-hole dispersion. The strongly interacting problem turns out to be weakly interacting in terms of holes, up to very low electron filling fractions.

The second system investigated in the paper is twisted bilayer graphene aligned with boron nitride discussed in section 4.4.2. We focused on the valence band (similar results for the conduction band) with Chern number $C = 1$ as shown in Figure 4.8(a). We sought if FCI states are possible upon fractional doping of this band. To that end, we employed exact diagonalization and found evidence of a Laughlin-like FCI state at $\nu = 1/3$ as shown in Fig. 3 in Paper I [48]. The theory behind the numerical evidence that includes ground state degeneracies, spectral flow and particle entanglement spectrum are discussed in detail in section 3.2.

A possible reason why such a state is stabilized is the less fluctuating single-hole dispersion (see Fig.1 in Paper I [48]). A highly dispersive single-hole dispersion is very likely to destroy FCI phases. Looking also at the occupation at $\nu = 1/3$ reveals that it is more uniform as expected from a uniform density fractional quantum Hall state. A finite-size calculation shows that the gap above the ground state is of order 10 K which suggests that this state could definitely survive higher temperatures than usual quantum Hall systems. This provided a strong evidence that twisted bilayer graphene is a promising candidate for realizing high temperature FCI states down to zero magnetic field.

Our findings of FCIs in twisted bilayer graphene were subsequently corroborated by two related studies. In Ref. [128], the role of spin was taken into account and in Ref. [129], analytical arguments based on the chiral limit [130] have shown that FCI states might be favoured. This is due to the fact that the wavefunctions of twisted bilayer graphene in such limit can be obtained analytically and they turn out to be reminiscent of Landau level wavefunctions on the torus [131].

Our theoretical prediction was confirmed later in a recent local compressibility experiment [55] where evidence of a series of FCI states were found, albeit at non-zero magnetic field. The most prominent of these, the FCI states at fillings $3 + 1/3$ and $3 + 2/3$ (Fig. 1(b) in Ref. [55]) correspond to the case we studied in Paper I [48]. They survive down to magnetic field $B \sim 5$T. While this is still a considerable magnetic field, this represents a major improvement compared to the earlier realization of FCI states [54] that required a magnetic field $B \sim 30$T to create Landau levels in the graphene heterostructure. In our paper, we reported the existence of the FCI state at a slightly different value of the AA interlayer tunneling parameter w_0 (see equation (4.23)) which physically puts the system in a qualitatively similar regime as the actual experiment with a non-zero magnetic field.

The reason behind the destabilization of the FCI state below $B \sim 5$T is the existence of a competing charge density wave (CDW) that survives down to zero magnetic field. The competition between the FCI and CDW [132] is sensitive to the band geometry of the flat bands (section 3.3) that depends on the ratio of AA to AB interlayer tunnelling w_0/w_1 (equation (4.23)). FCIs are favoured towards lower values of $w_0/w_1 \leq 0.6$. It is believed that $w_0/w_1 \sim 0.7 - 0.8$ in twisted bilayer graphene which explains the existence of a CDW state and the need for a it of magnetic field to stabilize the FCI state instead. In Paper IV [51], we provide an alternative explanation of the competition from a momentum space occupation point of view.

Paper II

In Paper II [49], we study twisted double bilayer graphene introduced in section 4.4.4. As discussed before, the bandwidth and topology of the conduction band can be tuned by varying the twist angle and the applied gate potential. We focus on two regions where the conduction band has Chern numbers $C = 1$ and $C = 2$ respectively. In the $C = 1$ region, we find signatures of a Laughlin FCI state at $\nu = 1/3$, its particle-hole conjugate $\nu = 2/3$. In addition, we find that the spin-singlet Halperin (332) state (section 3.1.6) is more favourable than the Jain state (section 3.1.5) at $\nu = 2/5$.

In the $C = 2$ region, we identify a novel spin-polarized FCI phase at $\nu = 1/3$ that has not been reported before in higher Chern number lattice models. The three-fold ground state degeneracy and spectral flow suggest that the system carries a quantized Hall response. Moreover, preliminary entanglement spectrum calculations rule out charge density wave states. However, the counting of the particle entanglement spectrum (section 3.2.4) is different from the expected counting of a Laughlin state which is the natural fractional quantum hall state at this filling.

By the virtue of the logic introduced in [99], a $\nu = 1/3$ filling fraction in a $C = 2$

band corresponds to negative flux attachment when the system is viewed through composite fermion theory. A more recent explanation [133] suggests that this state is adiabatically connected to a Halperin (112) state into two decoupled $C = 1$ basis. Filling $\nu = 1/3$ in this case corresponds to filling 2/3 of each $C = 1$ band, hence the hypothesized Halperin (112) state. The particle entanglement spectrum counting we did (similar counting for a similar state was done in [134]) is in agreement with this hypothesis.

It's quite surprising that such a unique state can be theoretically predicted in an already-manufactured material such as twisted double bilayer graphene beyond toy models. All these results establish twisted double bilayer graphene as another promising candidate for the experimental realization of multi-component and higher Chern number FCI states.

Paper III

In Paper III [50], we take a detour from moiré systems and study the possibility of having generic lattice models with constant Berry curvature. This is motivated by research on optimal lattice models for realizing fractional Chern insulators where Berry curvature uniformity is usually considered as a good indicator. We construct a general algorithm to flatten the Berry curvature for generic lattice models with three or more bands. In addition, we prove that there is a lower bound to Berry curvature fluctuations in two band models implying it is impossible to flatten the Berry curvature in this case.

Having established the possibility of constant Berry curvature, we turn to study the implications of this on the properties of FCIs. For this, we study bosonic FCIs in the flat bands of two lattice models, the Kapit-Mueller (KM) model [135] and the Hofstadter model [136], with on-site interactions. Similar to the fermionic case (section 3.1.2), bosonic Laughlin states are exact zero modes for a Haldane pseudopotential Hamiltonian with only non-zero V_0 component or equivalently only on-site interactions. This case can be realized exactly with interacting lattice Hamiltonians of bosons.

We find that flattening the curvature does not always improve the properties of FCIs, namely the energy gap and the degeneracy splitting of the many-body ground states. The KM model realizes a discretized version of the lowest Landau level so it has exact zero energy modes at half filling $\nu = 1/2$ for on-site interactions. We find that the ground state exact degeneracy is split and they are no-longer zero modes when the curvature is made constant resulting in a less ideal model for FCI in this sense. Finally, we prove that the GMP algebra discussed in section 3.3.1 cannot be realized in any strictly tight-binding model on a lattice.

Paper IV

In Paper IV [51], we carefully investigate the particle-hole asymmetry of band-projected interactions highlighted in Paper I [48]. We relate the interaction-induced hole dispersion to the Fubini-Study metric (section 2.3) of the flat band. This is always true in the limit of small momentum exchange but we argue that this limit is natural in many moiré systems since the form factors decay quickly. The existence of many bands in these models allows the Bloch eigenfunctions to spread out in the complex projective space leading to a fast decay of the form factors.

Having related the interaction-induced hole dispersion to the Fubini-Study metric, we study how the electron occupation in the many-body ground state correlates with the Fubini-Study metric and we find that electrons tend to occupy states with lower values of the Fubini-Study metric trace. This allows us to explain the origin of the observed (Paper I [48]) emergent Fermi liquids in ABC stacked trilayer graphene aligned with boron nitride and to give an alternative explanation of the FCI vs CDW competition in twisted bilayer graphene aligned with boron nitride.

Our findings provide new insights about the significance of the Fubini-Study metric, a single-body quantity, when it comes to the many-body physics of a large class of materials. The Fubini-Study metric has been less explored in condensed matter systems compared to the Berry curvature. But as evident from our results, it appears very naturally in band-projected interactions with fast-decaying form factors.

Paper V

In Paper V [56], we study another class of moiré systems where the basic building block is TMDs (section 4.6) instead of graphene. We focus on twisted TMD homobilayers (section 4.6.2) at odd integer fillings and study the competing phases as a function of the interaction range and strength.

Our main finding is the abundance of multiferroicity [57] through the phase diagram (Fig. 1 in Paper V [56]). The multiferroicity consists of co-existing magnetic and electric orders. The magnetic order corresponds to spin-valley ferromagnetism and the electric order corresponds to layer polarization where there is an unbalanced number of charge carriers in the two twisted layers.

Upon decreasing the interaction range, we observe a transition from the multiferroic to a Chern insulator phase (section 2.4) obtained by filling one of the flat Chern bands. We find that the structure of the phase diagram can be intuitively understood from a simple real space picture consisting of a honeycomb lattice with two sublattices representing the two layers.

Multiferroics hold a great promise for future technological applications due to the tantalizing idea of controlling magnetism with electric fields through a possible magneto-electric coupling in these materials which could give rise to far more energy-efficient electronic devices that do not rely on running electric currents to generate magnetic fields thereby avoiding heating problems. Multiferroics are rare [137] therefore their possible existence in a moiré heterostructure could guide the search towards experimental setups where this phenomenon is more prevalent.

5.2 Outlook

Having established the existence of wide range of distinct quantum phases in moiré systems including fractional Chern insulators, Fermi liquids and multiferroics, a number of future directions are worth looking at.

In connection to the predicted and observed *abelian* FCIs in moiré systems, it is of ultimate interest to research into the possibility of stabilizing *non-abelian* FCIs in these systems. The existence of many tuning knobs in Van der Waals moiré heterostructures offers a playground for designing different flat band systems with controllable topology. We have seen already that the flat bands of these systems are very promising for abelian FCIs such as the Laughlin state but so far, no numerical evidence of non-abelian states could be found. It is therefore necessary to understand the reason behind the absence of these states. A possible explanation is most likely due to the nature of the projected Coulomb interactions onto these flat bands which could be similar to projected Coulomb interaction onto the lowest Landau level that admits a highly-peaked psuedopotential expansion as discussed in section 3.1.2.

Non-abelian fractional quantum Hall states are observed in the first excited Landau level ($n = 1$ in equation (2.8)) which admits in contrast a less peaked psuedopotential expansion [138]. It is therefore interesting to understand this interplay and how to realize this physics in moiré systems. Another route towards non-abelian states could possibly be by utilizing the multi-component nature of the moiré flat bands. Interaction could drive the existence of tunneling-driven non-abelian phases [139, 140] or even exotic non-abelian defects from the higher Chern nature of the flat bands [141, 142].

Moiré systems have been shown to be a platform for the intricate interplay between the quantum geometry of the flat bands and strongly correlated phases. This is evident, for instance, in the context of FCIs and is also relevant to the superconductivity observed in these systems [143]. A future interesting direction is to investigate in more detail the effects of the quantum geometry distribution in favoring or ruling out possible quantum phases of matter. We have seen already in Paper IV [51] an example of geometry-induced Fermi liquids in trilayer graphene aligned with boron nitride that are favoured over other phases in a purely interacting problem.

It would be interesting to develop a general framework for addressing this interplay. For example, in the context discussed in Paper IV [51], the emergent weakly interacting nature of the problem allows the possible use of standard techniques from perturbation theory that could address possible charge or spin order instabilities in addition to the expected non-Fermi liquid behaviour at the onset of these instabilities.

Finally, apart from general aspects of correlation physics in TMDs moiré systems that are worth investigating, we note that the predicted multiferroicity in twisted TMDs (Paper V [56]) opens avenues for numerous future directions. A very natural follow-up in this regard is to investigate possible ways of achieving the long-sought-after electric field control of magnetism. This requires studying the magneto-electric coupling in the multiferroic phase with the aim of identifying and proposing exact mechanisms under which the two orders are intertwined, not only co-existing.

Bibliography

[1] A. H. Castro Neto, F. Guinea, N. M. R. Peres, K. S. Novoselov, and A. K. Geim. The electronic properties of graphene. *Rev. Mod. Phys.*, 81(1):109–162, 2009.

[2] A. K. Geim and I. V. Grigorieva. Van der Waals heterostructures. *Nature*, 499(7459):419–425, 2013.

[3] K. v. Klitzing, G. Dorda, and M. Pepper. New Method for High-Accuracy Determination of the Fine-Structure Constant Based on Quantized Hall Resistance. *Phys. Rev. Lett.*, 45(6):494–497, 1980.

[4] D. C. Tsui, H. L. Stormer, and A. C. Gossard. Two-Dimensional Magnetotransport in the Extreme Quantum Limit. *Phys. Rev. Lett.*, 48(22):1559–1562, 1982.

[5] X. G. Wen. Topological orders in rigid states. *Int. J. Mod. Phys. B*, 04(02):239–271, 1990.

[6] X. G. Wen and Q. Niu. Ground-state degeneracy of the fractional quantum Hall states in the presence of a random potential and on high-genus Riemann surfaces. *Phys. Rev. B*, 41(13):9377–9396, 1990.

[7] Leon Balents, Cory R. Dean, Dmitri K. Efetov, and Andrea F. Young. Superconductivity and strong correlations in moiré flat bands. *Nat. Phys.*, 16(7):725–733, 2020.

[8] J. M. B. Lopes dos Santos, N. M. R. Peres, and A. H. Castro Neto. Graphene Bilayer with a Twist: Electronic Structure. *Phys. Rev. Lett.*, 99(25):256802, 2007.

[9] Rafi Bistritzer and Allan H. MacDonald. Moiré bands in twisted double-layer graphene. *PNAS*, 108(30):12233–12237, 2011.

[10] Yuan Cao, Valla Fatemi, Shiang Fang, Kenji Watanabe, Takashi Taniguchi, Efthimios Kaxiras, and Pablo Jarillo-Herrero. Unconventional superconductivity in magic-angle graphene superlattices. *Nature*, 556(7699):43–50, 2018.

[11] Yuan Cao, Valla Fatemi, Ahmet Demir, Shiang Fang, Spencer L. Tomarken, Jason Y. Luo, Javier D. Sanchez-Yamagishi, Kenji Watanabe, Takashi Taniguchi, Efthimios Kaxiras, Ray C. Ashoori, and Pablo Jarillo-Herrero. Correlated insulator behaviour at half-filling in magic-angle graphene superlattices. *Nature*, 556(7699):80–84, 2018.

[12] Yonglong Xie, Biao Lian, Berthold Jäck, Xiaomeng Liu, Cheng-Li Chiu, Kenji Watanabe, Takashi Taniguchi, B. Andrei Bernevig, and Ali Yazdani. Spectroscopic signatures of many-body correlations in magic-angle twisted bilayer graphene. *Nature*, 572(7767):101–105, 2019.

[13] Xiaobo Lu, Petr Stepanov, Wei Yang, Ming Xie, Mohammed Ali Aamir, Ipsita Das, Carles Urgell, Kenji Watanabe, Takashi Taniguchi, Guangyu Zhang, Adrian Bachtold, Allan H. MacDonald, and Dmitri K. Efetov. Superconductors, orbital magnets and correlated states in magic-angle bilayer graphene. *Nature*, 574(7780):653–657, 2019.

[14] Matthew Yankowitz, Shaowen Chen, Hryhoriy Polshyn, Yuxuan Zhang, K. Watanabe, T. Taniguchi, David Graf, Andrea F. Young, and Cory R. Dean. Tuning superconductivity in twisted bilayer graphene. *Science*, 363(6431):1059–1064, 2019.

[15] Yu Saito, Jingyuan Ge, Kenji Watanabe, Takashi Taniguchi, and Andrea F. Young. Independent superconductors and correlated insulators in twisted bilayer graphene. *Nat. Phys.*, 16(9), 2020.

[16] Petr Stepanov, Ipsita Das, Xiaobo Lu, Ali Fahimniya, Kenji Watanabe, Takashi Taniguchi, Frank H. L. Koppens, Johannes Lischner, Leonid Levitov, and Dmitri K. Efetov. Untying the insulating and superconducting orders in magic-angle graphene. *Nature*, 583(7816), 2020.

[17] Aaron L. Sharpe, Eli J. Fox, Arthur W. Barnard, Joe Finney, Kenji Watanabe, Takashi Taniguchi, M. A. Kastner, and David Goldhaber-Gordon. Emergent ferromagnetism near three-quarters filling in twisted bilayer graphene. *Science*, 365(6453):605–608, 2019.

[18] M. Serlin, C. L. Tschirhart, H. Polshyn, Y. Zhang, J. Zhu, K. Watanabe, T. Taniguchi, L. Balents, and A. F. Young. Intrinsic quantized anomalous Hall effect in a moiré heterostructure. *Science*, 367(6480):900–903, 2020.

[19] Kevin P. Nuckolls, Myungchul Oh, Dillon Wong, Biao Lian, Kenji Watanabe, Takashi Taniguchi, B. Andrei Bernevig, and Ali Yazdani. Strongly correlated Chern insulators in magic-angle twisted bilayer graphene. *Nature*, 588(7839):610–615, 2020.

[20] Bheema Lingam Chittari, Guorui Chen, Yuanbo Zhang, Feng Wang, and Jeil Jung. Gate-Tunable Topological Flat Bands in Trilayer Graphene Boron-Nitride Moiré Superlattices. *Phys. Rev. Lett.*, 122(1), 2019.

[21] Ya-Hui Zhang, Dan Mao, Yuan Cao, Pablo Jarillo-Herrero, and T. Senthil. Nearly flat Chern bands in moiré superlattices. *Phys. Rev. B*, 99(7):075127, 2019.

[22] Fan Zhang, Bhagawan Sahu, Hongki Min, and A. H. MacDonald. Band structure of abc-stacked graphene trilayers. *Phys. Rev. B*, 82(3):035409, 2010.

[23] Guorui Chen, Lili Jiang, Shuang Wu, Bosai Lyu, Hongyuan Li, Bheema Lingam Chittari, Kenji Watanabe, Takashi Taniguchi, Zhiwen Shi, Jeil Jung, Yuanbo Zhang, and Feng Wang. Evidence of a gate-tunable Mott insulator in a trilayer graphene moiré superlattice. *Nature Physics*, 15(3):237–241, 2019.

[24] Guorui Chen, Aaron L. Sharpe, Patrick Gallagher, Ilan T. Rosen, Eli J. Fox, Lili Jiang, Bosai Lyu, Hongyuan Li, Kenji Watanabe, Takashi Taniguchi, Jeil Jung, Zhiwen Shi, David Goldhaber-Gordon, Yuanbo Zhang, and Feng Wang. Signatures of tunable superconductivity in a trilayer graphene moiré superlattice. *Nature*, 572(7768):215–219, 2019.

[25] Guorui Chen, Aaron L. Sharpe, Eli J. Fox, Ya-Hui Zhang, Shaoxin Wang, Lili Jiang, Bosai Lyu, Hongyuan Li, Kenji Watanabe, Takashi Taniguchi, Zhiwen Shi, T. Senthil, David Goldhaber-Gordon, Yuanbo Zhang, and Feng Wang. Tunable correlated Chern insulator and ferromagnetism in a moiré superlattice. *Nature*, 579(7797):56–61, 2020.

[26] Guorui Chen, Aaron L. Sharpe, Eli J. Fox, Shaoxin Wang, Bosai Lyu, Lili Jiang, Hongyuan Li, Kenji Watanabe, Takashi Taniguchi, Michael F. Crommie, Marc A. Kastner, Zhiwen Shi, David Goldhaber-Gordon, Yuanbo Zhang, and Feng Wang. Tunable Orbital Ferromagnetism at Noninteger Filling of a Moiré Superlattice. *Nano Letters*, 22(1), 2022.

[27] Mikito Koshino. Band structure and topological properties of twisted double bilayer graphene. *Phys. Rev. B*, 99(23):235406, 2019.

[28] Narasimha Raju Chebrolu, Bheema Lingam Chittari, and Jeil Jung. Flat bands in twisted double bilayer graphene. *Phys. Rev. B*, 99(23):235417, 2019.

[29] Young Woo Choi and Hyoung Joon Choi. Intrinsic band gap and electrically tunable flat bands in twisted double bilayer graphene. *Phys. Rev. B*, 100(20):201402, 2019.

[30] Fatemeh Haddadi, QuanSheng Wu, Alex J. Kruchkov, and Oleg V. Yazyev. Moiré Flat Bands in Twisted Double Bilayer Graphene. *Nano Lett.*, 20(4):2410–2415, 2020.

[31] Jong Yeon Lee, Eslam Khalaf, Shang Liu, Xiaomeng Liu, Zeyu Hao, Philip Kim, and Ashvin Vishwanath. Theory of correlated insulating behaviour and spin-triplet superconductivity in twisted double bilayer graphene. *Nature Communications*, 10(1):5333, 2019.

[32] Cheng Shen, Yanbang Chu, QuanSheng Wu, Na Li, Shuopei Wang, Yanchong Zhao, Jian Tang, Jieying Liu, Jinpeng Tian, Kenji Watanabe, Takashi Taniguchi, Rong Yang, Zi Yang Meng, Dongxia Shi, Oleg V. Yazyev, and Guangyu Zhang. Correlated states in twisted double bilayer graphene. *Nature Physics*, 16(5):520–525, 2020.

[33] Yuan Cao, Daniel Rodan-Legrain, Oriol Rubies-Bigorda, Jeong Min Park, Kenji Watanabe, Takashi Taniguchi, and Pablo Jarillo-Herrero. Tunable correlated states and spin-polarized phases in twisted bilayer–bilayer graphene. *Nature*, 583(7815):215–220, 2020.

[34] Xiaomeng Liu, Zeyu Hao, Eslam Khalaf, Jong Yeon Lee, Yuval Ronen, Hyobin Yoo, Danial Haei Najafabadi, Kenji Watanabe, Takashi Taniguchi, Ashvin Vishwanath, and Philip Kim. Tunable spin-polarized correlated states in twisted double bilayer graphene. *Nature*, 583(7815):221–225, 2020.

[35] G. William Burg, Jihang Zhu, Takashi Taniguchi, Kenji Watanabe, Allan H. MacDonald, and Emanuel Tutuc. Correlated Insulating States in Twisted Double Bilayer Graphene. *Phys. Rev. Lett.*, 123(19):197702, 2019.

[36] Xiaodong Xu, Wang Yao, Di Xiao, and Tony F. Heinz. Spin and pseudospins in layered transition metal dichalcogenides. *Nature Phys*, 10(5):343–350, 2014.

[37] Sajedeh Manzeli, Dmitry Ovchinnikov, Diego Pasquier, Oleg V. Yazyev, and Andras Kis. 2D transition metal dichalcogenides. *Nat Rev Mater*, 2(8):1–15, 2017.

[38] Yanhao Tang, Lizhong Li, Tingxin Li, Yang Xu, Song Liu, Katayun Barmak, Kenji Watanabe, Takashi Taniguchi, Allan H. MacDonald, Jie Shan, and Kin Fai Mak. Simulation of Hubbard model physics in WSe2/WS2 moiré superlattices. *Nature*, 579(7799):353–358, 2020.

[39] Yang Xu, Kaifei Kang, Kenji Watanabe, Takashi Taniguchi, Kin Fai Mak, and Jie Shan. A tunable bilayer Hubbard model in twisted WSe2. *Nat. Nanotechnol.*, 17(9):934–939, 2022.

[40] Lei Wang, En-Min Shih, Augusto Ghiotto, Lede Xian, Daniel A. Rhodes, Cheng Tan, Martin Claassen, Dante M. Kennes, Yusong Bai, Bumho Kim, Kenji Watanabe, Takashi Taniguchi, Xiaoyang Zhu, James Hone, Angel Rubio, Abhay N. Pasupathy, and Cory R. Dean. Correlated electronic phases in twisted bilayer transition metal dichalcogenides. *Nat. Mater.*, 19(8):861–866, 2020.

[41] Yang Xu, Song Liu, Daniel A. Rhodes, Kenji Watanabe, Takashi Taniguchi, James Hone, Veit Elser, Kin Fai Mak, and Jie Shan. Correlated insulating states at fractional fillings of moiré superlattices. *Nature*, 587(7833):214–218, 2020.

[42] Xiong Huang, Tianmeng Wang, Shengnan Miao, Chong Wang, Zhipeng Li, Zhen Lian, Takashi Taniguchi, Kenji Watanabe, Satoshi Okamoto, Di Xiao, Su-Fei Shi, and Yong-Tao Cui. Correlated insulating states at fractional fillings of the WS2/WSe2 moiré lattice. *Nat. Phys.*, 17(6):715–719, 2021.

[43] Emma C. Regan, Danqing Wang, Chenhao Jin, M. Iqbal Bakti Utama, Beini Gao, Xin Wei, Sihan Zhao, Wenyu Zhao, Zuocheng Zhang, Kentaro Yumigeta, Mark Blei, Johan D. Carlström, Kenji Watanabe, Takashi Taniguchi, Sefaattin Tongay, Michael Crommie, Alex Zettl, and Feng Wang. Mott and generalized Wigner crystal states in WSe2/WS2 moiré superlattices. *Nature*, 579(7799):359–363, 2020.

[44] Tingxin Li, Shengwei Jiang, Lizhong Li, Yang Zhang, Kaifei Kang, Jiacheng Zhu, Kenji Watanabe, Takashi Taniguchi, Debanjan Chowdhury, Liang Fu, Jie Shan, and Kin Fai Mak. Continuous Mott transition in semiconductor moiré superlattices. *Nature*, 597(7876):350–354, 2021.

[45] Augusto Ghiotto, En-Min Shih, Giancarlo S. S. G. Pereira, Daniel A. Rhodes, Bumho Kim, Jiawei Zang, Andrew J. Millis, Kenji Watanabe, Takashi Taniguchi, James C. Hone, Lei Wang, Cory R. Dean, and Abhay N. Pasupathy. Quantum criticality in twisted transition metal dichalcogenides. *Nature*, 597(7876):345–349, 2021.

[46] Tingxin Li, Shengwei Jiang, Bowen Shen, Yang Zhang, Lizhong Li, Zui Tao, Trithep Devakul, Kenji Watanabe, Takashi Taniguchi, Liang Fu, Jie Shan, and Kin Fai Mak. Quantum anomalous Hall effect from intertwined moiré bands. *Nature*, 600(7890):641–646, 2021.

[47] Zui Tao, Bowen Shen, Shengwei Jiang, Tingxin Li, Lizhong Li, Liguo Ma, Wenjin Zhao, Jenny Hu, Kateryna Pistunova, Kenji Watanabe, Takashi Taniguchi, Tony F. Heinz, Kin Fai Mak, and Jie Shan. Valley-coherent quantum anomalous Hall state in AB-stacked MoTe2/WSe2 bilayers. *arXiv:2208.07452*, 2022.

[48] Ahmed Abouelkomsan, Zhao Liu, and Emil J. Bergholtz. Particle-Hole Duality, Emergent Fermi Liquids, and Fractional Chern Insulators in Moiré Flatbands. *Phys. Rev. Lett.*, 124(10):106803, 2020.

[49] Zhao Liu, Ahmed Abouelkomsan, and Emil J. Bergholtz. Gate-Tunable Fractional Chern Insulators in Twisted Double Bilayer Graphene. *Phys. Rev. Lett.*, 126(2):026801, 2021.

[50] Daniel Varjas, Ahmed Abouelkomsan, Kang Yang, and Emil Bergholtz. Topological lattice models with constant Berry curvature. *SciPost Physics*, 12(4), 2022.

[51] Ahmed Abouelkomsan, Kang Yang, and Emil J. Bergholtz. Quantum Metric Induced Phases in Moiré Materials. *arXiv:2202.10467*, 2022.

[52] Emil J. Bergholtz and Zhao Liu. Topological flat band models and fractional chern insulators. *Int. J. Mod. Phys. B*, 27(24):1330017, 2013.

[53] Siddharth A. Parameswaran, Rahul Roy, and Shivaji L. Sondhi. Fractional quantum Hall physics in topological flat bands. *Comptes Rendus Physique*, 14(9):816–839, 2013.

[54] Eric M. Spanton, Alexander A. Zibrov, Haoxin Zhou, Takashi Taniguchi, Kenji Watanabe, Michael P. Zaletel, and Andrea F. Young. Observation of fractional Chern insulators in a van der Waals heterostructure. *Science*, 360(6384):62–66, 2018.

[55] Yonglong Xie, Andrew T. Pierce, Jeong Min Park, Daniel E. Parker, Eslam Khalaf, Patrick Ledwith, Yuan Cao, Seung Hwan Lee, Shaowen Chen, Patrick R. Forrester, Kenji Watanabe, Takashi Taniguchi, Ashvin Vishwanath, Pablo Jarillo-Herrero, and Amir Yacoby. Fractional Chern insulators in magic-angle twisted bilayer graphene. *Nature*, 600(7889):439–443, 2021.

[56] Ahmed Abouelkomsan, Emil J. Bergholtz, and Shubhayu Chatterjee. Multiferroicity and Topology in Twisted Transition Metal Dichalcogenides. *arXiv.2210.14918*, 2022.

[57] W. Eerenstein, N. D. Mathur, and J. F. Scott. Multiferroic and magnetoelectric materials. *Nature*, 442(7104):759–765, 2006.

[58] E. H. Hall. On a New Action of the Magnet on Electric Currents. *American Journal of Mathematics*, 2(3):287–292, 1879.

[59] H. L. Stormer. Two-dimensional electron correlation in high magnetic fields. *Physica B: Condensed Matter*, 177(1):401–408, 1992.

[60] L. Landau. Diamagnetismus der Metalle. *Z. Physik*, 64(9):629–637, 1930.

[61] R. B. Laughlin. Quantized Hall conductivity in two dimensions. *Phys. Rev. B*, 23(10):5632–5633, 1981.

[62] N. Byers and C. N. Yang. Theoretical Considerations Concerning Quantized Magnetic Flux in Superconducting Cylinders. *Phys. Rev. Lett.*, 7(2):46–49, 1961.

[63] Mikio Nakahara. *Geometry, topology and physics*. CRC press, 2018.

[64] Michael Victor Berry. Quantal phase factors accompanying adiabatic changes. *Proceedings of the Royal Society of London. A. Mathematical and Physical Sciences*, 392(1802):45–57, 1984.

[65] Ming-Che Chang and Qian Niu. Berry Phase, Hyperorbits, and the Hofstadter Spectrum. *Phys. Rev. Lett.*, 75(7):1348–1351, 1995.

[66] Ming-Che Chang and Qian Niu. Berry phase, hyperorbits, and the Hofstadter spectrum: Semiclassical dynamics in magnetic Bloch bands. *Phys. Rev. B*, 53(11):7010–7023, 1996.

[67] Di Xiao, Ming-Che Chang, and Qian Niu. Berry phase effects on electronic properties. *Rev. Mod. Phys.*, 82(3):1959–2007, 2010.

[68] Shiing-shen Chern. Characteristic Classes of Hermitian Manifolds. *Annals of Mathematics*, 47(1):85–121, 1946.

[69] Sebastiano Peotta and Päivi Törmä. Superfluidity in topologically nontrivial flat bands. *Nat Commun*, 6(1):8944, 2015.

[70] Long Liang, Tuomas I. Vanhala, Sebastiano Peotta, Topi Siro, Ari Harju, and Päivi Törmä. Band geometry, Berry curvature, and superfluid weight. *Phys. Rev. B*, 95(2):024515, 2017.

[71] D. J. Thouless, M. Kohmoto, M. P. Nightingale, and M. den Nijs. Quantized Hall Conductance in a Two-Dimensional Periodic Potential. *Phys. Rev. Lett.*, 49(6):405–408, 1982.

[72] F. D. M. Haldane. Model for a Quantum Hall Effect without Landau Levels: Condensed-Matter Realization of the "Parity Anomaly". *Phys. Rev. Lett.*, 61(18):2015–2018, 1988.

[73] Chetan Nayak, Steven H. Simon, Ady Stern, Michael Freedman, and Sankar Das Sarma. Non-Abelian anyons and topological quantum computation. *Rev. Mod. Phys.*, 80(3):1083–1159, 2008.

[74] R. B. Laughlin. Anomalous Quantum Hall Effect: An Incompressible Quantum Fluid with Fractionally Charged Excitations. *Phys. Rev. Lett.*, 50(18):1395–1398, 1983.

[75] G. Fano, F. Ortolani, and E. Colombo. Configuration-interaction calculations on the fractional quantum Hall effect. *Phys. Rev. B*, 34(4):2670–2680, 1986.

[76] F. D. M. Haldane. Fractional Quantization of the Hall Effect: A Hierarchy of Incompressible Quantum Fluid States. *Phys. Rev. Lett.*, 51(7):605–608, 1983.

[77] J. M. Leinaas and J. Myrheim. On the theory of identical particles. *Nuovo Cim B*, 37(1):1–23, 1977.

[78] Frank Wilczek. Quantum Mechanics of Fractional-Spin Particles. *Phys. Rev. Lett.*, 49(14):957–959, 1982.

[79] Daniel Arovas, J. R. Schrieffer, and Frank Wilczek. Fractional Statistics and the Quantum Hall Effect. *Phys. Rev. Lett.*, 53(7):722–723, 1984.

[80] R. de Picciotto, M. Reznikov, M. Heiblum, V. Umansky, G. Bunin, and D. Mahalu. Direct observation of a fractional charge. *Nature*, 389(6647):162–164, 1997.

[81] J. Nakamura, S. Liang, G. C. Gardner, and M. J. Manfra. Direct observation of anyonic braiding statistics. *Nature Physics*, 16(9), 2020.

[82] F. D. M. Haldane. Many-Particle Translational Symmetries of Two-Dimensional Electrons at Rational Landau-Level Filling. *Phys. Rev. Lett.*, 55(20):2095–2098, 1985.

[83] B. I. Halperin. Statistics of Quasiparticles and the Hierarchy of Fractional Quantized Hall States. *Phys. Rev. Lett.*, 52(18):1583–1586, 1984.

[84] J. K. Jain. Composite-fermion approach for the fractional quantum Hall effect. *Physical Review Letters*, 63(2), 1989.

[85] David Tong. Lectures on the Quantum Hall Effect. *arXiv:1606.06687*, 2016.

[86] Jainendra K. Jain. *Composite Fermions.* Cambridge University Press, first edition, 2007.

[87] B. I. Halperin. Theory of the quantized Hall conductance. *Helv. Phys. Acta*, 56:75–102, 1983.

[88] T. S. Jackson, Gunnar Möller, and Rahul Roy. Geometric stability of topological lattice phases. *Nature Communications*, 6(1):8629, 2015.

[89] F. D. M. Haldane. "Fractional statistics" in arbitrary dimensions: A generalization of the Pauli principle. *Phys. Rev. Lett.*, 67(8):937–940, 1991.

[90] B. Andrei Bernevig and F. D. M. Haldane. Model Fractional Quantum Hall States and Jack Polynomials. *Phys. Rev. Lett.*, 100(24):246802, 2008.

[91] Xiao-Gang Wen and Zhenghan Wang. Topological properties of Abelian and non-Abelian quantum Hall states classified using patterns of zeros. *Phys. Rev. B*, 78(15):155109, 2008.

[92] E. J. Bergholtz and A. Karlhede. Quantum Hall system in Tao-Thouless limit. *Phys. Rev. B*, 77(15):155308, 2008.

[93] B. Andrei Bernevig and N. Regnault. Emergent many-body translational symmetries of Abelian and non-Abelian fractionally filled topological insulators. *Phys. Rev. B*, 85(7):075128, 2012.

[94] Hui Li and F. D. M. Haldane. Entanglement Spectrum as a Generalization of Entanglement Entropy: Identification of Topological Order in Non-Abelian Fractional Quantum Hall Effect States. *Phys. Rev. Lett.*, 101(1):010504, 2008.

[95] N. Regnault. Entanglement Spectroscopy and its Application to the Quantum Hall Effects. *arXiv:1510.07670*, 2015.

[96] A. Sterdyniak, N. Regnault, and B. A. Bernevig. Extracting Excitations from Model State Entanglement. *Phys. Rev. Lett.*, 106(10):100405, 2011.

[97] Xiao-Liang Qi. Generic Wave-Function Description of Fractional Quantum Anomalous Hall States and Fractional Topological Insulators. *Phys. Rev. Lett.*, 107(12):126803, 2011.

[98] Zhao Liu, Emil J. Bergholtz, Heng Fan, and Andreas M. Läuchli. Fractional Chern Insulators in Topological Flat Bands with Higher Chern Number. *Phys. Rev. Lett.*, 109(18):186805, 2012.

[99] Gunnar Möller and Nigel R. Cooper. Fractional Chern Insulators in Harper-Hofstadter Bands with Higher Chern Number. *Phys. Rev. Lett.*, 115(12):126401, 2015.

[100] Yang-Le Wu, N. Regnault, and B. Andrei Bernevig. Bloch Model Wave Functions and Pseudopotentials for All Fractional Chern Insulators. *Phys. Rev. Lett.*, 110(10):106802, 2013.

[101] S. M. Girvin, A. H. MacDonald, and P. M. Platzman. Magneto-roton theory of collective excitations in the fractional quantum Hall effect. *Phys. Rev. B*, 33(4):2481–2494, 1986.

[102] Rahul Roy. Band geometry of fractional topological insulators. *Phys. Rev. B*, 90(16):165139, 2014.

[103] Tomoki Ozawa and Bruno Mera. Relations between topology and the quantum metric for Chern insulators. *Phys. Rev. B*, 104(4):045103, 2021.

[104] Jie Wang, Jennifer Cano, Andrew J. Millis, Zhao Liu, and Bo Yang. Exact Landau Level Description of Geometry and Interaction in a Flatband. *Phys. Rev. Lett.*, 127(24):246403, 2021.

[105] Patrick J. Ledwith, Ashvin Vishwanath, and Daniel E. Parker. Vortexability: A Unifying Criterion for Ideal Fractional Chern Insulators. *arXiv:2209.15023*, 2022.

[106] P. R. Wallace. The Band Theory of Graphite. *Phys. Rev.*, 71(9):622–634, 1947.

[107] E. Mostaani, N.D. Drummond, and Falko. V. I. Quantum Monte Carlo Calculation of the Binding Energy of Bilayer Graphene. *Phys. Rev. Lett.*, 115(11).

[108] Edward McCann and Mikito Koshino. The electronic properties of bilayer graphene. *Rep. Prog. Phys.*, 76(5):056503, 2013.

[109] Mikito Koshino and Edward McCann. Trigonal warping and Berry's phase $N\pi$ in ABC-stacked multilayer graphene. *Phys. Rev. B*, 80(16):165409, 2009.

[110] J. M. B. Lopes dos Santos, N. M. R. Peres, and A. H. Castro Neto. Continuum model of the twisted graphene bilayer. *Phys. Rev. B*, 86(15):155449, 2012.

[111] Nguyen N. T. Nam and Mikito Koshino. Lattice relaxation and energy band modulation in twisted bilayer graphene. *Phys. Rev. B*, 96(7):075311, 2017.

[112] Kasra Hejazi, Chunxiao Liu, Hassan Shapourian, Xiao Chen, and Leon Balents. Multiple topological transitions in twisted bilayer graphene near the first magic angle. *Phys. Rev. B*, 99(3):035111, 2019.

[113] Jeil Jung, Arnaud Raoux, Zhenhua Qiao, and A. H. MacDonald. Ab initio theory of moiré superlattice bands in layered two-dimensional materials. *Phys. Rev. B*, 89(20):205414, 2014.

[114] Hoi Chun Po, Liujun Zou, Ashvin Vishwanath, and T. Senthil. Origin of Mott Insulating Behavior and Superconductivity in Twisted Bilayer Graphene. *Phys. Rev. X*, 8(3):031089, 2018.

[115] J. A. Wilson, F. J. Di Salvo, and S. Mahajan. Charge-Density Waves in Metallic, Layered, Transition-Metal Dichalcogenides. *Phys. Rev. Lett.*, 32(16):882–885, April 1974.

[116] B. Radisavljevic, A. Radenovic, J. Brivio, V. Giacometti, and A. Kis. Single-layer MoS2 transistors. *Nature Nanotech*, 6(3):147–150, 2011.

[117] Kin Fai Mak, Changgu Lee, James Hone, Jie Shan, and Tony F. Heinz. Atomically Thin MoS_2: A New Direct-Gap Semiconductor. *Phys. Rev. Lett.*, 105(13):136805, 2010.

[118] Z. Y. Zhu, Y. C. Cheng, and U. Schwingenschlögl. Giant spin-orbit-induced spin splitting in two-dimensional transition-metal dichalcogenide semiconductors. *Phys. Rev. B*, 84(15):153402, 2011.

[119] G. Dresselhaus. Spin-Orbit Coupling Effects in Zinc Blende Structures. *Phys. Rev.*, 100(2):580–586, 1955.

[120] Fengcheng Wu, Timothy Lovorn, Emanuel Tutuc, and A. H. MacDonald. Hubbard Model Physics in Transition Metal Dichalcogenide Moir\'e Bands. *Phys. Rev. Lett.*, 121(2):026402, 2018.

[121] Fengcheng Wu, Timothy Lovorn, Emanuel Tutuc, Ivar Martin, and A. H. MacDonald. Topological Insulators in Twisted Transition Metal Dichalcogenide Homobilayers. *Phys. Rev. Lett.*, 122(8):086402, 2019.

[122] Hoi Chun Po, Haruki Watanabe, and Ashvin Vishwanath. Fragile Topology and Wannier Obstructions. *Phys. Rev. Lett.*, 121(12):126402, 2018.

[123] Hoi Chun Po, Liujun Zou, T. Senthil, and Ashvin Vishwanath. Faithful tight-binding models and fragile topology of magic-angle bilayer graphene. *Phys. Rev. B*, 99(19):195455, 2019.

[124] Zhida Song, Zhijun Wang, Wujun Shi, Gang Li, Chen Fang, and B. Andrei Bernevig. All Magic Angles in Twisted Bilayer Graphene are Topological. *Phys. Rev. Lett.*, 123(3):036401, 2019.

[125] C. L. Kane and E. J. Mele. Quantum Spin Hall Effect in Graphene. *Phys. Rev. Lett.*, 95(22):226801, 2005.

[126] Edward H. Rezayi and Steven H. Simon. Breaking of Particle-Hole Symmetry by Landau Level Mixing in the $\nu = 5/2$ Quantized Hall State. *Phys. Rev. Lett.*, 106(11), 2011.

[127] A. M. Läuchli, Zhao Liu, E. J. Bergholtz, and R. Moessner. Hierarchy of Fractional Chern Insulators and Competing Compressible States. *Phys. Rev. Lett.*, 111(12):126802, 2013.

[128] Cécile Repellin and T. Senthil. Chern bands of twisted bilayer graphene: Fractional Chern insulators and spin phase transition. *Phys. Rev. Res.*, 2(2), 2020.

[129] Patrick J. Ledwith, Grigory Tarnopolsky, Eslam Khalaf, and Ashvin Vishwanath. Fractional Chern insulator states in twisted bilayer graphene: An analytical approach. *Phys. Rev. Res.*, 2(2), 2020.

[130] Grigory Tarnopolsky, Alex Jura Kruchkov, and Ashvin Vishwanath. Origin of Magic Angles in Twisted Bilayer Graphene. *Phys. Rev. Lett*, 122(10), 2019.

[131] F. D. M. Haldane and E. H. Rezayi. Periodic Laughlin-Jastrow wave functions for the fractional quantized Hall effect. *Phys. Rev. B*, 31(4), 1985.

[132] Patrick Wilhelm, Thomas C. Lang, and Andreas M. Läuchli. Interplay of fractional Chern insulator and charge density wave phases in twisted bilayer graphene. *Phys. Rev. B*, 103(12), 2021.

[133] Junkai Dong, Patrick J. Ledwith, Eslam Khalaf, Jong Yeon Lee, and Ashvin Vishwanath. Exact Many-Body Ground States from Decomposition of Ideal Higher Chern Bands: Applications to Chirally Twisted Graphene Multilayers. *arXiv.2210.13477*, 2022.

[134] Zhao Liu, Abolhassan Vaezi, Kyungmin Lee, and Eun-Ah Kim. Non-Abelian phases in two-component $\nu = 2/3$ fractional quantum Hall states: Emergence of Fibonacci anyons. *Phys. Rev. B*, 92(8), 2015.

[135] Eliot Kapit and Erich Mueller. Exact Parent Hamiltonian for the Quantum Hall States in a Lattice. *Phys. Rev. Lett.*, 105(21), 2010.

[136] Douglas R. Hofstadter. Energy levels and wave functions of Bloch electrons in rational and irrational magnetic fields. *Phys. Rev. B*, 14(6), 1976.

[137] Nicola A. Hill. Why Are There so Few Magnetic Ferroelectrics? *J. Phys. Chem. B*, 104(29), 2000.

[138] Daijiro Yoshioka. *The Quantum Hall Effect*, volume 133 of *Springer Series in Solid-State Sciences*. Springer Berlin Heidelberg, Berlin, Heidelberg, 2002.

[139] Xiao-Gang Wen. Continuous Topological Phase Transitions between Clean Quantum Hall States. *Phys. Rev. Lett.*, 84(17), 2000.

[140] W. Zhu, Zhao Liu, F. D. M. Haldane, and D. N. Sheng. Fractional Quantum Hall Bilayers at Half-Filling: Tunneling-driven Non-Abelian Phase. *Phys. Rev. B*, 94(24), 2016.

[141] Maissam Barkeshli and Xiao-Liang Qi. Topological Nematic States and Non-Abelian Lattice Dislocations. *Phys. Rev. X*, 2(3), 2012.

[142] Zhao Liu, Gunnar Möller, and Emil J. Bergholtz. Exotic Non-Abelian Topological Defects in Lattice Fractional Quantum Hall States. *Phys. Rev. Lett.*, 119(10), 2017.

[143] P. Törmä, S. Peotta, and B. A. Bernevig. Superfluidity and Quantum Geometry in Twisted Multilayer Systems. *arXiv:2111.00807*, 2021.

Accompanying Papers